

博士論文

**Chirality selective growth of single-walled carbon
nanotubes using W-Co alloy catalyst**

(W-Co 合金触媒を用いたカイラリティ制御
単層カーボンナノチューブ合成)

Hua AN
(安華)

Doctoral dissertation

**Chirality selective growth of single-walled carbon
nanotubes using W-Co alloy catalyst**

by

Hua AN

Presented to

GRADUATE SCHOOL OF ENGINEERING, THE UNIVERSITY OF TOKYO

in Partial Fulfillment of the Requirements for the Degree of

Doctoral of Philosophy

in the Field of Mechanical Engineering

2017.3

Abstract

Ever since their discovery, single-walled carbon nanotubes (SWNTs) have attracted intensive attention because of their unique properties and potential applications. The diversity of SWNT atomic structures provides a broad window for their applications in nanodevices. However, the candidates for individual devices require SWNT assemblies with homogeneous structure and properties. Unfortunately, the as-grown SWNTs are always a mixture of various chiralities, which hinders their applications in nanoelectronics. Since the chirality determines the property of SWNTs, diameter-control and chirality-control are the prerequisite to obtain SWNTs with homogeneous properties. Extensive researches have focused on the direct growth of SWNTs with identical chirality and diameter, however, it is still a critical challenge to grow single-chirality SWNT assemblies. Catalysts play an important role in the chirality definition of SWNTs during the growth. Bimetallic catalysts usually possess different catalytic properties than either of their parental metals and thus they have been widely explored in catalytic reactions for SWNTs growth. In this dissertation, the bimetallic catalysts will be the main focus to selectively control the diameter and chirality of SWNTs.

In order to investigate the mechanism of the growth of SWNTs with transmission electron microscopy (TEM), we have developed an in-plane TEM method where a thin amorphous SiO₂ window can work as the substrate to directly grow SWNTs with deposited catalysts. By using the in-plane TEM method, we have successfully studied the CuCo bimetallic catalyst which can grow small-diameter SWNTs at relatively low temperature. An anchoring effect of Cu has been proposed to prevent the active Co catalyst particles from aggregating to larger ones resulting in the production of small-diameter SWNTs.

Recently, Co₇W₆ clusters were reported to successfully grow a metallic chirality (12, 6) SWNT, with over 90% abundance, a zigzag (16, 0) SWNT with near 80% and a semiconducting (14, 4) SWNT with over 97%, by controlling the catalyst structure and

growth conditions with a high-temperature reduction and growth [*Nature*, 2014, **510**, 522; *J. Am. Chem. Soc.*, 2015, **137**, 8688; *ACS Nano*, 2017, **11**: 186]. However, the low yield and short SWNTs inhibit the large-scale applications of the near single-chirality SWNT assemblies. Here, we report a simple sputtered W-Co catalyst can selectively grow high-quality (12, 6) SWNTs with better uniformity by low pressure chemical vapor deposition at lower temperature than the Nature paper. The abundance of (12, 6) is 50%-70% according to the statistical Raman mapping analysis and optical absorption spectrum of the randomly collected as-grown SWNTs. Parametric study of the W-Co catalyst system demonstrates that the reduction temperature before growth is critical for the selectivity and the intermediate structure, $\text{Co}_6\text{W}_6\text{C}$, is identified by the electron diffraction. Moreover, the catalyst particles are transformed to Co after 5 min-growth. The investigation of catalysts discloses the complicated structure changes before and after CVD growth.

The as-reduced catalyst particles are characterized by EDS mapping to further understand the elemental distribution of nano sized particles and an acid treatment experiment is designed to verify the nonexistence of the trifle amount of pure Co phase. The time-dependent study confirms that the dynamic evolution of catalyst structure is associated with the selectivity towards (12, 6). The $\text{Co}_6\text{W}_6\text{C}$ is more likely to correlate with the nucleation of (12, 6) cap to achieve a selective growth. A proposed mechanism reveals the elongated nucleation and growth stage which is strongly dependent on the catalyst structure. The structure evolution of catalyst particles indicates a possible clue for the understanding of selective growth with $\text{Co}_6\text{W}_6\text{C}$. The in-plane TEM study with W-Co bimetallic catalyst paves an important way to the final goal of single-chirality synthesis of SWNTs.

Contents

Abstract.....	i
Chapter 1 Background and introduction to single-walled carbon nanotubes	1
1.1 Introduction to single-walled carbon nanotubes	1
1.2 Structure and properties of SWNTs	3
1.2.1 Chirality of SWNTs	3
1.2.2 Electronic structure of SWNTs	6
1.2.3 Phonon structure of SWNTs	10
1.3 Synthesis method	10
1.3.1 Arc discharge	10
1.3.2 Laser ablation	11
1.3.3 Chemical vapor deposition (CVD)	12
1.4 Growth mechanism	13
1.5 Assembly morphology and potential applications	15
1.6 Main challenges for the industrial applications	16
1.7 Motivation, objective and organization of this dissertation	17
Chapter 2 Experimental methods.....	19
2.1 Preparation methods for catalysts	19
2.1.1 Dip-coating	19
2.1.2 Magnetron sputtering.....	20
2.2 Synthesis of SWNTs	21
2.3 Characterization of SWNTs	22
2.3.1 Raman spectroscopy	22
2.3.2 Optical absorption spectroscopy	26
2.3.3 Scanning electron microscopy (SEM)	29
2.3.4 Transmission electron microscopy (TEM).....	31

2.3.5 Electron diffraction	31
2.3.6 In-plane transmission electron microscopy (TEM)	33
2.3.7 Application of in-plane TEM in the study of synthesis of small-diameter SWNTs with CuCo.....	34
2.4 Summary	43
 Chapter 3 Selective synthesis of (12, 6) with sputtered W-Co	44
3.1 State of art to achieve single chirality of SWNTs.....	44
3.1.1 Separation of SWNTs	45
3.1.2 Selective synthesis of SWNTs	45
3.1.3 Catalysts in the selective growth of SWNTs.....	46
3.1.4 Recent breakthroughs of high selectivity with W-based catalyst.....	47
3.2 Selective growth of (12, 6) with sputtered W-Co	48
3.2.1 Growth of SWNTs with sputtered W-Co as catalyst.....	48
3.2.2 Characterization of (12, 6).....	49
3.3 Parametric study of the selective growth of SWNTs with sputtered W-Co.....	56
3.3.1 Influence of the ratio of W to Co	57
3.3.2 Effect of reduction temperature	59
3.4 Investigation of W-Co catalyst and SWNTs with in-plane TEM.....	62
3.4.1 TEM imaging of catalyst morphology	62
3.4.2 Electron diffraction pattern of the W-Co catalyst particles.....	64
3.5 Summary	67
 Chapter 4 Structure evolution of W-Co catalyst and the possible mechanism	68
4.1 Detailed characterization of as-reduced catalysts	68
4.1.1 Further confirmation of the as-reduced catalysts by acid treatment	69
4.1.2 Elemental distribution of W-Co catalysts	70
4.2 Time-dependent growth of SWNTs with sputtered W-Co	74
4.2.1 Time-dependent growth of SWNTs	74
4.2.2 In-plane TEM observation of W-Co catalysts at different growth time	75
4.2.3 Discussions on the W-Co catalyst evolution with phase diagram.....	79

4.2.4 Intermediate structure of W-Co catalyst particles.....	80
4.2.5 Possible mechanism of the structure evolution of W-Co catalyst during the growth of SWNTs with ethanol.....	83
4.3 Summary	84
Chapter 5 Conclusions.....	85
5.1 Summary of the dissertation	85
5.2 Prospects	86
Bibliography	87
List of abbreviations	106
List of publications.....	108
Acknowledgement	109

Chapter 1 Background and introduction to single-walled carbon nanotubes

This chapter will give a brief background of single-walled carbon nanotubes which will start with an introduction of carbon, its allotropes and the nanocarbon family. The basic structure and physical properties of single-walled carbon nanotubes will be the main part followed by the widely used synthetic methods and proposed mechanism for SWNTs. Different morphologies of SWNT assemblies reported for various purposes of applications are discussed afterwards. The current main challenges which hinder the industrial applications will be introduced in detail. Finally, the motivations and objectives of this dissertation and organization for the following four chapters will be the closing part.

1.1 Introduction to single-walled carbon nanotubes

Carbon is regarded as one of the most important elements on earth, consisting of the basic skeleton of organic for living things from as huge as whale to as tiny as virus. Carbon is located at group 14, the middle of the main group, unlike the alkali metals or halogens which can lose or get one electron easily to form a perfect stable state as the noble gases. Out of the nucleus, carbon has six electrons of which four belong to the valence electrons. The atomic structure of carbon is shown in Figure 1.1.

The unique atomic structure gives carbon peculiar chemical properties. Six electrons in carbon occupy three different orbitals that is 1s, 2s, 2p. The four electrons in the outer orbitals do not behave equally in the chemical reactions thus carbon can take two different chemical

valences +2 and +4 in compounds, for example CO and CO₂. Four outer electrons can combine with four other electrons to form four covalent bonds in the most stable state which also strengthens the compound. This is the typical micro-structure of diamond through sp^3 hybridization, constituting one of the hardest materials on the earth. Another important allotrope is graphite. Graphite is a layered carbon material and the micro-structure unit of one layer of graphite is a hexagon with six carbon atoms. The schematic of the one-layer graphite is shown in Figure 1.2. The six carbon atoms are bonded via sp^2 hybridization to form a planar structure with π - π bond perpendicular to the hexagonal plane. These hexagons can combine with pentagons and heptagons to form a football shape molecule-fullerene. This hexagon unit can also extend in planar directions to form one-layer graphite-graphene. By rolling up this graphene layer to form a cylinder with two fullerene hemispheric caps at both ends, that is single-walled carbon nanotubes. Multi-walled carbon nanotubes can be formed by rolling up multi layers of graphene sheets. The corresponding microstructures of these nanocarbons are shown in Figure 1.3.

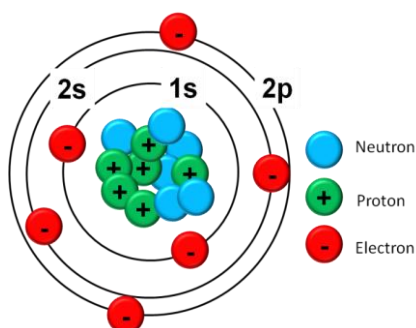


Figure 1.1 Carbon atomic structure.

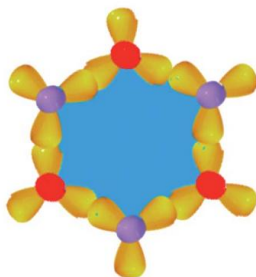


Figure 1.2 Schematic of the hexagonal structure of the graphene unit. Reproduced from [1] with permission of The Royal Society of Chemistry.

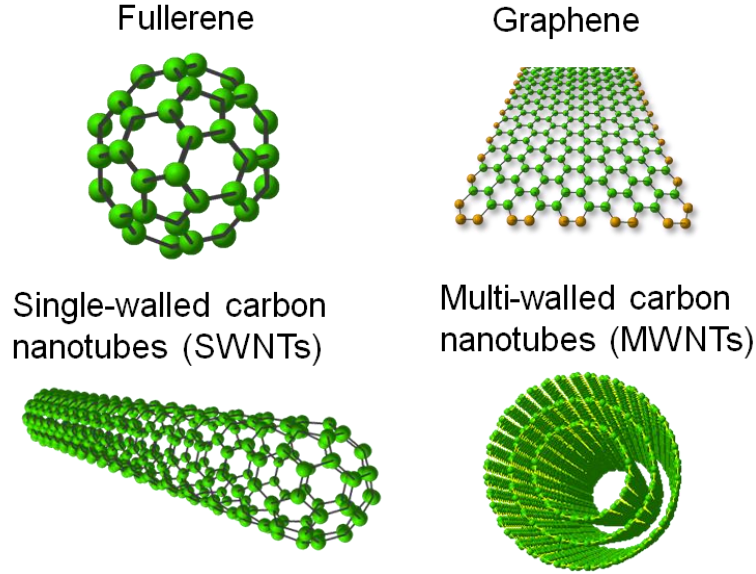


Figure 1.3 Various structures in nanocarbon family. Images are from <http://www.photon.t.u-tokyo.ac.jp>.

1.2 Structure and properties of SWNTs

Single-walled carbon nanotubes (SWNTs) are regarded as rolling up a graphene sheet to a cylinder with a diameter of subnanometers to a few nanometers and a length of more than micrometer scale to form one dimensional material with a high aspect ratio and possess excellent structure-dependent mechanical, optical, physical and thermal properties. The structure of SWNTs is determined by the way of rolling-up which in turn defines their properties [2, 3].

1.2.1 Chirality of SWNTs

The definition of chirality of SWNTs comes from the symmetry of the structure when rolling up the graphene sheet. Figure 1.4 shows the unrolled graphene hexagonal lattice structure. \mathbf{a}_1 and \mathbf{a}_2 are the unit vectors which can be expressed with the bond length of a graphene hexagon $a_{c-c}=1.42 \text{ \AA}$ as

$$\mathbf{a}_1 = \left(\frac{3}{2} a_{c-c}, \frac{\sqrt{3}}{2} a_{c-c} \right), \mathbf{a}_2 = \left(\frac{3}{2} a_{c-c}, -\frac{\sqrt{3}}{2} a_{c-c} \right),$$

According to the relationship in regular hexagon, there is $a = |\mathbf{a}_1| = |\mathbf{a}_2| = \sqrt{3} a_{c-c} = 2.46 \text{ \AA}$ which is the lattice constant of graphene, thus the vectors can also be

$$\mathbf{a}_1 = \left(\frac{\sqrt{3}}{2}, \frac{1}{2} \right) a, \mathbf{a}_2 = \left(\frac{\sqrt{3}}{2}, -\frac{1}{2} \right) a,$$

The rolling way of graphene sheet to be a SWNT can be determined uniquely by the chiral vector \mathbf{C}_h which can be expressed by the unit vectors \mathbf{a}_1 and \mathbf{a}_2 as

$$\mathbf{C}_h = n\mathbf{a}_1 + m\mathbf{a}_2 \equiv (n, m)$$

And \mathbf{C}_h is the radial direction of the rolled-up single-walled carbon nanotube. In this coordinate, the integer pairs of (n, m) can be used to uniquely define a single-walled carbon nanotube, thus (n, m) is one important index to denote the chirality of SWNTs and normally for convenience, we specify $n \geq m$.

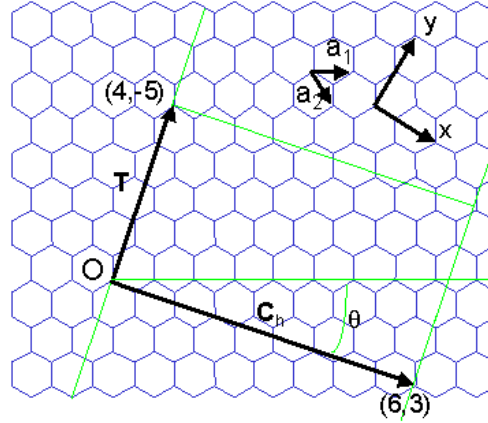


Figure 1.4 Unrolled graphene lattice showing the definition of the chirality of SWNTs. Image is from <http://www.photon.t.u-tokyo.ac.jp>.

The circumference of the SWNT is $|\mathbf{C}_h| = \sqrt{3} a_{c-c} \sqrt{n^2 + nm + m^2}$, so the diameter of the SWNT is

$$d_t = \frac{|\mathbf{C}_h|}{\pi} = \frac{\sqrt{3}a_{c-c} \sqrt{(n^2 + nm + m^2)}}{\pi} \propto \sqrt{n^2 + nm + m^2}$$

For the definition of a SWNT, another important vector is the translation vector \mathbf{T} in Figure 1.4, which is the shortest repeat distance along the axial direction. \mathbf{T} can be expressed as

$$\mathbf{T} = t_1 \mathbf{a}_1 + t_2 \mathbf{a}_2 \equiv (t_1, t_2)$$

The relationship of (t_1, t_2) to (n, m) is

$$t_1 = \frac{2m+n}{d_R}, t_2 = -\frac{2n+m}{d_R}$$

where d_R is the greatest common divisor of $(2m+n, 2n+m)$ and can be

$$d_R = \begin{cases} d, & \text{if } n-m \text{ is not a multiple of } 3d, \\ 3d, & \text{if } n-m \text{ is a multiple of } 3d. \end{cases}$$

where d is the greatest common divisor of (n, m) .

The area of chiral vector \mathbf{C}_h and transition vector \mathbf{T} defines the unit cell of the SWNT, and the number of hexagons, N , in this area is

$$N = \frac{|\mathbf{C}_h \times \mathbf{T}|}{|\mathbf{a}_1 \times \mathbf{a}_2|} = \frac{2(n^2 + m^2 + nm)}{d_R}$$

As shown in Figure 1.4, the angle between chiral vector \mathbf{C}_h and unit vector \mathbf{a}_1 is defined as the chiral angle θ , which is given by n and m as

$$\theta = \tan^{-1} \left(\frac{\sqrt{3}m}{m+2n} \right)$$

The chiral angle ranges from 0° to 30° ($0^\circ \leq \theta \leq 30^\circ$). When θ is 0° , it is a zigzag SWNT, and if θ is 30° , it is a armchair SWNT, and others are chiral SWNTs. The pair of (d_t, θ) is another

important index to denote the chirality of SWNTs as shown in Figure 1.5.

SWNTs can be divided into metallic and semiconducting SWNTs according to their electronic properties, as shown in the chiral map in Figure 1.5. The SWNTs can also be either left handed or right handed, but generally, the handedness of SWNTs does not significantly affect their physical properties and can be experimentally detected only when external fields are applied. Thus we do not discuss the handedness when we talk about the chirality of SWNTs.

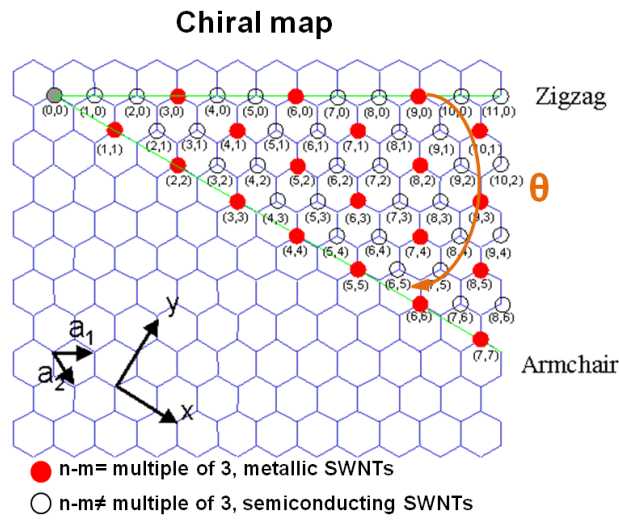


Figure 1.5 Chiral map of SWNTs where one pair of (n, m) indice represents one chirality of SWNTs and the black open circles are the semiconducting SWNTs and the red solid circles represent the metallic SWNTs. Image modified from <http://www.photon.t.u-tokyo.ac.jp>.

1.2.2 Electronic structure of SWNTs

The electronic structure of SWNTs can be understood by imposing a zone-folding effect on the 2D graphite material with tight-binding calculation method since the SWNTs can be formed by rolling up the one layer 2D graphite [2].

Figure 1.6 shows the unit cell of 2D graphene in real space and reciprocal space with the Brillouin zone of 2D graphite in gray hexagon. The unit vector in reciprocal space can be given by

$$\mathbf{b}_1 = \left(\frac{2\pi}{\sqrt{3}a}, \frac{2\pi}{a} \right), \mathbf{b}_2 = \left(\frac{2\pi}{\sqrt{3}a}, -\frac{2\pi}{a} \right)$$

where a is the lattice constant of graphene in real space and the lattice constant in reciprocal space is $4\pi/\sqrt{3}a$. The high symmetry points are denoted as Γ , M , K shown in Figure 1.6 at the center, center of edge and the corner respectively. The reciprocal lattice vector \mathbf{K}_1 in the circumferential direction and \mathbf{K}_2 along the axial direction are corresponding with the chiral vector \mathbf{C}_h and the transitional vector \mathbf{T} in the real space and define the discrete k values for the Brillouin zone of a SWNT. The \mathbf{K}_1 and \mathbf{K}_2 correlate to \mathbf{C}_h and \mathbf{T} as

$$\mathbf{C}_h \cdot \mathbf{K}_1 = 2\pi, \mathbf{T} \cdot \mathbf{K}_1 = 0, \mathbf{C}_h \cdot \mathbf{K}_2 = 0, \mathbf{T} \cdot \mathbf{K}_2 = 0.$$

Thus

$$N\mathbf{K}_1 = (-t_2\mathbf{b}_1 + t_1\mathbf{b}_2), N\mathbf{K}_2 = (m\mathbf{b}_1 - n\mathbf{b}_2).$$

The first Brillouin zone of a SWNT is a series of cutting lines in the circumferential direction shown in Figure 1.6c. The N wave vectors $\mu\mathbf{K}_1$ ($\mu = 0, \dots, N-1$) bring about N discrete k vectors or parallel cutting lines and each of the μ discrete values corresponds to one electronic energy band and 6 branches in the phonon dispersion relations. The length of the parallel lines is $2\pi/\mathbf{T}$. The spacing between the cutting lines is $2\pi/L_t$ with a SWNT length of L_t which will be continuous wave vectors if the SWNT length extends to infinity due to the translational symmetry of \mathbf{T} .

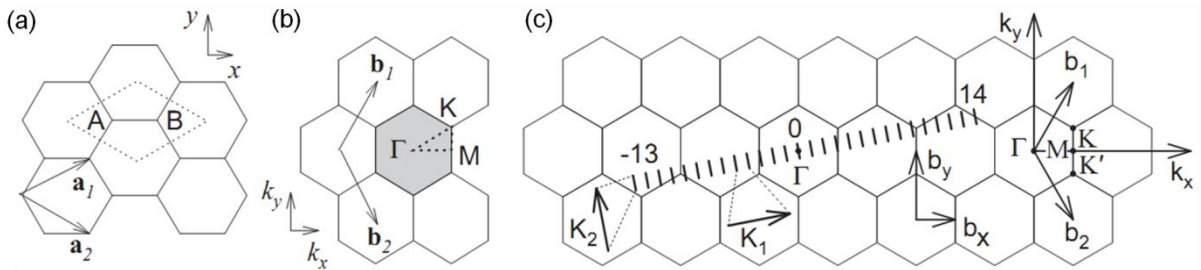


Figure 1.6 (a) Unit cell of the 2D graphene in real space. (b) Brillouin zone (shaded hexagon area) for 2D graphene in reciprocal space. (c) Brillouin zone for (4, 2) SWNT in reciprocal space. Reprinted from [2], Copyright (2005), with permission from Elsevier.

Figure 1.7a shows the electronic dispersion of the first Brillouin zone from the π and π^* bands close to the Fermi level of 2D graphite with the tight-binding calculation. K points are the corners where the valence and conduction bands touch together and around there optical transitions can occur. By superimposing the cutting lines from SWNT reciprocal space on this electronic dispersion surface, we can get the electronic band structure of a SWNT given by

$$E_{\mu}(k) = E_{g2D}(k \frac{\mathbf{K}_2}{|\mathbf{K}_2|} + \mu \mathbf{K}_1), \quad (\mu=0, \dots, N-1, \text{ and } -\frac{\pi}{T} < k < \frac{\pi}{T})$$

As shown in Figure 1.7b, if the cutting lines pass across the K points of the Brillouin zone, the certain (n, m) SWNT is metallic with a zero band gap, otherwise, the SWNT is semiconducting with a nonzero band gap between valence and conduction bands. According to the calculation, the condition for metallic SWNTs is that the (n-m) is a multiple of 3. As shown in Figure 1.5, one third of indices are metallic and the other two thirds are semiconducting, which means the as-grown sample will have 67% of semiconducting SWNTs and 33% of metallic SWNTs if all the SWNTs in the chiral table are equivalently grown. In fact, due to the curvature effect, only armchair SWNTs are truly metallic, while other metallic (n-m=3d, d≠0) SWNTs are only gapless at room temperature but will have a small chirality-dependent band gap with decreasing temperatures.

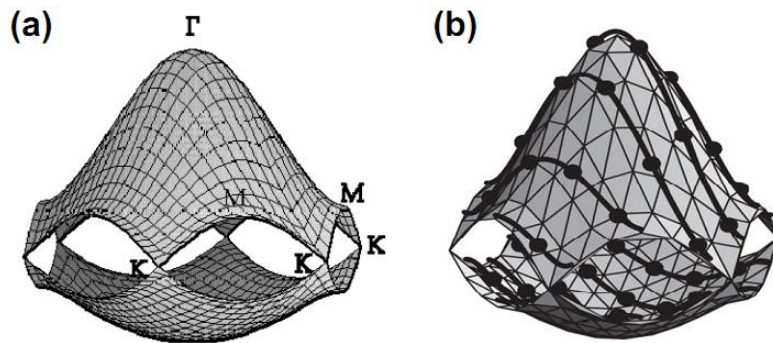


Figure 1.7 Three dimensional band structure of (a) 2D graphene layer (Image from: <http://www.photon.t.u-tokyo.ac.jp> and <http://flex.phys.tohoku.ac.jp>) and (b) a SWNT calculated from the nearest neighbor tight bonding model. Reprinted from [2], Copyright (2005), with permission from Elsevier.

Of particular importance pertaining to semiconducting SWNTs is that the band gap is independent of chiral angle but relies on the reciprocal nanotube diameter d_t with an equation

$$E_g = \frac{|t| a_{c-c}}{d_t}$$

With this relation, we can conclude that the band gap of semiconducting SWNTs is inversely proportional to their diameter.

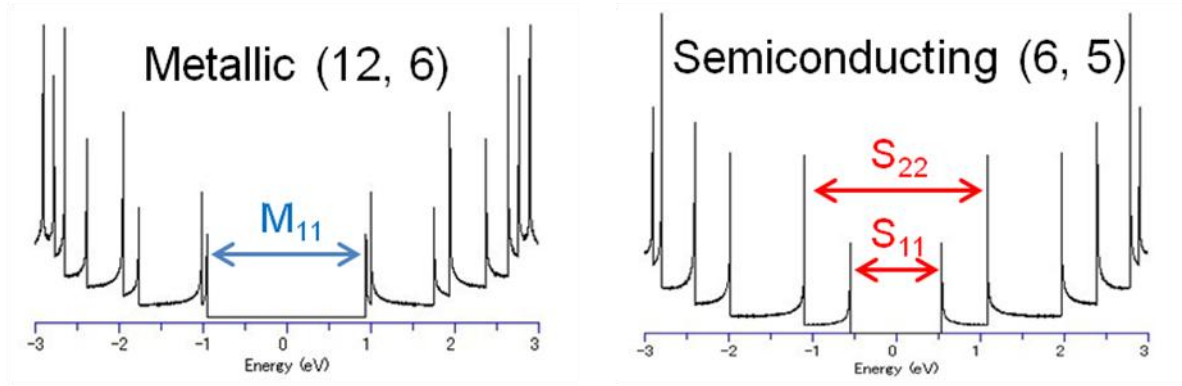


Figure 1.8 One dimensional density of states for metallic (12, 6) and semiconducting (6, 5). Images modified from <http://www.photon.t.u-tokyo.ac.jp>.

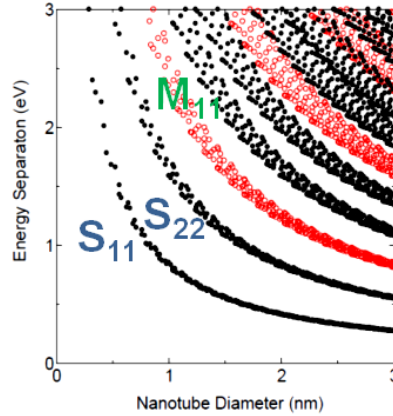


Figure 1.9 Kataura plot with the relation of transition energies vs the diameter of SWNTs. Image modified from <http://www.photon.t.u-tokyo.ac.jp>.

Figure 1.8 shows the density of states of typical metallic and semiconducting SWNTs. A certain chirality of SWNT possesses a specific set of van Hove singularities (vHS) and can exhibit corresponding sets of optical transitions leading to the structural determination of (n,

m) by optical experiments. The energy transitions within vHS are labeled as E_{ii} values and specific to a definite (n, m) SWNT. The relationship of E_{ii} for (n, m) to its diameter is shown in Figure 1.9 with tight binding calculation which is called Kataura plot. The electronic energy transitions M_{ii} for metallic SWNTs and S_{ii} for semiconducting SWNTs play an important role in the interpretation of optical spectra for the assignment of (n, m).

Thus the property of SWNTs can be defined by their structure which provides a diversity of applications in electronic devices making SWNTs one of the most promising building blocks in nanoelectronics.

1.2.3 Phonon structure of SWNTs

Similar to the electronic structure, the phonon structure of SWNTs can also be interpreted by the phonon dispersion relations of 2D graphene sheet with a 1D quantum confinement [2]. Thus the phonon density of states for a certain SWNT can be obtained by a zone folding effect which is applicable to most of the phonon modes but needs to be corrected with additional physical concepts for the low frequency region. On the other hand, the Raman signals originate from the corresponding phonon modes with different symmetry which helps us to interpret the Raman spectrum. Phonon structure determines the thermal and mechanical properties of a solid material and also affects the electron transport phenomena. Since the phonon dispersion relations of a SWNT depend on the chirality and diameter of the SWNT, the properties of a SWNT strongly depend on its chirality and diameter.

1.3 Synthesis method

1.3.1 Arc discharge

In the two separate discovery works of single-walled carbon nanotubes, arc discharge is the method to synthesize CNTs with one-atomic-layer wall which is originally used in the production of fullerenes [4, 5]. Typically, in this simple and conventional method, one graphitic composite rod composed of graphite and one single metal or mixed metals is

attached to the anode electrode which is coaxial with another carbon rod at a distance of around 1 mm in the chamber [6]. The metal in the composite rod acts as catalyst in the synthetic reaction. Voltage is applied to the electrodes with an electric current across. While operating, the chamber is flowed with inert gas or hydrogen or mixed gas at low pressure. The synthesized SWNTs will deposit on the cathode side. Catalyst is necessary for the growth of SWNTs but in the case of MWNTs, no catalysts are used. The catalyst composites usually include transitional metals Fe, Co, Ni, Pd, Pt etc and their corresponding mixtures with other metals. Accompanied with SWNTs are some other unwanted byproducts such as MWNTs, soot and fullerenes. It will require a post growth purification process before application [7].

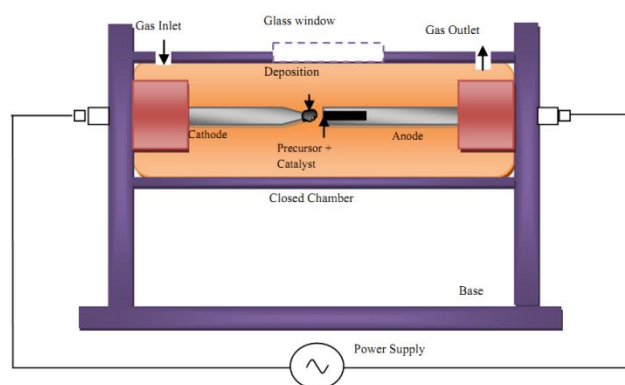


Figure 1.10 Schematic of arc discharge method. Reprinted from [6], Copyright (2014), with permission from Elsevier.

1.3.2 Laser ablation

Another high temperature growth method is the laser ablation which was first used for the production of SWNTs by Smalley's group in 1995 [8]. A high temperature furnace is mounted with a computer controlled laser in the upstream side and a water cooling system at the downstream side. A composite target made of graphite and metal catalyst is placed in the center part of a quartz tube. The chamber is evacuated and then filled with argon gas. SWNTs are produced by laser assisted vaporization and flowed with Ar gas to the collector at the downstream. Diameter of SWNTs can be tuned by varying growth conditions or catalyst compositions to some extent. With this approach, it is still very challenging to scale up the production and purify SWNTs for practical applications because of their highly tangled rope

morphology [9].

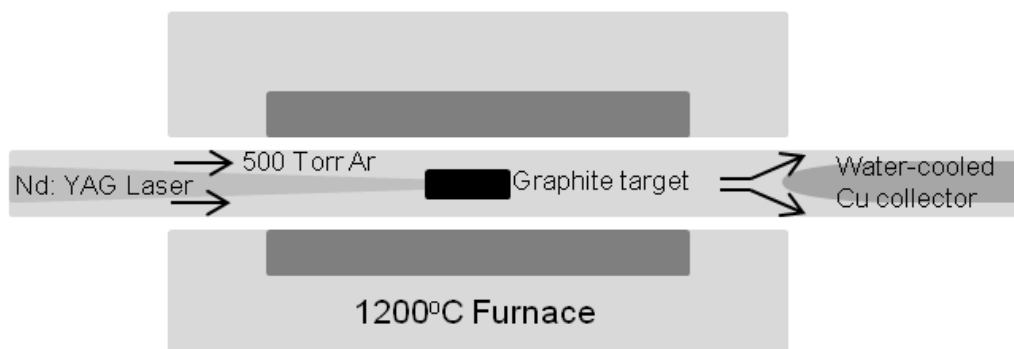


Figure 1.11 Schematic of the oven laser-vaporization apparatus. Modified from [8], Copyright (1995), with permission from Elsevier.

1.3.3 Chemical vapor deposition (CVD)

Chemical vapor deposition (CVD) is previously used to produce carbon fibers but also show great advantages in the growth of SWNTs [3, 10-13]. The decomposition of a hydrocarbon and the deposition of SWNTs can be realized at a much lower temperature than the other two methods. CVD method is versatile and viable for scale-up production of SWNTs for industrial applications and it is easy to control the parameters showing more potential to control the structure and distribution of the as-grown SWNTs. Most importantly, the SWNTs grown from CVD method are of high quality and high purity with low cost. A classic CVD reactor is shown in Figure 1.12. The catalysts are deposited on a flat substrate or support materials in a quartz boat placing under the thermal couple region in the tube chamber. Hydrocarbon gas as the carbon source is flowed and decomposed at the growth temperature. Then SWNTs can be grown on the substrate or support materials with catalysts.

Other setups for CVD system are also available for specific purpose including plasma enhanced CVD and hot filament CVD etc. Other methods which are not widely used in the synthesis of SWNTs will not be introduced in this dissertation. Since the CVD method is more promising in the large-scale production and high-quality and high-purity growth, all the SWNT samples in this dissertation will be grown with CVD method unless otherwise noted.

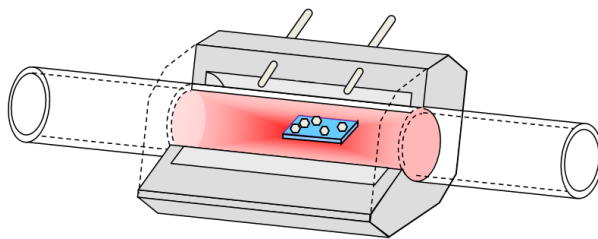


Figure 1.12 Schematic of the CVD furnace. Image modified from [14].

1.4 Growth mechanism

Since their discovery, SWNTs have been produced by various methods using a large variety of metal catalysts and carbon sources with gradually widened growth window [15, 16]. However, the detailed underlying growth mechanism for SWNTs is still under controversy, while many simulations and experimental results show some evidences to disclose a tip of the mysterious story. One of the most popular explanations for the CNT growth is the vapor-liquid-solid (VLS) mechanism [17-19]. However, the hypotheses that the catalyst particles are liquid droplets at growth temperature and the bulk diffusion of carbon are contradictory and misleading [20]. With further modifications and supports, the SWNT growth model by ACCVD method is widely accepted as follows: the ethanol vapor can decompose at the high growth temperature to other carbon species which will be absorbed or adsorbed on the active sites from the catalyst nanoparticles, and the carbon diffusion occur through the corresponding catalyst particles via surface/subsurface diffusion or bulk diffusion. When the particles are saturated, carbon nanotubes can grow from the precipitation of carbon atoms on the catalysts through a top-growth or base-growth model (Figure 1.13).

The decomposition of carbon source molecules can happen at high temperature or due to the promotion of catalyst particles according to the reactivity of carbon sources. Ethanol, acetylene and ethylene can decompose readily at relatively low temperature which is thermodynamically allowed, while the pyrolysis of methane needs higher temperature [20]. Theoretical and experimental results reveal that the products of the carbon source decomposition are small carbon-based molecules or fragments and other byproducts such as

dihydrogen [20-22]. However, the reaction intermediate incorporated into the SWNT growth is an open question. Wang et.al claimed a chirality selection induced by single C atom and a growth of SWNTs with the incorporation of C₂ dimers based on the abounding density function calculations [23]. Chains of carbon atoms are also reported as intermediates to proceed the SWNT growth which is the popular “octopus” model in simulations [24]. An isotopically labeled ethanol is proposed by Xiang et.al to demonstrate the unequal contribution of two carbon atoms in ethanol molecules to SWNT growth and the scission of C-C bond and their preferential incorporation to SWNTs [25].

The next debatable issue is the physical state of catalyst particles at the nucleation and growth stage of SWNTs. The melting point of various metal catalysts for the growth of SWNTs is reduced [26] because of the nanosize effect [27] and the influence of carbon [20]. Due to the diversity of catalysts reported for the growth of SWNTs, the physical state of the catalyst particles for some cases is likely to be solid (diamond) and in other cases is probably liquid (Pb, Au) at the standard growth temperatures (600°C-900°C). The *in situ* TEM observations show the crystal structure during MWNT growth with deformation towards a “pear” shape [28, 29] for the large catalyst particles while the physical state of active catalysts for the growth of SWNTs remains unclear.

The solubility of carbon has been believed to be important for the catalytic ability of metals in the synthesis of SWNTs. An appropriate carbon solubility is required for the carbon diffusion through the catalyst particles [30]. However, the diffusion mode is still under controversy. Generally, the activation barriers for bulk diffusion have been calculated to be significantly higher than that of surface and subsurface diffusions [31]. Insufficient data is available for the dependence of diffusion on the particle size. On the other hand, the chemical state of catalyst during CNT growth is also controversial, especially for the iron catalyst [32]-whether the metal iron or the carbide iron is the real active catalyst for the CNT growth [33-36].

A lot of researchers are devoted to the selective growth of SWNTs towards

semiconducting-pure or chirality-pure properties and much progress has been achieved [37-40]. The selective synthesis of SWNTs always associated with the low yield is mostly contributed to the selective etching effect due to the different reactivity of metallic SWNTs and semiconducting SWNTs [41]. However, the underlying chiral selective mechanism for SWNT nucleation, growth and termination is still unsettled.

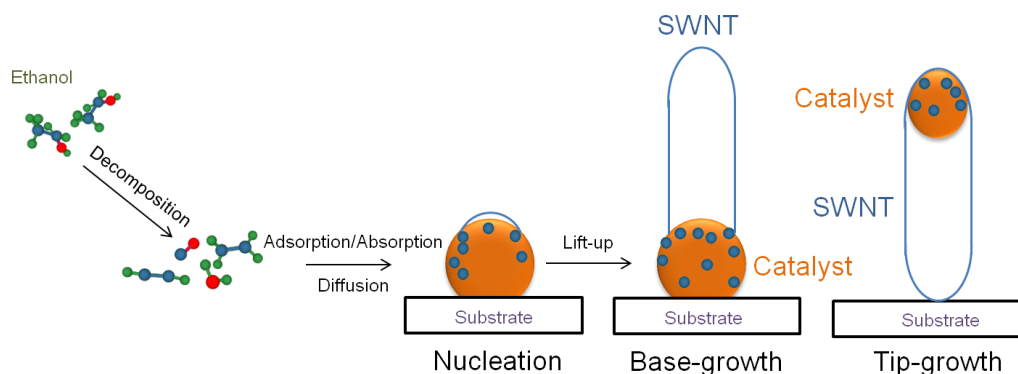


Figure 1.13 Schematic of SWNT growth model.

1.5 Assembly morphology and potential applications

From the nanoscale to the microscale, single-walled carbon nanotubes can take on different shapes and morphologies which will influence the properties and further determine their applications [42-46]. In nanoscale, individual SWNTs have been reported to work as optical sensors, transistors and other nanodevices [47-49]. The first sub-10 nm transistor made from one SWNT has been reported to surpassed silicon competitors in 2012 [50]. Individual SWNT can also work as the gate electrode to reduce the size of transistors into 1 nm [51]. In microscale, SWNTs can exhibit different morphologies including vertically-aligned forests (VA-SWNTs) [52], horizontally-aligned arrays [53, 54], randomly transparent conductive films [55] and spun SWNT fibers [56]. VA-SWNT forests can produce a honey-comb microstructure through water vapor treatment to improve the transparency and conductivity of the SWNT film [57]. Transistors that outperform silicon for the first time are created with carbon nanotube arrays [58]. In macroscale, the honey-comb SWNT film can be utilized in Si-based solar cells resulting in a high efficiency [57]. Random SWNT films are promising in

the applications of transparent conductive films [59, 60] and flexible electronic devices [61].

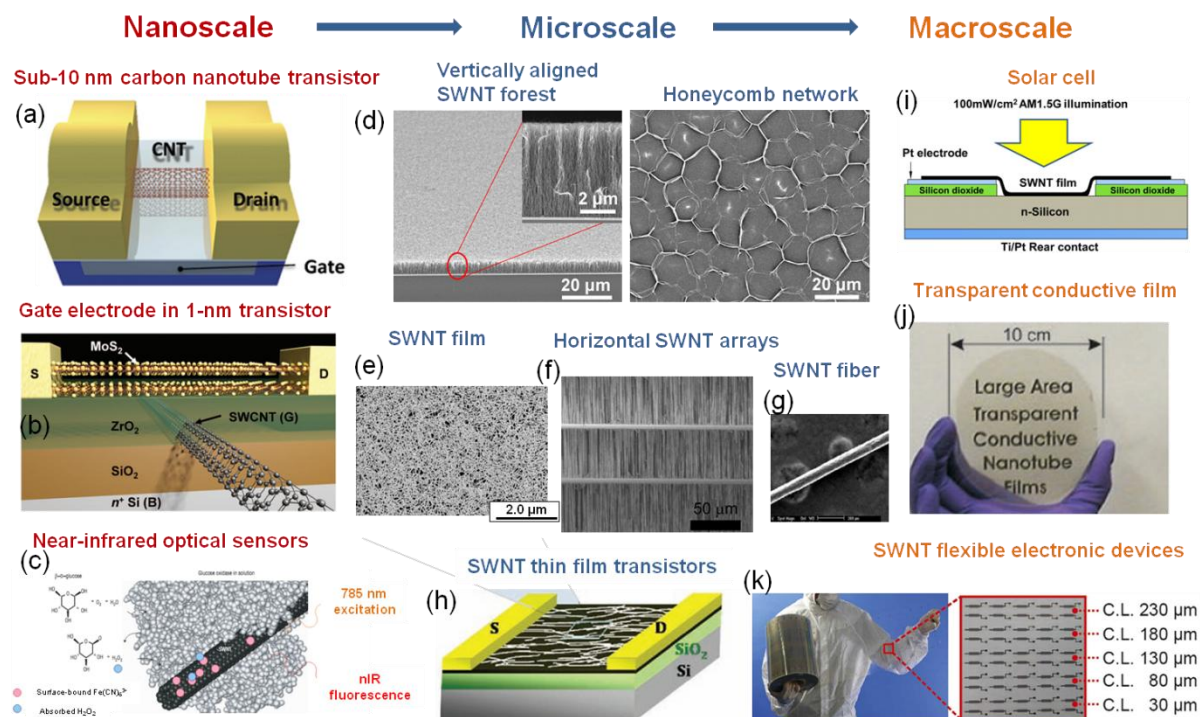


Figure 1.14 Assembly morphologies and potential applications of SWNTs at different scales. (a) Reprinted with permission from [50], Copyright (2012) American Chemical Society. (b) From [51], Reprinted with permission from AAAS. (c) Reprinted by permission from Macmillan Publisher Ltd: (Nature Materials) [47], copyright (2004). (d) & (i) Reprinted with permission from [57]. Copyright (2013) American Chemical Society. (f) Reprinted with permission from [54]. Copyright (2013) American Chemical Society. (g) From [46], Reprinted with permission from AAAS. (h) From [62], Reprinted with permission from AAAS. (j) From [59], Reprinted with permission from AAAS. (k) The authors from Ref [61] and the original source of publication from Nature Publishing group are fully acknowledged.

1.6 Main challenges for the industrial applications

SWNTs attract intensive attention due to their structure-dependent mechanical, electrical, thermal and optical properties in widespread applications. SWNTs are reported to be one of the most important promising building blocks in nano devices because of the rich variety of SWNT chiralities [63, 64]. However, the critical obstacles that inhibit the industrial

applications of SWNTs are that the conductivity-pure and single-chirality SWNT assemblies with homogeneous property can not be produced. Semiconducting SWNTs are highly desired in electronic devices while the metallic SWNTs can significantly degrade their performance [65]. Single-chirality SWNTs can possess the same properties and display the same response to external stimulations which will dramatically improve the performance of the devices. The expected excellent roles that SWNTs can play in the applications are stranded by the as-grown mixtures of semiconducting and metallic SWNTs with broad chirality distribution [66]. The difficulty for the controlled synthesis of single-chirality SWNTs lies mainly in the lack of proper understanding of growth mechanisms [67]. The experimental investigation to disclose the hidden story in the selective growth of SWNTs requires high resolution in-situ method which is not always possible for researchers. These lead up to the main challenges for the industrial applications of SWNTs-insufficient production and uncompetitive cost of SWNTs, lack of understanding of the growth mechanism, chirality-controlled and diameter-controlled growth of SWNTs.

1.7 Motivation, objective and organization of this dissertation

As discussed in the last section, the motivation and final objectives in this dissertation is to control the chirality of as-grown SWNTs with bimetallic catalysts and to understand the growth mechanism better with the proposed in-plane TEM method and endeavor to achieve the ultimate goal of single-chirality SWNTs.

Accordingly, the dissertation comprises of three main parts in the following. It will start with the experimental methods used in the synthesis and characterization of SWNTs and catalyst particles. The normal methods are briefly introduced and one novelly developed in-plane TEM is emphasized together with the successful advantages in the study of growth of small-diameter SWNTs using sputtered CuCo catalyst.

The most important contributions in this dissertation is the selective growth of (12, 6) SWNTs with sputtered W-Co bimetallic catalyst system. The as-grown SWNTs are characterized with Raman and optical absorption spectroscopy to estimate the content of (12, 6). The catalyst structure is investigated by in-plane TEM method and the crystal structure of catalysts is assigned by electron diffraction.

Further confirmation of the composition of as-reduced catalyst particles is realized and more detailed time-dependent investigation illustrates a complicated structure evolution process with this special bimetallic catalyst which will further guide us in the selective growth of SWNTs.

Chapter 2 Experimental methods

The second chapter will mainly focus on the experimental methods for the synthesis and characterization of SWNTs. Sputtering and dip-coating are used for the preparation of catalysts on substrate or supported materials. The as-grown samples are attached with carbon tape to check the morphology of SWNTs with scanning electron microscope (SEM). Renishaw in Via with four different excitation lasers (488 nm, 532 nm, 633 nm, 785 nm) and optical absorption spectroscopy is conducted to characterize the optical response from the SWNT samples. An in-plane TEM method can maintain the original structure of catalyst particles and SWNT morphology on Si/SiO₂ microgrid providing an efficacious way to study the underlying growth mechanism of SWNTs.

2.1 Preparation methods for catalysts

2.1.1 Dip-coating

Dip-coating is a typical and simple method for the preparation of catalysts for SWNT growth which was first introduced in 2003 in our group [68]. This method shows better controllability and uniformity than the drop-casting in the liquid-coating process. The schematic is shown in Figure 2.1. Typically, the cobalt acetate and molybdenum acetate are used as the catalyst precursors which can be tuned according to the purpose. The precursors are dissolved in ethanol solution with a typical concentration of 0.01 wt% and then sonicated for 1 h. During sonication, Si/SiO₂ substrate is annealed at 500°C and cooled for 5 min which can be used for the next step. After sonication, the prepared solutions show pink color for Co

and yellow for Mo respectively. Once everything is done, the substrate is submerged into the yellow Mo solution for 4 min first, and then withdrawn from the solution with a controlled speed of 6 cm/min. The substrate is annealed at 400°C in a small furnace in air. After cooling down to the room temperature, the substrate is immersed into the pink Co solution with a similar process. Then the prepared substrate is ready for ACCVD growth.

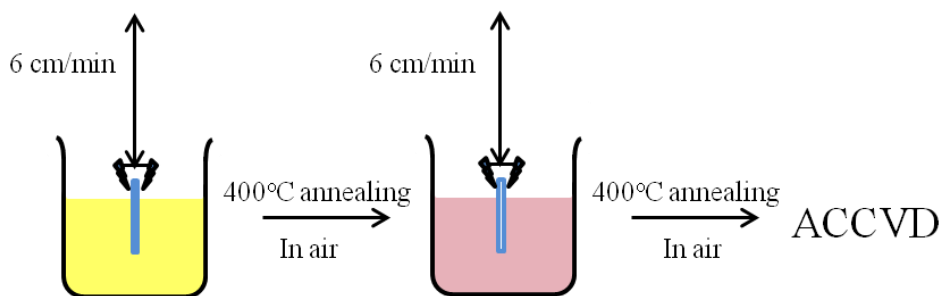


Figure 2.1 Schematic of dip-coating method

2.1.2 Magnetron sputtering

The second important method used for the preparation of catalyst in this dissertation is magnetron sputtering. Magnetron sputtering is established for the deposition of various kinds of coating materials with good controllability and high-quality film and has been widely applied in industrial coating. This method is important for the large-scale coatings especially for the high-melting-point metal and metal oxide [69]. Various parameters including electrode target, power, vacuum pressure and deposition time allow a maximum possibility to control the deposition process. A typical magnetron sputtering is a plasma-assisted deposition process at high vacuum condition. Normally, the chamber is first pumped to 5.0×10^{-4} to 1.0×10^{-5} Pa, and inert gas is flowed (Ar gas in our case). With the high electrical field around the target material, Ar plasma ions are created with positive charge and strike the target of the desired coating material. The Ar positive ions have sufficient energy to dislodge the target atoms from the bulk surface, then these atoms eject to the chamber space and some of them can go to the substrate sample and bond on the surface. In the case of CuCo and W-Co bimetallic catalyst systems, silicon substrates are deposited with two different layers of catalyst

separately and annealed at 400°C in air right after sputtering. In order to investigate the sequence of different metal materials, sputtering can be done by changing the deposition sequence and co-sputtering method.

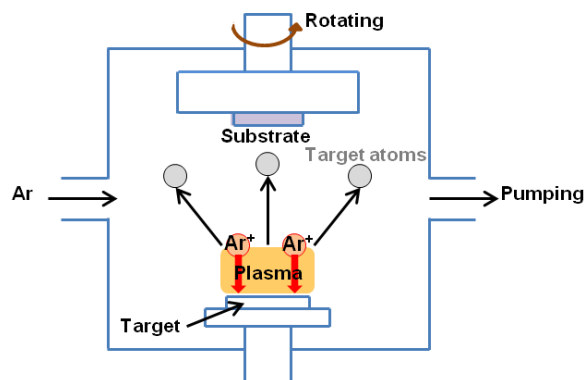


Figure 2.2 Schematic of magnetron sputtering method.

2.2 Synthesis of SWNTs

Alcohol catalytic chemical vapor deposition (ACCVD) was first proposed by Maruyama group, and then rapidly developed to grow large-scale carbon nanotubes with high quality and low cost [10]. The detailed setup is shown in Figure 2.3. The aforementioned substrate with catalyst loaded by dip-coating or sputtering is placed in a parallel orientation to the gas flow direction in a quartz tube chamber with the diameter of 25 cm and then pumped to vacuum (typically 25 Pa). Both the sub drain valve and butterfly valve are closed for 5 min to check the leakage of the CVD system. After that, Ar gas is flushed for 5 min to remove water and air in the chamber. After the pretreatment, the chamber is heated to the growth temperature (ranges from 600°C to 900°C) with a mixed Ar/H₂ (3%H₂) gas to reduce and anneal the catalyst particles to proper size before the growth of SWNTs. Upon reaching the target temperature, a more 5 min reduction procedure is necessary for further reduction, and then the ethanol gas is introduced to the chamber with a controlled flow rate and pressure. Growth time is determined by detailed purpose which can be easily control. After the growth, ethanol is stopped quickly and the butterfly valve is opened fully and the temperature is reset for cooling with a flushed Ar gas to the room temperature. Finally, the quartz tube is filled

with Ar gas and the sample can be taken out for further characterization.

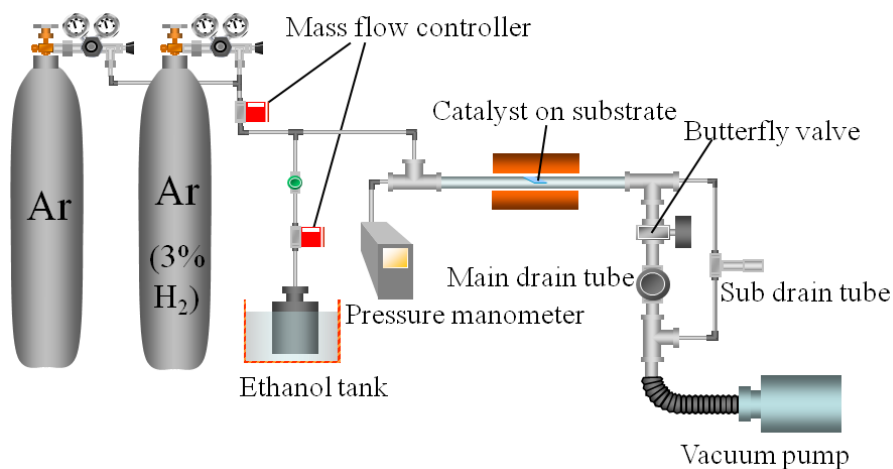


Figure 2.3 Schematic of ACCVD setup. Modified from [70].

2.3 Characterization of SWNTs

In order to analyze the structure and chirality distribution of the as-synthesized SWNTs, various methods are utilized from the optical way such as Raman and absorption spectroscopy to the microscopic way to illustrate the nanoscale single-walled structure by transmission electron microscope (TEM) and the microscale assembly morphology by scanning electron microscope (SEM).

2.3.1 Raman spectroscopy

Raman is a powerful tool for the characterization of materials because of its high sensitivity, easy operation and control, nondestructive measurement, applicability for versatile states of samples (solid, liquid and trace detection) [71].

When the incident light interacts with a material, the light can be absorbed or scattered if the light energy is consistent with the energy gap from the ground state to any excited state. The scattering process can be elastic scattering without energy loss which is the case of Rayleigh scattering or inelastic scattering with the loss of energy which is Raman scattering process.

The electrons are excited due to the absorption of energy from the ground state to excited states and will emit photons when return to the lower energy states. This process is Stokes scattering process. On the other hand, if the excited electrons from vibrational states emit photons when relax to the ground state, it is anti-Stokes scattering process. The scattering process can be measured by the intensity of emitted photons with a loss of energy (frequency shift), that is the Raman spectrum [72]. When the excitation energy is close to the energy gap of SWNTs, the Raman scattering intensity is enhanced, and this is due to the resonant effect [73]. Thus Raman scattering of SWNTs is a resonant process selecting specific chiralities whose electronic density of states match with a laser frequency [73].

Figure 2.4 shows a typical Raman spectrum for a SWNT sample with an excitation laser of 488 nm. Three important features from the spectrum can be obtained to interpret the chirality structure and purity of the sample.

One of the most distinct peaks is the G band of SWNTs which is located in high frequency region. The G band at 1590 cm^{-1} is a typical feature for the hexagonal carbon structure related to the tangential vibrational mode of carbon atoms of SWNTs. Different from the single Lorentzian peak of graphite, G band for SWNTs splits into several peaks due to the confinement of the phonon wave vector along circumferential direction and the symmetry-breaking effects because of the curvature [2]. As shown in Figure 2.4, G band can split into two peaks, G^+ band and G^- band. G^+ band can be assigned to the vibrations of carbon atoms on the graphene cylinder along the axial direction as shown in the vertical arrows in Figure 2.4. On the other hand, G^- band originates from the vibrational modes of carbon atoms on the graphene cylinder along the circumferential direction shown as the horizontal arrows in Figure 2.4. The lineshape of G^- band is associated with the electronic property of SWNTs [74] and the typical G bands for the metallic and semiconducting SWNTs are shown in Figure 2.4. In the case of metallic SWNTs, a broadened peak of G^- band can be observed which is called Breit-Wigner-Fano (BWF) feature related to the charge transfer of SWNTs [75].

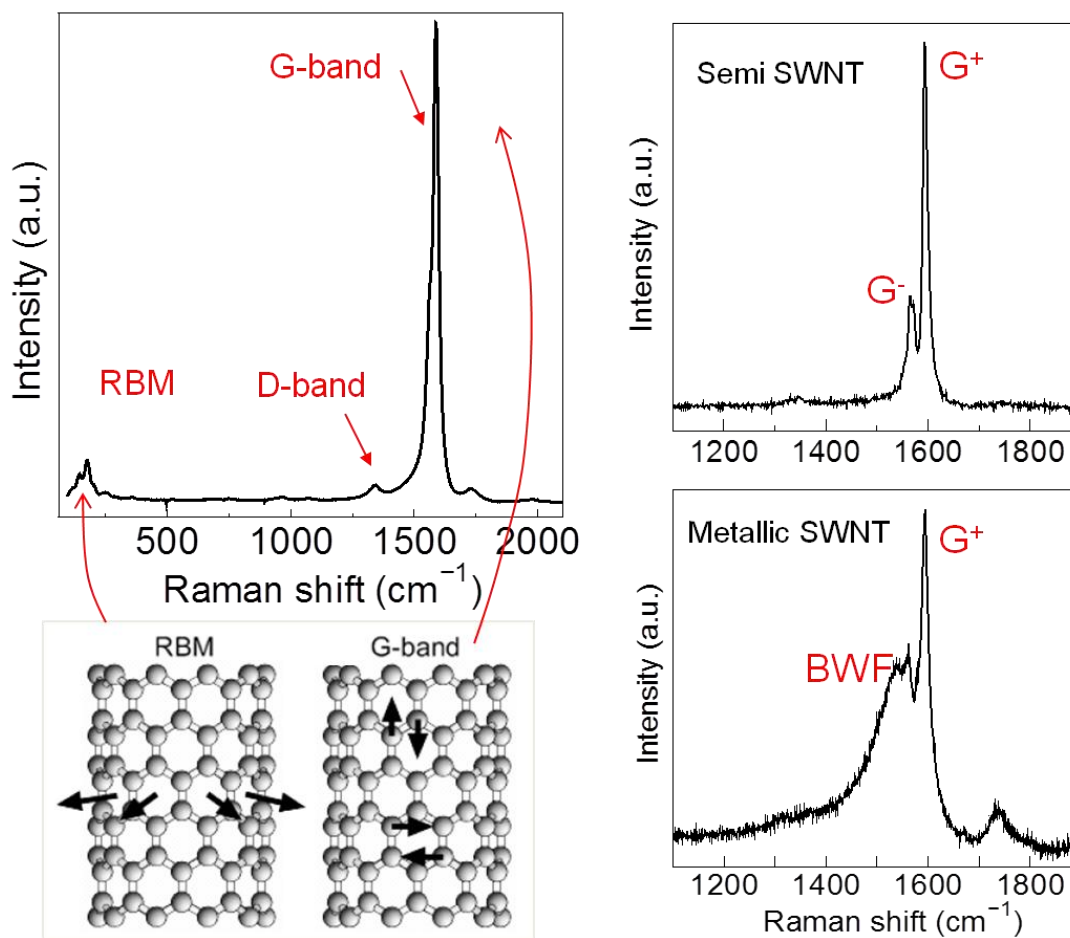


Figure 2.4 Typical Raman spectra of SWNTs showing different signals with corresponding vibration modes. Image modified from [76]. The authors from Ref [76] and the original source of publication from IOPscience are fully acknowledged.

Of particular importance is that the frequency for G^+ band is almost independent on the diameter and chirality, however, for the G^- band, the frequency is sensitive to the diameter of SWNTs and the degree of dependency is associated with metallic or semiconducting type of the SWNTs, providing an supplementary method for the judgment of diameter of SWNT sample by Raman spectrum [77].

Another characteristic peak close to G band is D band at around 1320 cm^{-1} . D band is derived from a Raman active disorder mode of symmetry-lowering effect due to the defective hexagonal network from pentagons and heptagons, bending of graphene cylinder, the existence of carbon nanoparticles and amorphous carbon [3]. The intensity of D band is

sensitive to the quality of SWNTs which is almost indistinguishable for the highly crystallized and defect-free SWNTs and thus ratio of I_G/I_D is a good index to evaluate the quality of as-grown SWNT samples by combining the defective D band and the graphitic G band [78-80].

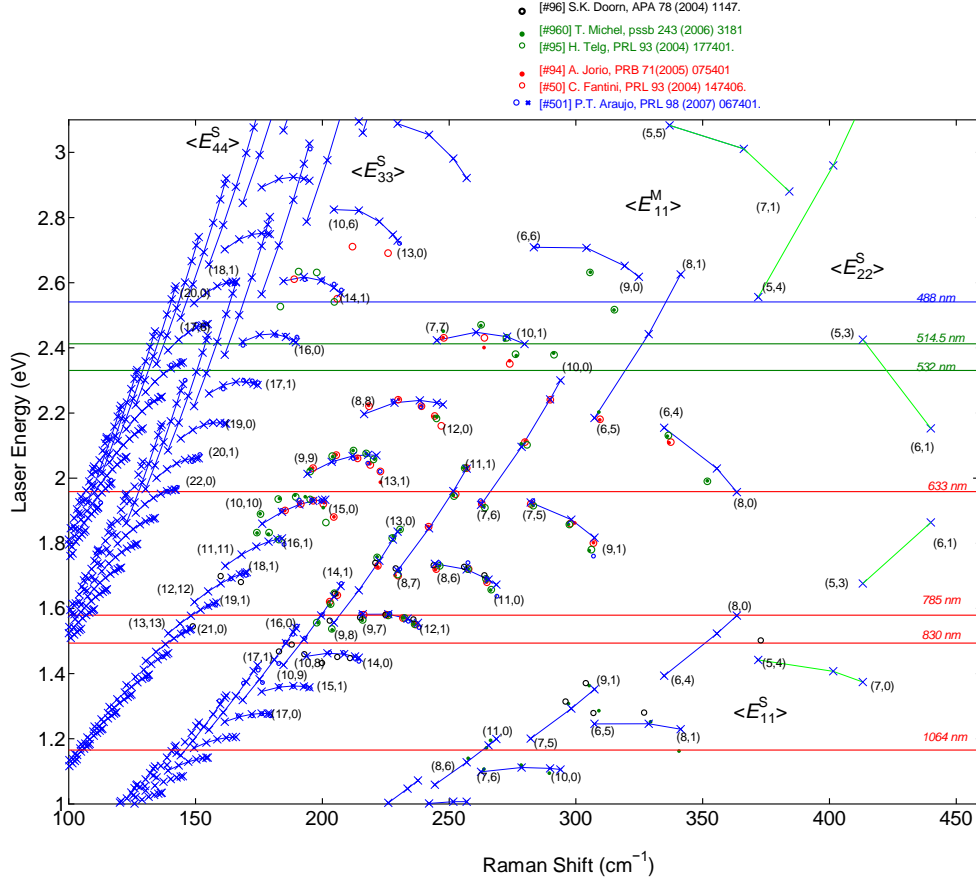


Figure 2.5 Kataura plot for the relationship of electronic transition energy and SWNT diameter with widened RBM region.

The peaks in the low frequency region (50-500 cm⁻¹) are the radial breathing mode (RBM) correlated to the coherent vibrations of carbon atoms in the radial direction [81]. The RBM feature is unique to single-walled carbon nanotubes and the frequency is inversely proportional to SWNT diameter with a relation of $\omega_{RBM} = A/d_t + B$, where A and B are empirical parameters depending on the surrounding conditions of SWNTs (bundled or not, interaction between SWNT and substrate etc) [82]. With this relation, the diameter of SWNTs can be obtained from the measurement of ω_{RBM} , and the indices of (n, m) can be determined

by Kataura plot based on the electronic transition energy resonant with the laser wavelength and the nanotube diameter [83]. Figure 2.5 shows the Kataura plot with a widened RBM region from our lab. Owing to the limitation of resonant effect, the RBM peaks from one laser is not a complete detection for the SWNT samples, thus different laser wavelengths are needed for the characterization of the chirality distribution by Raman [84]. It is important to point out that for large-diameter SWNTs, the RBM (less than 50 cm^{-1}) is hardly observable due to the weak intensity [2].

A commercial Renishaw in Via Raman spectroscopy will be utilized in this dissertation with four different lasers at the excitation wavelength of 488 nm, 532 nm, 633 nm, 785 nm. The detailed chirality distribution will be discussed in the following chapters for different catalyst systems. A Raman mapping measurement can be readily conducted with this microscope for SWNTs grown on flat substrates. The steps of the mapping arrangement can also be controlled by the commercial software which allows a statistical way of counting the RBM peaks to further analyze the chirality distribution.

2.3.2 Optical absorption spectroscopy

For the synthesis of SWNTs, not only the growth itself is important, but also a quick and reliable characterization which can immediately show the structure and chirality distribution of as-grown SWNTs in the sample is essential for the goal towards selective growth. Even though Raman spectroscopy shows a significant potential in the quick measurement [85], there are also some limitations. Because of the resonant effect, the signals from Raman spectrum in RBM region can only show a limit number of SWNTs existing in the sample [86]. For the RBM peaks excited by one laser, we can not tell the content of each chirality by comparing the peak intensity. The continuous laser is possible for detecting all the existing SWNTs but it seems not applicable for all laboratories. Photoluminescence excitation spectroscopy (PL) can act as a more powerful way to characterize the chirality distribution of dispersed SWNT samples showing the unambiguous identification of chiralities and the distribution with the peak intensity [87]. However, the PL signals from metallic SWNTs are

annihilated by electron-electron scattering and phonon-mediated relaxation process [88], thus the PL can only detect semiconducting SWNTs in the sample [89]. Compared to the previous two optical methods, absorption spectroscopy shows powerful and reliable ability to detect the average diameter of the SWNT samples including metallic and semiconducting SWNTs without resonant effect and is applicable to the SWNT films for non-destructive measurement and dispersed SWNT solutions for individual SWNT chirality assignment [90, 91].

Apart from scattering, when the light interacts with a matter, the incident photons can also be absorbed if the photon energy matches with the energy gap promoted from the ground state to the excited states. According to Beer-Lambert law, the absorbance of a sample is proportional to its thickness with an exponential relation. Due to the unique one dimensional feature of SWNTs, the absorption is strongly related to the discrete vHS of DOS. For a certain SWNT sample, the absorption happens when the energy gap of vHS corresponds to the incident photon energy. The electronic transitions can occur with the same order denoted as S_{11} , S_{22} ... for semiconducting SWNTs and M_{11} ... for metallic SWNTs. By referring to Kataura plot and the obtained electronic transition energies from absorption spectrum, chirality distribution of the SWNT sample can be identified. Of the same interest is that the intensity of the absorption is determined by the absorbed photon quantity which is dependent on the content of the corresponding chirality, thus the peak intensity of absorption spectrum indicates the enrichment of a certain chirality. Because of the rich diversity of SWNTs, discrete vHS and different electronic transitions, the absorption may overlap with different chiralities [92]. By combining the Raman spectrum with the optical absorption spectrum, the assignment of (n, m) is more reliable and the quantitative analysis becomes possible.

In the case of SWNT film grown from Co, CoMo and CuCo catalysts, the absorption measurement is taken at solid state which is a quite simple shown in Figure 2.6. A transparent bare quartz substrate is used to measure as the baseline, then the SWNT film on the quartz substrate which is transferred from the Si/SiO₂ substrate or grown directly on the fused quartz substrate is measured to obtain the absorption spectrum. Due to the bundles in the SWNT

film, the absorbance peaks are broadened and can be roughly used to evaluate the mean diameter in the film sample shown in figure 2.7.

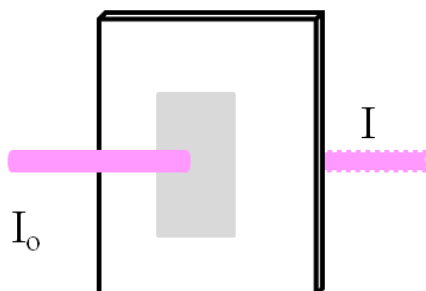


Figure 2.6 Schematic for the absorption microscopy measurement of SWNT film on quartz substrate.

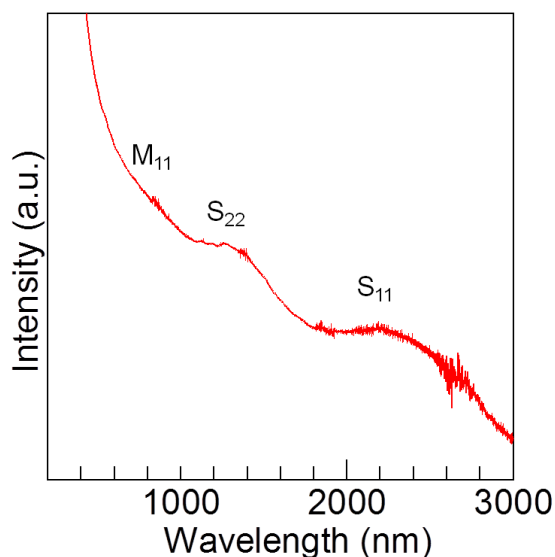


Figure 2.7 Typical absorption spectrum for the SWNT film.

In the case of SWNT sample grown from W-Co catalyst, since the yield is not high enough to measure directly on the quartz substrate, a more common liquid method is used [93]. The randomly collected samples grown directly on the Si/SiO₂ substrate are sonicated in the deuterium oxide (D₂O) solution with sodium dodecyl sulfate (SDS) as a surfactant. Then centrifugation is conducted in order to remove the scraps from Si/SiO₂ substrate and the stripped catalyst particles. After that, the supernatant is collected. Before measurement, the D₂O solution with the same SDS concentration is taken as the baseline, and the SWNT

solution is measured as illustrated in figure 2.8. In the well dispersed SWNT solution, individual SWNTs encapsulated by the surfactant show sharp absorbance peaks in the spectrum shown in figure 2.9, and the corresponding chirality can be assigned based on Kataura plot.

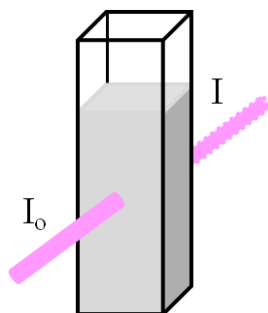


Figure 2.8 Schematic for the absorption microscopy measurement of SWNT suspension.

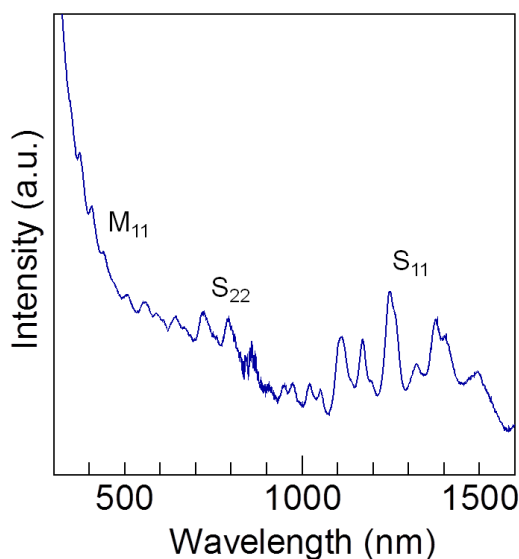


Figure 2.9 Typical absorption spectrum for the dispersed SWNTs.

2.3.3 Scanning electron microscopy (SEM)

SWNTs can take on various morphologies, such as SWNTs forest, mat, grassy network, and individual SWNTs randomly distributed on the substrate. In order to effectively characterize the morphology of SWNTs, scanning electron microscopy is widely used. Researchers have successfully grown horizontally aligned SWNT arrays on crystal substrate based on electrical

field, substrate and gas flow guided interaction which can be seen through SEM [94-97]. According to the conductivity of SWNTs, we can judge whether a SWNT is metallic or semiconducting with the different contrast on substrate by SEM [98].

Scanning electron microscopy is a method scanning the surface of a sample with focused fine electron beam and detecting the signals from the sample. The basic signals include for example secondary electrons, back-scattered electrons and so on. Not only the secondary electrons (common mode) but also the back-scattered electrons come from the surface of the sample (within tens of nanometers), thus SEM is a tool to detect the surface topography. The samples for SEM need to be conductive. If not, the samples should be deposited with a thin metal layer on the surface, such as Au. In the case of SWNT samples, it is conductive and can be effectively characterized by SEM. The typical SEM images of SWNTs with different morphologies are shown in Figure 2.10.

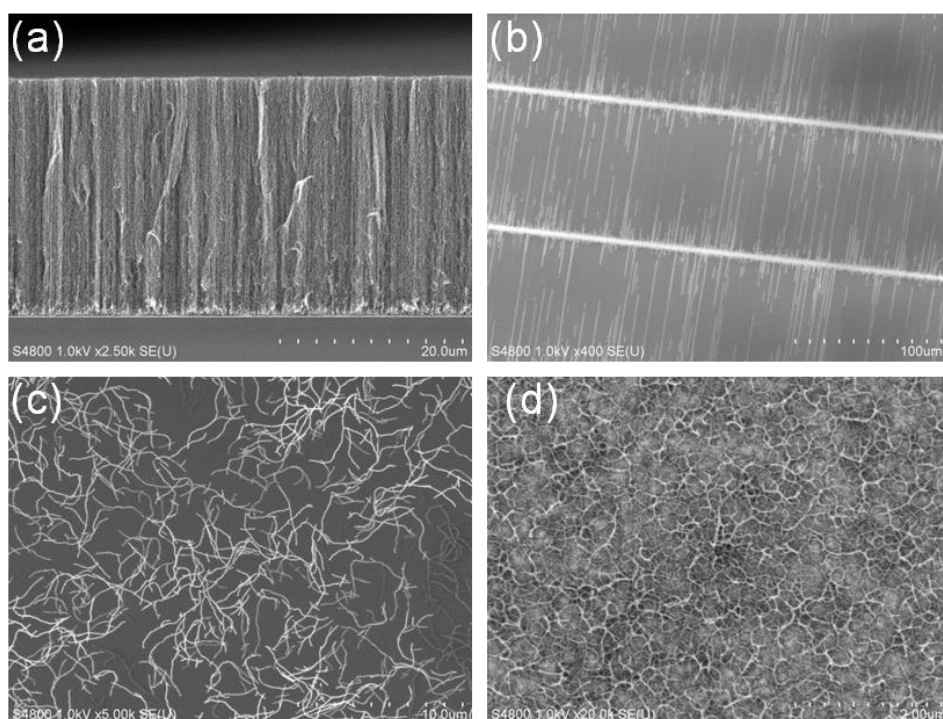


Figure 2.10 Typical SEM images of SWNTs with various morphologies. (a) Vertically aligned SWNT forest, (b) Horizontally aligned SWNT arrays, (c) Randomly SWNT network, (d) SWNT thin film on substrate.

2.3.4 Transmission electron microscopy (TEM)

Besides SEM, TEM is another powerful means to confirm the existence of CNTs which has played an important role in the breakthrough discovery of multi-walled CNTs and SWNTs [4, 99]. Compared with SEM which detects the secondary electrons or back-scattered electrons for imaging, TEM images the signals after a beam of electrons transmitting and interacting with a thin sample on a layer of photographic film or by a sensor such as a CCD camera. Explicit images of CNTs can be obtained by TEM showing the diameter, wall number, the connection structure with catalyst particles and different morphologies and shapes by high resolution TEM [52, 100]. The existence or nonexistence of catalyst particles can clearly tell the purity of a specimen as shown in figure 2.11.

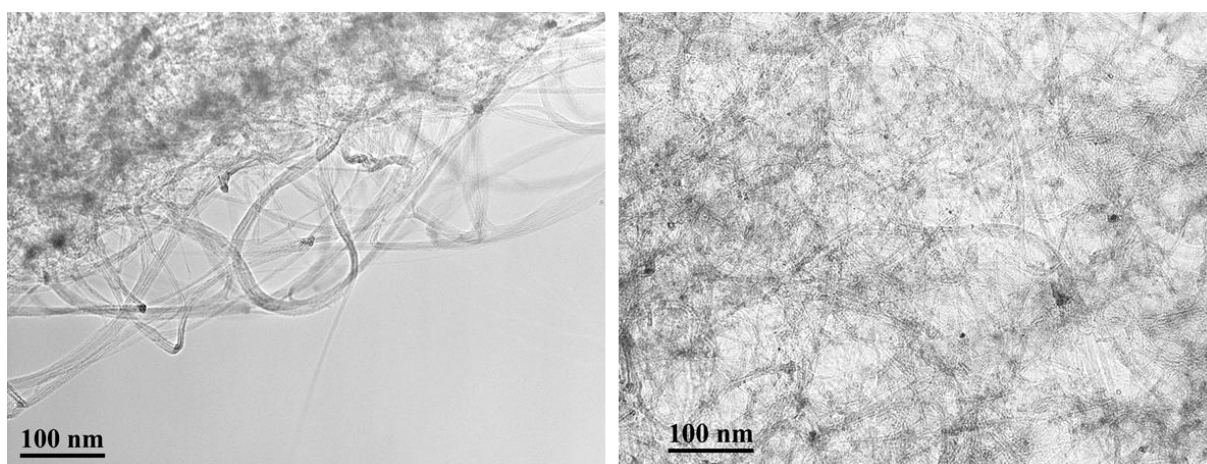


Figure 2.11 Typical TEM images of SWNTs

2.3.5 Electron diffraction

Because of the feature of wave-particle duality, electron beam can also be regarded as a wave. When electron beam passes through a matter with regular arrangement in atomic level, it can produce a diffraction phenomenon which can be understood by the diffraction of light called Huygens-Fresnel principle [101]. The regular arrangement of atoms can be regarded as an atomic scale lattice plane as shown in figure 2.12. When the incident light interacts with a crystal, the interplanar spacing leads to the interference between the secondary waves and a set of electron diffraction pattern can be generated. The interplanar distance d and the

incident angle θ can be related with wavelength of the electron beam with a Bragg law:

$$n\lambda = 2d\sin\theta$$

If we know the electron wavelength λ , the interplanar distance can be calculated with the obtained electron diffraction pattern and the specific crystal structure can be determined consequently. Electron diffraction represents a viable tool in the field of phase identification.

Electron diffraction patterns can exhibit different forms. A pair of spots can be generated with a perfect single crystal sample. However, if the sample is composed of many nano particles in random orientations, the diffraction spots from various planes can form a ring pattern shown in figure 2.13 [102]. The electron diffraction of nanomaterials can be performed in the transmission electron microscope with a selected area region. The resultant selected area electron diffraction pattern can be displayed on a photographic film where a lot of information on the crystal structure can be obtained [103, 104].

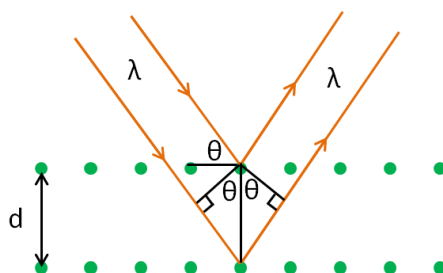


Figure 2.12 Schematic of electron diffraction process.

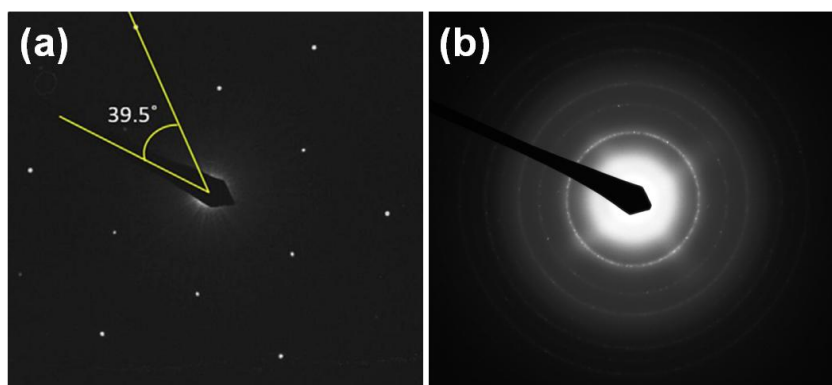


Figure 2.13 Typical electron diffraction patterns for single crystal (Reprinted from [102], Copyright(2016) with permission from Elsevier) and polycrystal samples.

2.3.6 In-plane transmission electron microscopy (TEM)

Catalyst plays a critical role in the formation of SWNTs, while obtaining the intrinsic structure and morphology of these nano-sized particles at growth or near-growth conditions remains challenging [105, 106]. Here, we have developed an in-plane TEM approach (figure 2.14) which enables a direct characterization of catalyst particles with atomic resolutions on an amorphous Si/SiO₂ micro grid with good uniformity. This microgrid can be stable up to 1000°C which makes direct growth of SWNTs on the microgrid and the in situ TEM observation possible and does not need transfer that means we can get the catalyst structure consistent with wafer substrate and will not lose any information. This in-plane view of catalyst gives comprehensive and statistical information in a large area on the uniform flat substrate from many particles. The collective (rather than localized) information from many particles can be obtained simultaneously by TEM imaging and electron diffraction. With this technique, we will systematically study the behaviors of bimetallic catalysts including CuCo, and W-Co in the growth of SWNTs and propose a possible mechanism accordingly. Sputtering method comes to our eyes due to its uniformity, simplicity and the universality, making it possible to systematically explore all the possible metal catalysts for the growth of SWNTs and their roles in the diameter and chirality control [107].

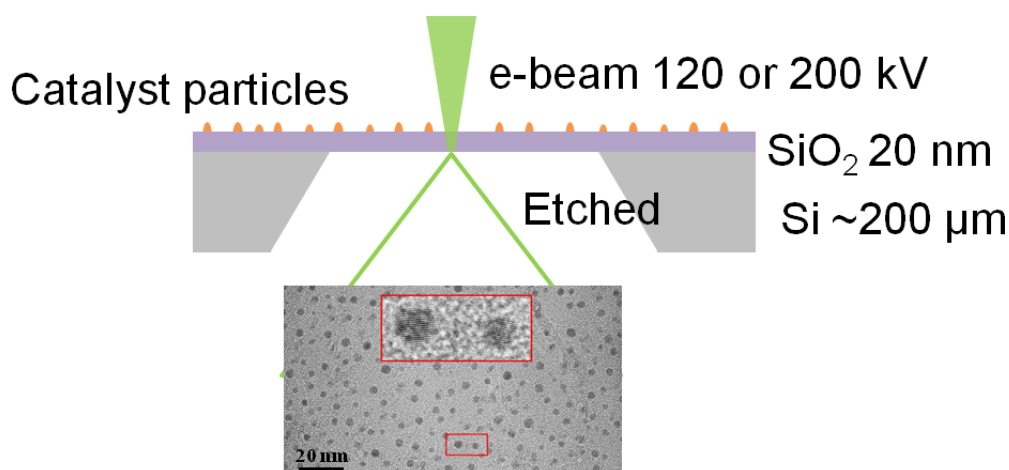


Figure 2.14 Schematic for in-plane TEM.

2.3.7 Application of in-plane TEM in the study of synthesis of small-diameter SWNTs with CuCo

Small-diameter semiconducting SWNTs with large band gap are promising alternatives to improve the performance of wide-bandgap semiconductors [108]. Bimetallic catalysts have shown excellent catalytic properties in the synthesis of small-diameter SWNTs [109, 110]. In our previous study, dip-coated CuCo can successfully grow sub-nanometer vertically aligned SWNT forest at low temperature [111]. The CuCo catalyst deposited by sputtering method can be utilized for the investigation of CuCo catalytic growth of small-diameter SWNTs with in-plane TEM method.

To understand the bimetallic effect of CuCo in the growth of SWNTs better, pure Co catalyst is sputtered with the same parameter as a comparison. With the aid of SEM, we can see that sputtered Co can efficiently grow vertically-aligned SWNT forest with high density at a relatively low temperature of 700°C in figure 2.15. What's in sharp contrast is that the SWNTs grown from CuCo at 700°C show sparse film randomly laying on the substrate with much lower yield than the forest from sputtered Co. By increasing the growth temperature, the yield which can be displayed by the thickness of the film improves to a thick network mat at CuCo800°C. The nice and clean SWNT bundles show “Y-shape” in the SEM images and the thickness of the film is less than 1.0 μm . The SWNTs grown at 800°C with both CuCo and Co exhibit a similar morphology. However, compared to the tendency of increasing yield in CuCo system with the increase of temperature, the Co catalyst at 800°C produces less SWNTs than the vertically aligned forest. This may be related to the density of active catalyst particles during CVD process.

The Raman spectra in figure 2.16 show the diameter distribution of SWNTs grown from two catalyst systems at different temperatures which is labeled as Co700°C, CuCo700°C, Co800°C, CuCo800°C. In the RBM region, the peaks at $\sim 100\text{ cm}^{-1}$ from Co700°C signify the existence of large-diameter SWNTs [112]. Note that the growth of large-diameter SWNTs in CuCo700°C is almost suppressed by the addition of Cu. The low temperature can grow

small-diameter of SWNTs which is consistent with the blue shift of the RBM peaks by comparing the 700°C and 800°C samples in CuCo catalyst system. On the other hand, from the perspective of the catalyst, the introduction of Cu can favor the growth of small-diameter SWNTs at both 700°C and 800°C. Furthermore, the reduction of diameter at 700°C is much more significant than that of 800°C with the introduction of Cu into Co catalyst showing an optimum functional temperature of Cu. It indicates that the introduction of Cu can facilitate the growth of small-diameter SWNTs at relatively low temperature which offers a possible strategy to produce large band gap SWNT samples to promote the applications of SWNTs in nanoelectronics [113-115].

What's more important is that the I_G/I_D ratio of the as-grown SWNTs is quite high suggesting a high quality and high purity of SWNTs in the Raman spectrum shown in figure 2.16. Since the frequency of G^- peak in Raman spectrum has been claimed to be another method to estimate the diameter of SWNTs and the G^- band frequency reduces with the decrease of SWNT diameter while the G^+ band stays constant [77], note that the red shift of the G^- band in figure 2.16 is more impressive at low temperature and with CuCo bimetallic catalyst indicating the small diameter of SWNTs.

A more visible comparison of the effect of Cu on Co in the synthesis of small-diameter SWNTs at low temperature is shown in the optical absorption spectrum in figure 2. 17. The significant blue shift of the S_{11} peaks at low growth temperature (from CuCo700°C to Co700°C) indicates a great reduction of diameter with the introduction of Cu to Co catalyst while the SWNTs grown from Co and CuCo at 800°C show similar absorbance. This interesting result tells us that Cu is more effective in decreasing the diameter of SWNTs at low temperature than that of high temperature. It suggests that an effective strategy to lower down the optimum growth temperature of SWNTs with better diameter controllability may be to utilize an anchoring metal with low melting point. The effect of the metal with low melting point is more effective at low temperature rather than high temperature based on the interaction of the bimetallic components. The optical absorption spectrum of CuCo 700°C

shows dominant peaks assigned to (6, 5) and (7, 6). The SWNT film demonstrates a narrow chirality distribution and the dominant S_{11} and S_{22} peaks indicate the enrichment of semiconducting SWNTs suggesting a high potential in the electronic devices where semiconducting SWNTs are highly desirable.

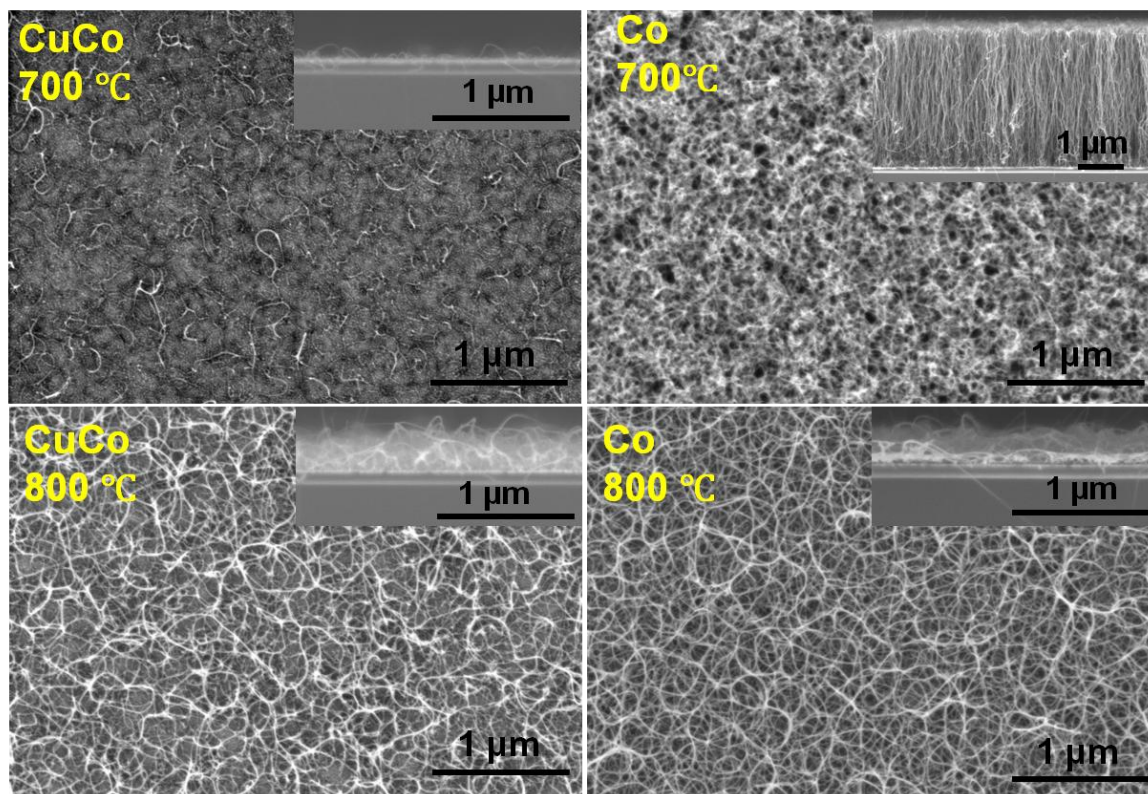


Figure 2.15 SEM images of SWNTs grown with sputtered Co and CuCo at 700°C and 800°C.

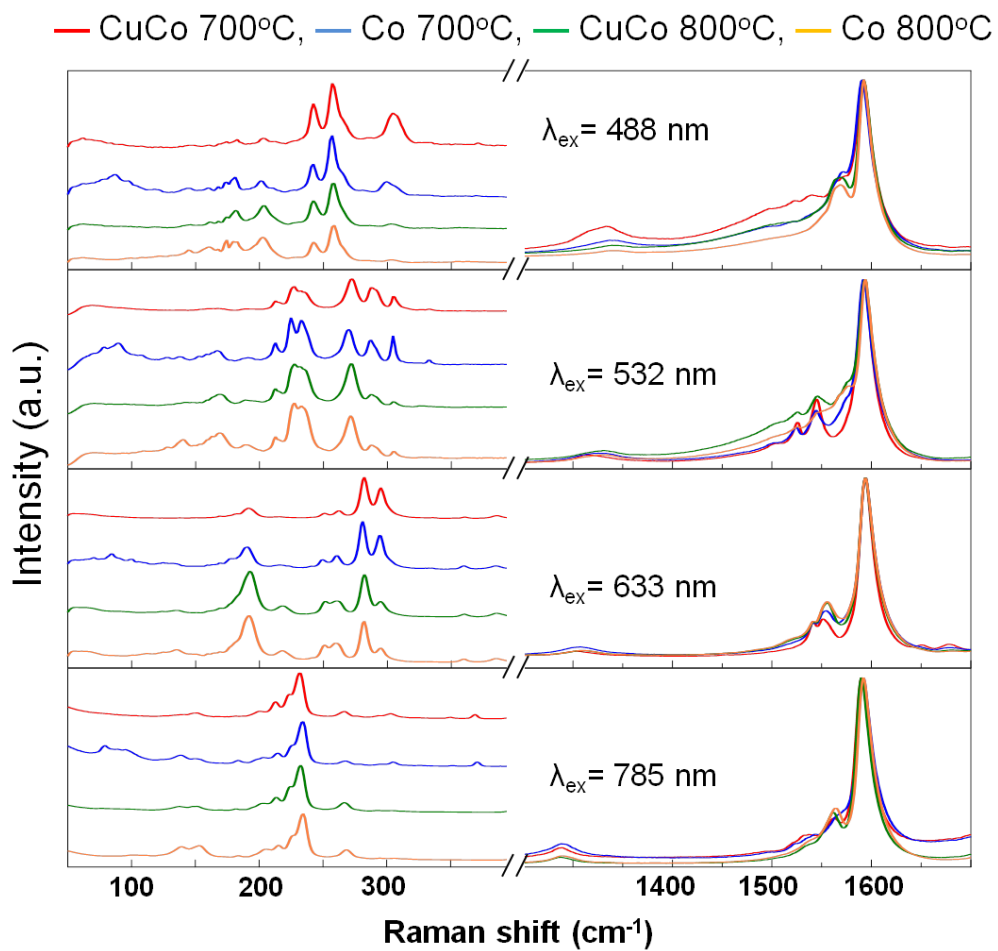


Figure 2.16 Raman spectra of SWNTs grown with sputtered Co and CuCo at 700°C and 800°C.

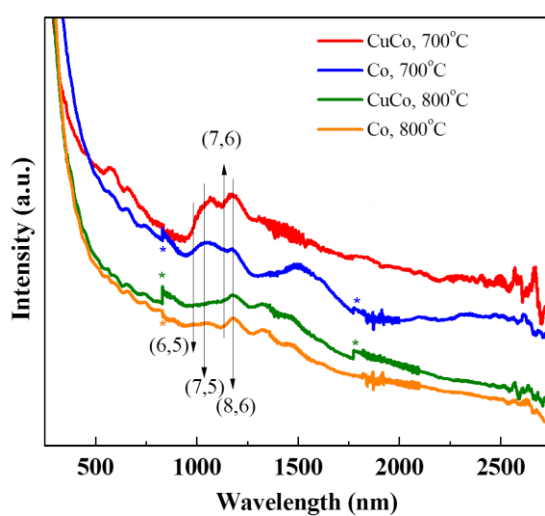


Figure 2.17 Absorption spectra of SWNTs grown with sputtered Co and CuCo at 700°C and 800°C.

In order to investigate the possible mechanism and propose a practical explanation of the growth of small-diameter SWNTs with CuCo at low temperature, the in-plane TEM method is conducted. CuCo bimetallic catalyst and monometallic Co catalyst for control experiment were prepared by magnetron sputtering on the Si/SiO₂ microgrid with exactly the same parameters of wafer substrate. The two microgrids were then undergone a heating process in 300 sccm Ar/H₂ (3% H₂) and reduced at 700°C for 5 min. After the reduction, the furnace was then cooled down to room temperature and the grids were kept in an Ar/H₂ (3% H₂) environment for the whole night before TEM observation to minimize the oxidation of the reduced metallic particles. Figure 2.18a and b show the resultant TEM images of Co and CuCo catalyst. Co particles in a few nanometers are uniformly distributed on the microgrid substrate. Metallic Co and oxidized Co particles due to the exposure to air are displayed with different contrast in which dark parts are metallic Co while the weak contrast ones are CoO because of the different scattering factors [116] and the lattice structure can be recognized in the high-resolution transmission electron microscopy (HRTEM). In the case of CuCo, large particles spread on the microgrid with different contrast in different parts showing the property of polycrystallinity. Among them, small particles intersperse around the larger ones showing two sets of nanoparticles with different sizes. The detailed size distribution of two catalyst systems is summarized and fitted in the histogram in Figure 2.18 b and d. The Co catalyst is fitted by a Gaussian curve showing a narrow size distribution ranging from 2 nm to 5 nm at an average diameter of 3.5 nm. Different from the Co catalyst and consistent with the TEM images, CuCo bimetallic catalyst exhibits a bimodal size distribution fitted by two Gaussian curves at an average size of 1.72 nm and 6.80 nm respectively. The introduction of Cu to Co catalyst system results in narrower-distributed small-size particles and broader-distributed larger-size particles. The role of substantial change of catalyst size on the growth of small-diameter SWNTs needs further investigation.

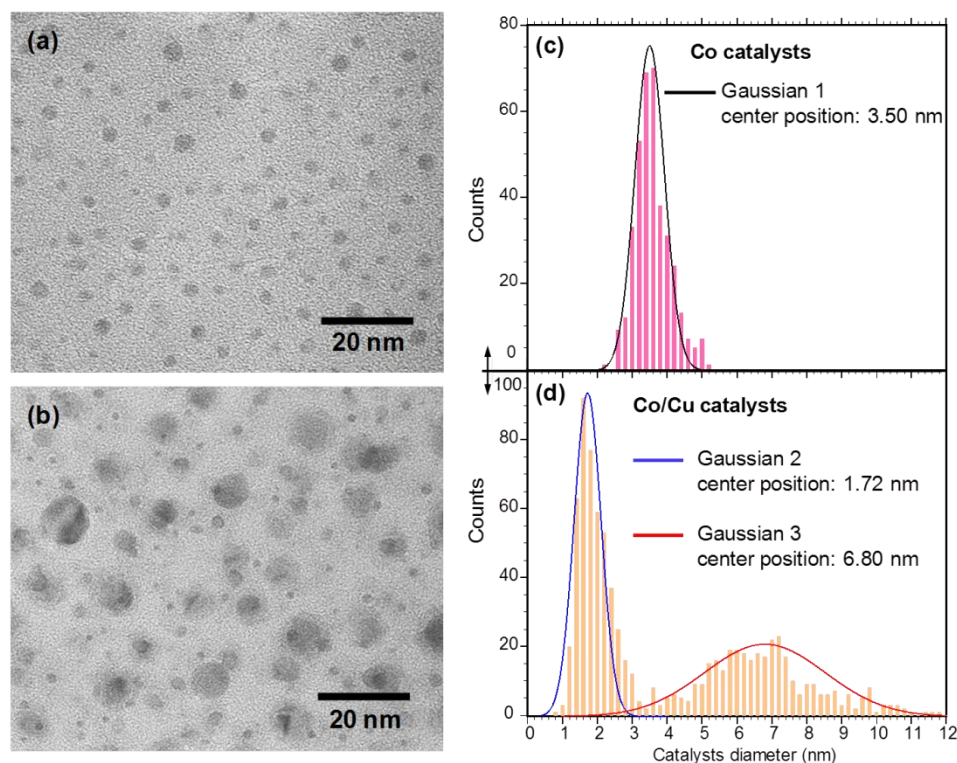


Figure 2.18 TEM imaging of Co and CuCo catalyst and size distribution of the particles. (a) Imaging of sputtered Co particles reduced at 700°C. (b) Imaging of sputtered CuCo particles reduced at 700°C. (c) Size distribution and the fitted corresponding Gaussian curve of sputtered Co particles from (a). (d) Size distribution and the fitted corresponding Gaussian curves of sputtered CuCo particles from (b). Reproduced from [111] with permission from the Royal Society of Chemistry.

To detect the composition of the particles in CuCo catalyst system, elemental mapping of these nanoparticles by energy dispersive X-ray spectroscopy-scanning transmission electron microscopy (EDS-STEM) is shown in figure 2.19. The overlapped elemental distribution of Co and Cu indicates that Co atoms can be either a monometallic Co particle or anchored by Cu atoms in a binary elemental particle. Furthermore, the actual size of the Co aggregates in both binary particles and individual Co clusters is smaller than the size of particles in mono Co metallic catalyst system by the comparison between Figure 2.18a and Figure 2.19a. Note that the Co nanoparticles are not fully encapsulated by Cu atoms but some parts are exposed outside. Moreover, even though Cu can also act as a catalyst in the synthesis of SWNTs [117-119], the low efficiency of Cu catalyst in ACCVD in the previous result (not shown here) and the large diameter of Cu particles suggest that SWNTs in CuCo system may be only

grown from active Co nanoparticles. Thus the smaller Co catalyst particles may be related to the growth of SWNTs with small diameter. Furthermore, CuCo alloy and some other intermetallic compounds are not explicitly discerned in the mapping result possibly due to the ignorable solubility of Cu in Co at this low temperature. However, strong adhesion force between Co and Cu atoms contributes to the conformation of these binary particles in CuCo catalyst system. Owing to the Cu-Co interaction, Co catalyst can be protected from coalescence into larger particles resulting in the small-size Co particles and the small-diameter SWNTs.

On the other hand, high angle annular dark field-scanning transmission electron microscopy (HAADF-STEM) can generate a Z-contrast imaging to show a strong contrast difference with a monotonic dependence on thickness (where Z is the atomic number). The intensity of image contrast is related to the atomic number with a relationship of Z^2 . In this bimetallic CuCo catalyst system, the atomic number of Co ($Z=27$) and Cu ($Z=29$) is similar, thus the difference of contrast is dependent on the thickness, that is the size of the spherical particles. Moreover, as shown in Figure 2.19d, the atomic number of Co and Cu is about twice of O ($Z=16$), thus the metallic nanoparticles (arrow A) are brighter than the oxidized ones (arrow B) compared with the same size particles. By combining the elemental mapping in Figure 2.19c with Figure 2.19e, the Co particles anchored by Cu are brighter than the oxidized mono Co particles which means the disengaged Co particles exist as oxide but the binary CuCo particles can be metallic. In the high resolution HAADF-STEM image combined with elemental mapping in Figure 2.19f, the lattice structure can be assigned to the (111) and (200) of face-centered cubic (FCC) Cu consistent with the interplanar spacing of 0.21 nm and 0.18 nm (JCPDS-International Centre for Diffraction Data 2004, card no. PDF#65-9026). Note that the lattice structure of Cu part is an identical phase of single-crystalline Cu and the grain boundary because of the additional adherence of Co atoms reveals a perfect structure matching and anchoring effect between Cu and Co. The strong adherence due to Cu on Co particles results in a redistribution of Co particles on the substrate which splits into small Co particles and anchored Co particles by large Cu particles. The

diameter of SWNTs does not solely depend on the size of catalyst, however, since the possibility of intermetallic compounds and alloys in the CuCo bimetallic system is excluded, the size reduction of Co particles is mainly responsible for the growth of small-diameter SWNTs compared to the large mono Co catalyst at the same growth condition [120,121]. Therefore, the positive correlation between the catalyst size and the SWNT diameter could be validated in CuCo bimetallic system. The anchoring effect of Cu discovered here provides a new strategy to independently control the catalyst size for the direct growth of small-diameter SWNTs for the future wide band gap semiconductors.

In view of the STEM results, a growth mechanism for the synthesis of the high-quality and small-diameter SWNTs is proposed as shown in figure 2.20. In the control experiment of Co monometallic catalyst system, Co particles have a certain degree of mobility on substrates because of the weak Co–SiO₂ bonding strength at the growth temperature. The migration of Co either by the diffusion of single Co atoms or in terms of colliding and coalescing of whole Co nanoparticles would result in the formation of large-size Co nanoparticles, as shown in Figure 2.20a. As far as the CuCo bimetallic catalyst system is concerned, Cu nanoparticles are highly mobile at the growth temperature due to the low melting point of Cu which will easily form many large particles through Ostwald ripening or Smoluchowski ripening [122]. The resultant larger Cu nanoparticles can be relatively more stable on the substrate because of the enhanced contact area. The fixed Cu nanoparticles can easily capture Co nanoparticles, resulting from the strong adhesion between Co and Cu. The anchored Co nanoparticles are protected by the Cu nanoparticles from growing into much larger ones, as illustrated in Figure 2.20b. The much smaller Co nanoparticles in the CuCo bimetallic catalyst system are the dominant reason for the direct synthesis of small-diameter SWNTs.

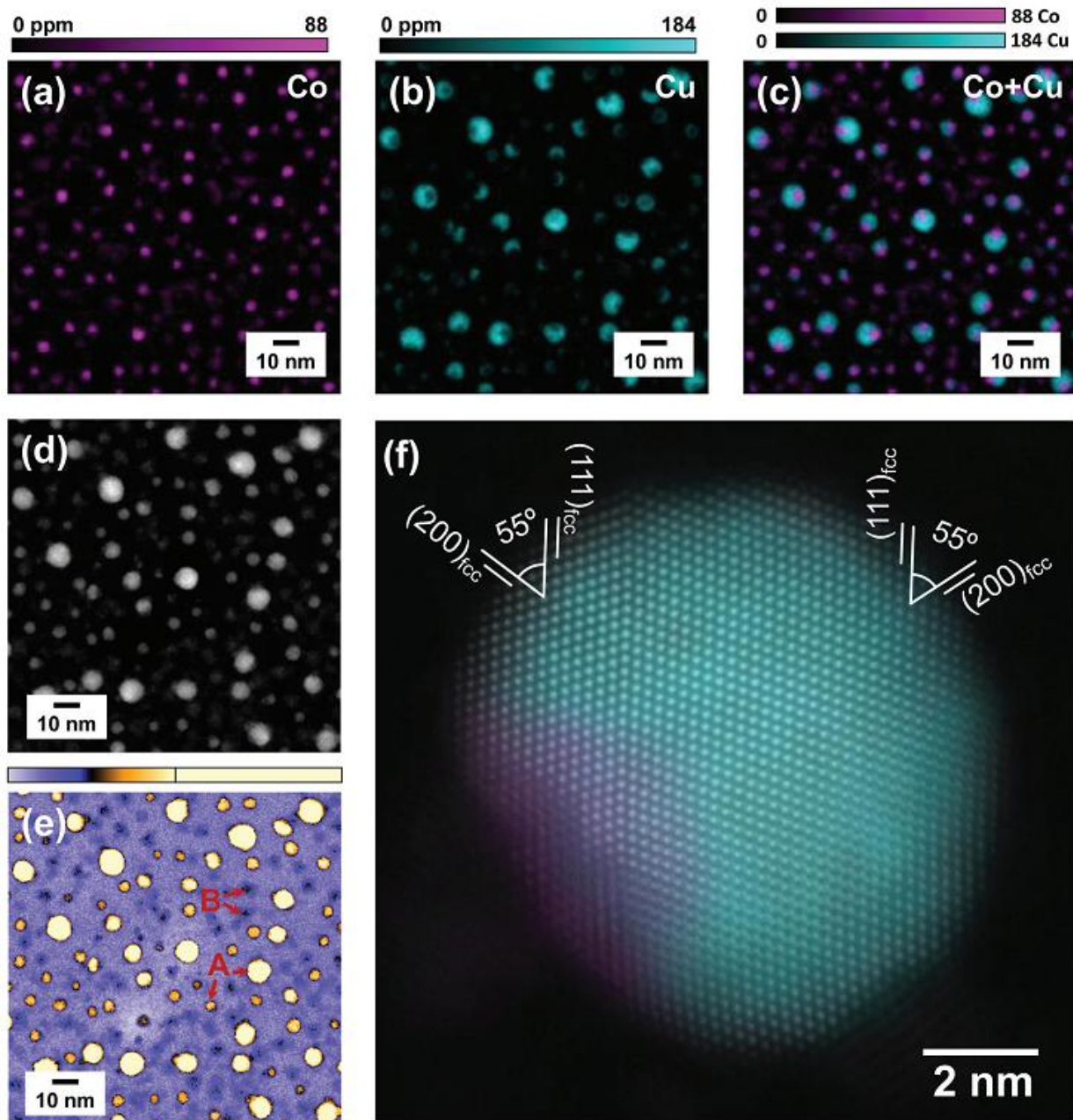


Figure 2.19 EDS mapping showing the elemental distribution of Co (a) and Cu (b) on the Si/SiO₂ micrgrid reduced at 700°C. (c) The overlapped elemental distribution of Co and Cu showing the detailed attachment between Co and Cu. (d) HAADF-STEM imaging of the CoCu catalyst with (e) highlight intensity distribution using colour bar. The imaging was taken in the same area as shown in (a–c). (f) EDS-STEM mapping of Co & Cu overlapped on high-resolution HAADF-STEM showing the structure of one typical binary catalyst particle. Reproduced from [111] with permission from the Royal Society of Chemistry.

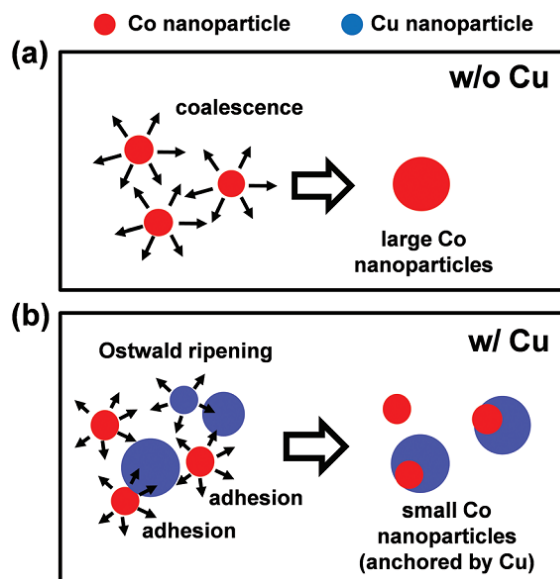


Figure 2.20 Possible mechanism showing CuCo catalyst (b) can grow small-diameter SWNTs compared with the pure Co catalyst system (a). Reproduced from [111] with permission from the Royal Society of Chemistry.

2.4 Summary

In this chapter, detailed experimental methods used in this dissertation are introduced with the physical principles and typical illustrations. Catalysts are prepared by dip-coating or magnetron sputtering. Dip-coating is a conventional method in our lab which is quite simple and can be used for most of catalysts for SWNT growth by changing the metal precursors and the corresponding solvent. Annealing is necessary after the dip-coating to transform the metal salt to metal oxide [123]. Magnetron sputtering is widely used in industry and in this case we choose sputtering because of the uniformity of the deposition and the high-melting point of W makes sputtering more practical than vacuum evaporation. The diameter and chirality distribution of as-grown SWNTs can be characterized by the optical method including Raman and absorption spectroscopy. TEM observation of catalyst structure by the in-plane method is a reliable way for the detailed mechanism study in the field of SWNTs which may pave a possible way for the future chirality control synthesis and industrial applications in electronic devices.

Chapter 3 Selective synthesis of (12, 6) with sputtered W-Co

The excellent properties of SWNTs make them one of the most promising materials for the applications in electronic devices. Their different applications strongly rely on the structure-dependent properties of SWNTs [124]. And the variety of chiralities of SWNTs provides versatile possibilities in real applications and can widen the performance of devices in a broad range with really small differences since the band gap of SWNTs can range from ~ 0.5 eV to ~ 2 eV with really tiny atomic differences [125]. However, the mixture of various chiralities in as-grown samples degrades their advantages which in turn impedes the development of SWNTs-based devices. That is because the nanodevices with homogenous structure can show excellent performance, however, most of the as-grown samples are mixtures with many chiralities including both metallic and semiconducting SWNTs. It is still very challenging to grow SWNTs with single chirality.

This chapter will mainly focus on the selective growth of SWNTs with sputtered bimetallic W-Co catalyst. The state of art will tell us how the selective growth is going on recently for the future large-scale applications. A more simple method to prepare bimetallic W-Co catalyst to selectively grow (12, 6) will be discussed in detail. Different strategies for better selectivity and parametric study have been done with this catalyst. In-plane TEM on the Si/SiO₂ microgrid will be further investigated to disclose the complicated structure evolution at high temperature and detailed mechanism will be discussed.

3.1 State of art to achieve single chirality of SWNTs

In order to realize the large-scale industrial applications of SWNTs, it is essential to control

the chirality, electronic structure, shape, position, orientation from micro-dimension to macro-dimension of the SWNTs assemblies. The most important part for fundamental researches and potential applications is the structure control of the as-synthesized SWNTs. Researchers have made great efforts from different strategies to achieve pure chirality and electronic structure of SWNTs which mainly fall into two categories: one is the postsynthesis separation, the other one is the direct selective growth.

3.1.1 Separation of SWNTs

Separation of SWNT mixtures to obtain single-chirality SWNTs has achieved considerable progresses based on their different chirality-determined properties. Chemical and physical methods such as dielectrophoresis [125] and density gradient centrifugation [126], electrophoresis [127], covalent and noncovalent surface functionalization [128, 129] have been widely investigated for the large-scale separation towards semiconducting pure or chirality pure SWNTs. High-purity separated (6, 5) SWNTs have been reported [130]. Semiconducting SWNT film with purity over 99% has been fabricated with the separated SWNTs [131]. Super-aligned SWNT film has been obtained with slow vacuum filtration method which is also applicable for the separated single-chirality SWNT dispersions [132].

3.1.2 Selective synthesis of SWNTs

Even though the postgrowth separation provides chirality-purified SWNTs for further applications, the drawbacks of this strategy also limit its large-scale applications, such as the shortening of the tubes, defects induced from ultrasonication and the residues of surfactants in the dispersions. Furthermore, the morphology of the obtained films is always strongly dependent on the post assembling process, which may deteriorate the performance of the electronics [133]. Thus the selective growth of SWNTs with pure chirality or electrical property is more urgent and garners considerable interests among researchers. Since the (n,m) index families include one third metallic SWNTs and two thirds semiconducting SWNTs, if all of SWNTs have the same possibility to grow in one sample, each as-grown SWNT sample

should have 66% semiconducting SWNTs which is far from requirements for applications. The growth of SW NTs strongly depends on the growth conditions (temperatures, carbon feeding components and velocity, pressure et al.) [54, 134, 135], catalyst compositions (mono, binary or even ternary, ratio) [136-138], catalyst size distribution [139], and structure [140], properties of support materials [141] and other parameters that possibly impact the nucleation and growth of SWNTs thus leading to different chirality distributions. Researchers have made significant efforts to explore possible approaches towards structure selective growth from both experimental and theoretical aspects. For example, Y. Miyauchi et al. obtained a chirality enrichment of (6, 5) and (7, 5) SWNTs with a low temperature alcohol catalytic CVD [142]. J. Liu et al. claimed the synthesis of semiconducting SWNTs by using an ethanol/methanol mixture or by water etching [143-145]. J. Zhang et al. found that metallic SWNTs can be destroyed by using UV light during the growth [146]. A. R. Harutyunyan et al. reported a direct synthesis of metallic SWNTs as high as 91% by modulating the ambient gas during annealing [147]. Y. Chen et al. achieved selective synthesis of (9, 8) with 33.5% abundance among all species [148-150]. B. Yakobson et al. demonstrated that near armchair SWNTs were kinetically favorable during growth, which resulted in a greater length and abundance [151]. This model was later supported by B. Maruyama et al. through an in situ Raman experiment [152]. More recently, they concurrently considered kinetic and thermodynamic aspects of CNT growth and explained the different enrichments under different CVD conditions [153].

3.1.3 Catalysts in the selective growth of SWNTs

Within various parameters, catalyst plays a significant role in the chirality definition during the SWNT growth process. Results have shown the observations of catalyst particles on the end of single-walled carbon nanotube which indicate the connection between nanoparticles and the SWNTs [154-157]. The difficulties of chirality control lay mainly on the catalyst evolution at high growth temperature due to thermal coalescing or Ostwald ripening resulting in large diameter of catalyst particles and broad chirality distribution of SWNTs. Efforts are

devoted to the size-control of catalyst nanoparticles and the exploration of new catalysts. A chiral-selective growth of SWNTs was realized with a preselection of catalyst size and an energy-dependent nucleation by using a simple monometallic Co catalyst [158]. Different from normal transitional metal catalysts which can grow SWNTs with broad chirality distributions, Rh has been reported to narrow down the chirality distribution of SWNTs through a perpendicular nucleation mode [159]. Solid Mo_2C particles have been claimed to catalyze small-diameter SWNTs with narrow chirality distribution at low carbon feeding rate in hydrogen-free environment [160]. An important strategy for the selective growth of SWNTs is the bimetallic catalysts which usually possess different catalytic properties than either of their parent metals and thus they have been widely explored in catalytic reactions for SWNT growth. Adding metals of high-melting point to transitional catalysts can significantly prevent nanoparticles from agglomerating and stabilize catalyst and grow SWNTs with narrow chirality distribution. D. E. Resasco et al. reported a supported CoMo catalyzed synthesis of (6, 5) dominant SWNTs by tailoring growth conditions and supported materials [134]. A possible mechanism was proposed to account for the well dispersed nano CoMo particles during calcination in the growth of SWNTs [123]. Platinum-group metals are also combined with transitional metals by several groups to selectively grow SWNTs dominant by (6, 5) [161-163]. Another interesting direction is the combination of transitional metals with Cu (low melting point metal) that can selectively grow semiconducting SWNTs with small diameter at low temperatures [111, 113-115], offering potential applications in nanodevices.

3.1.4 Recent breakthroughs of high selectivity with W-based catalyst

With respect to the catalyst on the chirality-selective synthesis of SWNTs, one breakthrough is that in 2014, Professor Li's group from Peking University successfully reported high selectivity, 92% of (12, 6) by using a tungsten-based bimetallic catalyst clusters via a high-temperature reduction and growth process [164]. According to their explanation, the Co_7W_6 alloy is the real catalyst with different facets match with different chiralities through varying the growth conditions. Simulations show the (0 0 12) and (1 1 6) plane can

structurally match with (12, 6) and (16, 0) SWNTs and they have achieved selectivity of (12, 6) with 92% and (16, 0) with about 80% experimentally [165]. And more recently, they obtained the selectivity towards (14, 4) with water assisted reduction process [166]. However, with a liquid phase of preparation method of catalyst, the yield and selectivity strongly rely on the surface property of the substrate and their samples are normally not uniform with low yield even with a hydrophilic treatment of substrate. Even though they contributed the selectivity of SWNTs to the structure matching with specific facet of Co_7W_6 alloy by density functional theory (DFT) calculations, many other questions in the growth mechanism is still not addressed-for example the detailed diffusion process of carbon in the Co_7W_6 alloy and the elongation mechanism of carbon tubes. Thus a uniform and large-scale method is much more urgent for the chirality controlled growth and a more detailed study to unravel the veil of underlying mechanism is highly desired.

3.2 Selective growth of (12, 6) with sputtered W-Co

The key to the high selectivity in the Nature paper is attributed to the W-Co clusters, which can produce a Co_7W_6 alloy that structurally matches with (12, 6) SWNTs. The catalyst they used is a unique crown-type structure molecule that contains six Co atoms encapsulated with a W-based polyoxoanion shell, which favors the formation of the Co_7W_6 alloy at high temperature. If this growth selectivity is governed by catalyst structure regardless of the precursor molecules, preparing a catalyst by more versatile optional methods will not only verify the robustness of this W-Co combination, but may also benefit possible scalable production in the future.

3.2.1 Growth of SWNTs with sputtered W-Co as catalyst

A developed simple sputtering method is reported to prepare bimetallic W-Co catalysts for the selective CVD growth in this dissertation. The detailed experimental process is similar to CuCo system. The nominal thickness for tungsten and cobalt is W: Co=0.7 nm: 0.3 nm. The total thickness of active catalyst is normally no more than 1 nm to restrain the growth of

multi-walled carbon nanotubes [167]. In the sputtering process, the p-doped Si substrate with a 300 nm SiO₂ layer is deposited with metallic W and Co in sequence followed by 5 min annealing at 400°C in air. After sputtering, the prepared substrate is placed in the ACCVD chamber. The quartz tube is flushed with a 300 sccm Ar for 5 min and afterwards, the Ar/H₂ (3% H₂) mixture gas is purged during the heating process at the pressure of 40 kPa. The reduction temperature ranging from 600°C to 850°C is kept for 5 min with a subsequent heating or cooling process in Ar gas to the fixed growth temperature of 750°C. After that, the ethanol flow is manipulated at the rate of 150–450 sccm for a 5 min growth with a total pressure of 1.3 kPa. The growth can also be terminated by further controlling the growth time. Finally, the chamber will be cooled down to room temperature with a 300 sccm Ar gas.

3.2.2 Characterization of (12, 6)

In order to precisely characterize the as-grown SWNTs with W-Co and analyze the chirality distribution, various methods are utilized including the scanning electron microscopy (SEM), Raman spectroscopy, optical absorption spectroscopy, transmission electron microscopy (TEM). The SEM images show different morphologies with different conditions. Raman and optical absorption spectrum can represent the optical response of SWNTs in the sample from which we can assign the chirality and analyze the chirality distribution [83]. The TEM can show the morphology of SWNTs and catalyst structure to uncover the structure evolution by changing the growth conditions to further disclose the growth mechanism.

3.2.1.1 SWNT morphology by SEM

Figure 3.1 shows the representative SEM images of SWNTs grown from sputtered W-Co catalyst at a temperature of 750°C. A SWNT sample produced from sputtered Co at the same condition is demonstrated for comparison. Sputtered Co can nucleate with a high density and form a vertically-aligned SWNT forest, while in the case of W-Co bimetallic catalyst system, less SWNTs are grown with a lower density and uniformly distributed on the Si substrate. As illustrated from the high resolution of SEM images in the inset, the SWNTs obtained from

W-Co catalyst usually possess a length of several micrometers after a 5 min growth, which are not much different from those of pure Co. Note that the SWNTs grown from W-Co are likely to be encapsulated with some white particle impurities. These white particles will be characterized with high resolution TEM techniques and discussed later. In this case, the sputtered W-Co catalyst can grow SWNTs uniformly over the entire substrate of which the spatial uniformity is going to be significantly essential for the fabrication of nanodevices.

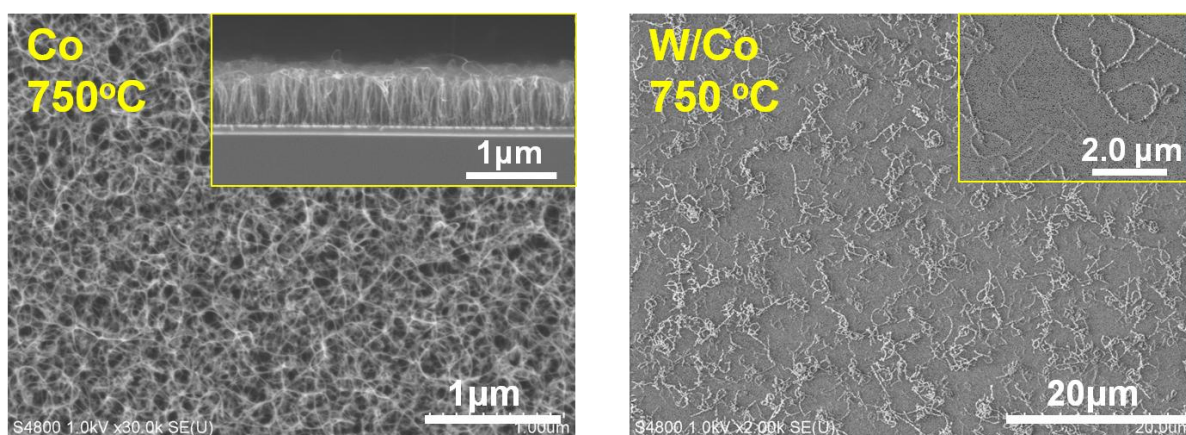


Figure 3.1 SEM images of SWNTs grown from sputtered Co and W-Co. Insets are the cross-section image showing the vertical alignment of SWNTs and high magnification image respectively.

3.2.1.2 Assignment of the chiralities of as-grown SWNTs

The existence and chirality distribution of SWNTs are firstly characterized by Raman spectroscopy. As shown in Figure 3.2, clear differences are observed in RBM region between the sputtered Co and W-Co catalyst systems. For pure Co catalyst, the RBM peaks excited at four different lasers display a very broad chirality distribution, while in the case of W-Co bimetallic catalyst system, a dominant peak located at 197 cm^{-1} is resonant at 633 nm accompanied by some sparse peaks from other chiralities.

In order to assign the chiral indices of the dominant RBM peak at 197 cm^{-1} by combination with the diameter and excitation transition energy according to Kataura plot, a relationship of the diameter of SWNTs and their corresponding RBM peaks is determined by $\omega_{\text{RBM}} =$

$235.9/d_t + 5.5$. This relation is carefully calibrated based on the investigation of the interaction from substrate, amorphous coating and catalyst which suits for the SWNTs on flat Si/SiO₂ substrates in the range of 1.2-2.1 nm [168]. The zoomed Kataura plot extracted from this relation with the frequency from 180 cm⁻¹ to 200cm⁻¹ is shown in Figure 3.3. The only possible alternates are (12, 6) and (9, 9). Due to the asymmetric G⁻ band shape with a Breit–Wigner–Fano (BWF) feature shown in Figure 3.4 [169], the index of the dominant peak is assigned to (12, 6).

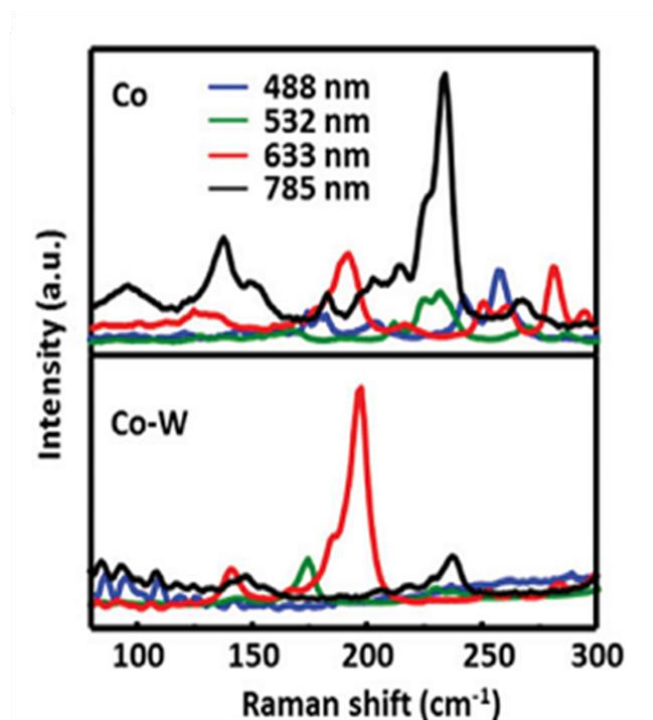


Figure 3.2 Raman spectra of SWNTs grown from sputtered Co and W-Co with four different lasers (488 nm, 532 nm, 633 nm, 785 nm). Reproduced from [170] with permission from the Royal Society of Chemistry.

In order to check the quality of the as-grown SWNTs, high-frequency Raman spectrum is a good tactic. As shown in Figure 3.4, the G-bands of both samples (grown from Co and W-Co catalyst) show typical features of SWNTs, with a clear split into G⁺ and G⁻ band. The D bands of both samples are not strong, and typical I_G/I_D ratios are about 15 to 20. This indicates the high crystallinity of SWNTs which is much better than that grown from W-Co clusters perhaps due to the production of other carbon species at that high temperature.

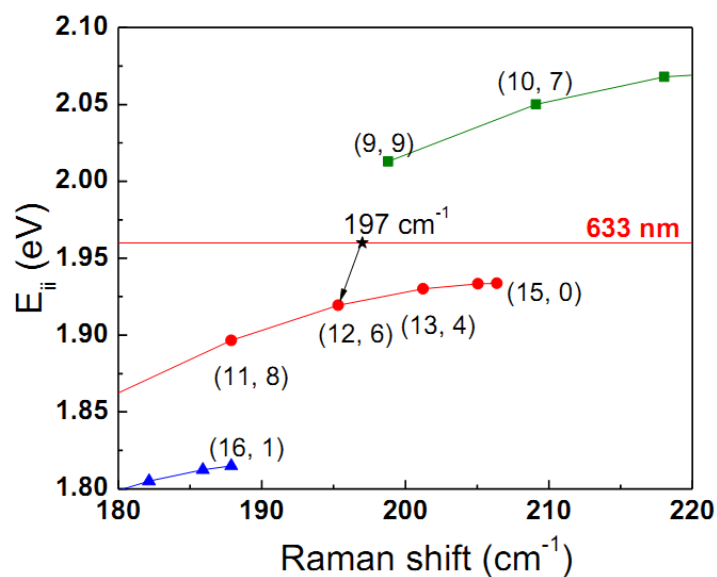


Figure 3.3 Assignment of SWNTs at 197 cm^{-1} according to the Kataura plot. A relation of RBM frequency and diameter of $\omega_{\text{RBM}} = 235.9/d_t + 5.5$ is utilized [168]. The red horizontal line corresponds to the excitation energy of 633 nm laser. Reproduced from [170] with permission from the Royal Society of Chemistry.

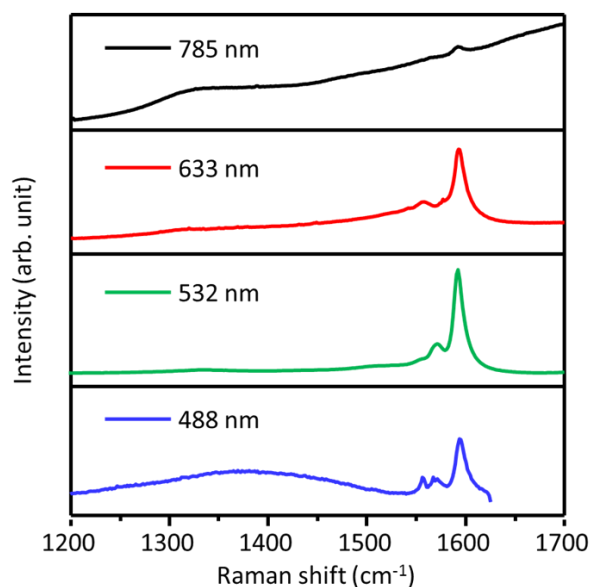


Figure 3.4 Characteristic Raman spectra (G-band region) of SWNTs grown from sputtered W-Co. The catalyst reduction and CVD reaction were performed at 750°C . Reproduced from [170] with permission from the Royal Society of Chemistry.

3.2.1.3 Assessment of the content of (12, 6) in the as-grown SWNTs

Owing to the resonant effect, the Raman intensity cannot quantitatively tell us the enrichment

of (12, 6) over all the existing chiralities. One approach roughly shows the chirality distribution is the Raman mapping by counting the frequency of occurrence of RBM peaks which is also reported in the Nature paper. Thus in this case, Raman mapping is carried out to quantitatively estimate the content of (12, 6) and the detailed chirality distribution of the as-grown SWNTs. In the Raman mapping process, the scanning step is set to be 8 μm which is rational to measure each SWNT only once and avoid the overcounting of SWNTs since the spot size of the lasers is smaller than 2 μm and the length of SWNT is no more than 5 μm as shown in SEM images (although there are still such possibilities with more than one SWNTs in each scanning spot). With this method, a 1 cm \times 1 cm sample is characterized by four different excitation lasers (totally 1826 points), and 1157 RBM peaks are observed. Among all the obtained RBM peaks, 607 of them are assigned to (12, 6). If we suppose one (12, 6) peak is from one individual SWNT, then the (12, 6) SWNTs account for 52.5% among all the detectable chiralities. Table 3.1 exhibits a detailed statistical summary from the Raman mapping result. According to the SEM images, it is also very likely that some 197 cm^{-1} peaks come from more than one (12, 6) tubes. In this way, the precise abundance of (12, 6) SWNTs will become higher. The original Nature paper claimed an observation of about seven SWNTs under each laser spot and obtained selectivity as high as 92%. In the SWNT sample grown with sputtered W-Co, the content of (12, 6) can be calibrated to 67%, 75%, 82%, and 89% if we assume there are respectively 2, 3, 4, or 7 SWNTs on average under one laser spot. Since the SWNTs are shown to be sparser and there may be 3 to 4 SWNTs on average under one laser spot, the content of (12, 6) can be over 70% after the calibration with a conservative evaluation. Considering that there may be some other chiralities that are not resonant with all the four lasers and some short SWNTs are not detectable, this value does not precisely reflect the percentage in SWNTs. However, it seems to be conclusive that the as-grown SWNT sample from sputtered W-Co bimetallic catalyst system is highly (12, 6) enriched (Figure 3.5), and the enrichment of (12, 6) is 50–70% from the current Raman analysis.

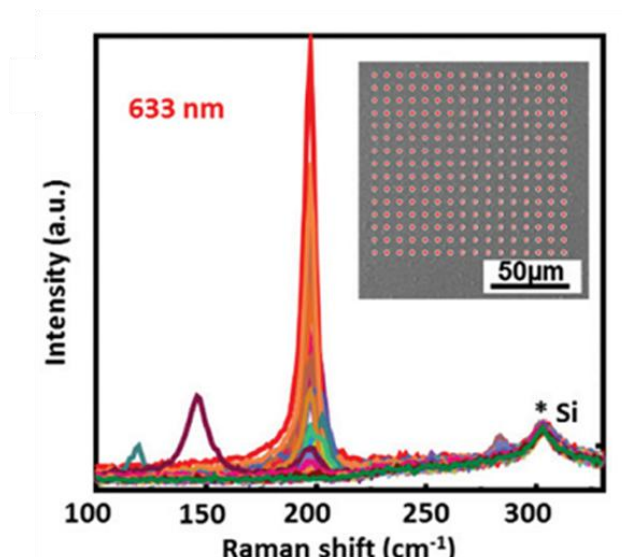


Figure 3.5 Raman spectra of SWNTs with multi data excited at 633 nm. Reproduced from [170] with permission from the Royal Society of Chemistry.

Table 3.1 Statistical analysis on SWNTs of (12, 6) with RBM occurrence frequencies excited by four lasers: 488, 532, 633 and 785 nm.

Excitation laser wavelength	488	532	633	785	total
Number of RBM peaks	21	161	952	23	1157
Number of (12, 6) peaks (195-198 cm ⁻¹)	0	0	607	0	607
Proportion of (12, 6) peaks among all RBM 607/1157=52.5%					

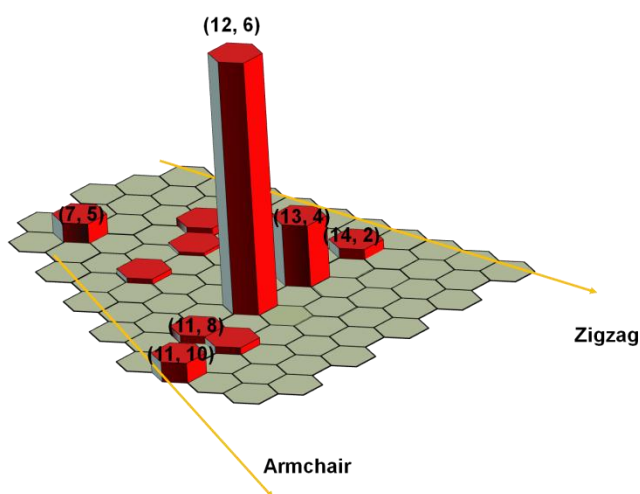


Figure 3.6 Chiral map showing the chirality distribution denoted as the height of column from the Raman mapping.

A more distinct way is shown in Figure 3.6 in which the content of each chirality (occurrence frequency is more than 1%) is represented by the height of the hexagonal prisms in the chiral map. This chiral map shows the abundance of other chiralities besides (12, 6) such as the (14, 2), (7, 5), (11, 8) etc. More interestingly, the high content of the $2n+m=30$ family indicates the conducive nucleation and growth of a specific family.

Except for Raman spectrum, optical absorption usually gives more reliable evaluations of the entire sample in the field of CNTs. Optical absorption is obtained on the dispersed samples by using a UV-vis-NIR optical spectrometer (Shimadzu UV-3150). Since the SWNT yield on the surface is not high enough, 30 pieces of $1\text{ cm} \times 1\text{ cm}$ randomly collected samples are sonicated in D_2O solution with 1.25 w/v% SDS to obtain sufficient optical density. Ultrasonication is not necessary since the bath sonication is enough to tear off the SWNTs from the Si/SiO₂ substrate, and the explicit contrast before and after sonication is shown in Figure 3.7. A dominant absorption peak is located at $\sim 610\text{ nm}$ as shown in Figure 3.8, which is consistent with the M_{11} transition of (12, 6) SWNTs. However, due to the low SWNT yield, the peak is not satisfactorily strong, though over 30 samples were used to prepare one solution. Also, the broad peak suggests the possible coexistence of impurities and other chiralities. Possibly because of these two reasons; we cannot observe a peak splitting that was clearly shown for spectroscopically pure semimetal SWNTs [171, 172]. Compared with the original report of over 90%, this relatively low selectivity could be related to the lower growth temperature and/or to a different catalyst preparation method. Except for this, it is convincing to us that the incorporation of W into a Co catalyst leads to a clear shift and narrowing down of the chirality distribution.

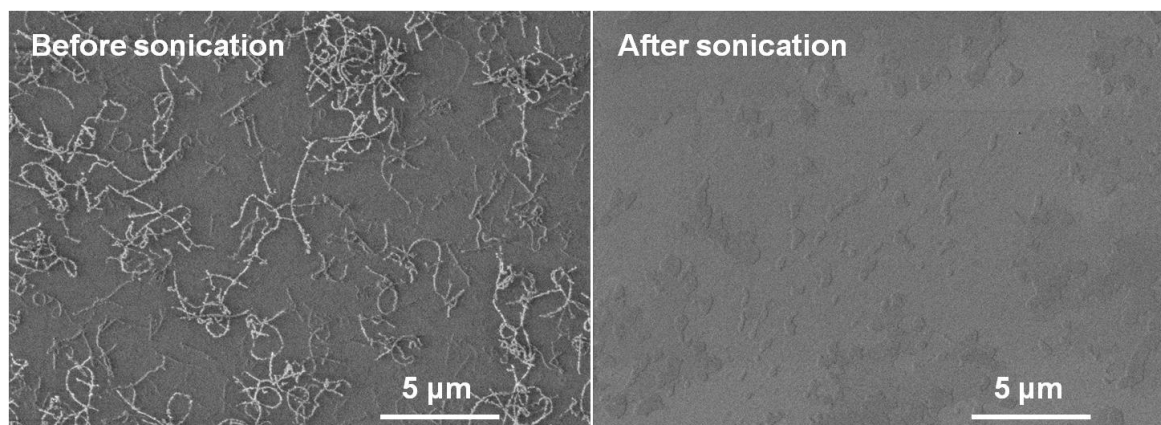


Figure 3.7 SEM images for SWNTs on Si/SiO₂ substrates before and after sonication to disperse SWNTs.

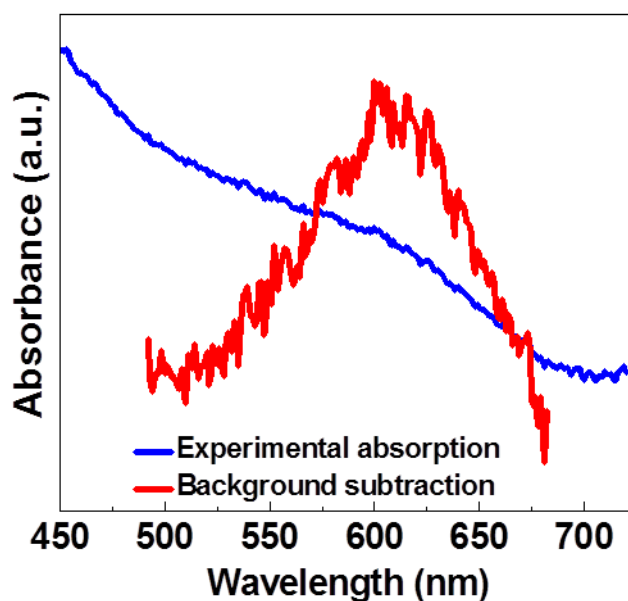


Figure 3.8 Optical absorption spectrum of SWNTs synthesized from sputtered W-Co. Reproduced from [170] with permission from the Royal Society of Chemistry.

3.3 Parametric study of the selective growth of SWNTs with sputtered W-Co

Previous studies have shown that the CVD conditions are essential to the evolution of catalyst structure and the chirality and distribution of obtained SWNTs [173]. In this case, a detailed

parametric study on the influence of CVD conditions on the selectivity and catalysts is going to be discussed.

3.3.1 Influence of the ratio of W to Co

The ratio of two component metals is an important parameter for the structure of the catalyst and the as-grown SWNTs in the bimetallic catalyst system. In fact, with detailed study on the ratio of W to Co, we find that the selectivity indeed relies on the ratio and absolute amount of W and Co in this sputtered bimetallic catalyst system. As shown in Figure 3.9, by decreasing the amount of tungsten with a constant Co volume, the density of SWNTs increases significantly and the lower ratio of tungsten, the closer to the morphology of SWNTs from pure Co, which means the worsening of the selectivity.

On the other hand, the changes of the amount of Co can also vary the yield of SWNTs as shown in Figure 3.10. Increasing or decreasing the amount of Co reveal similar tendency of the yield as W.

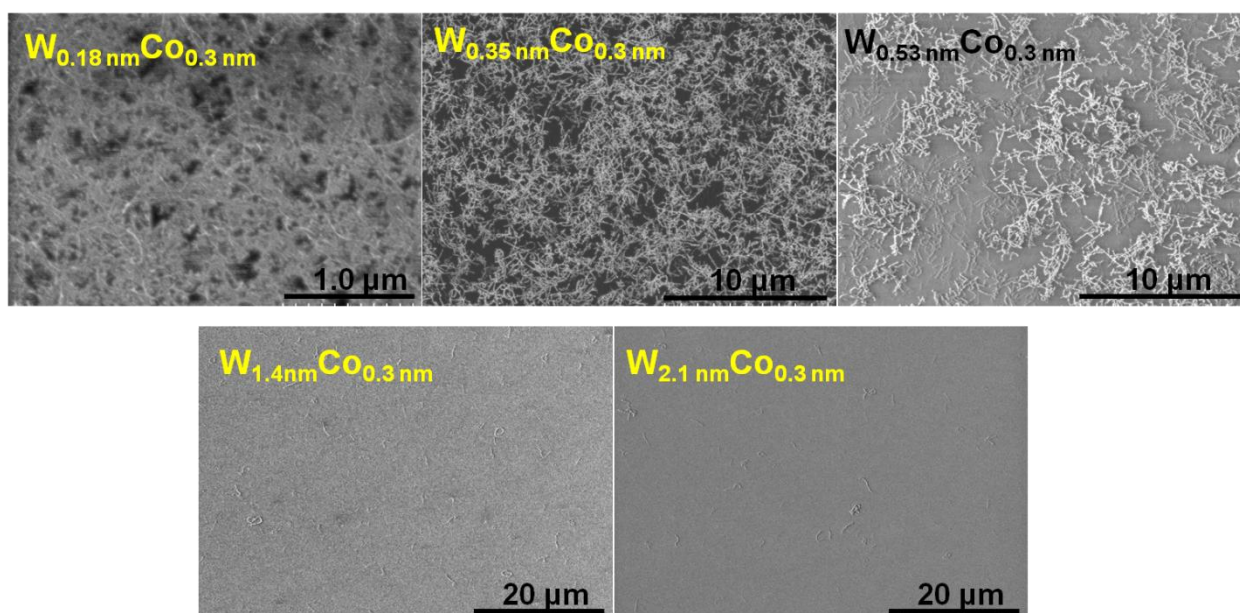


Figure 3.9 SEM images of SWNTs grown with various nominal thickness of W.

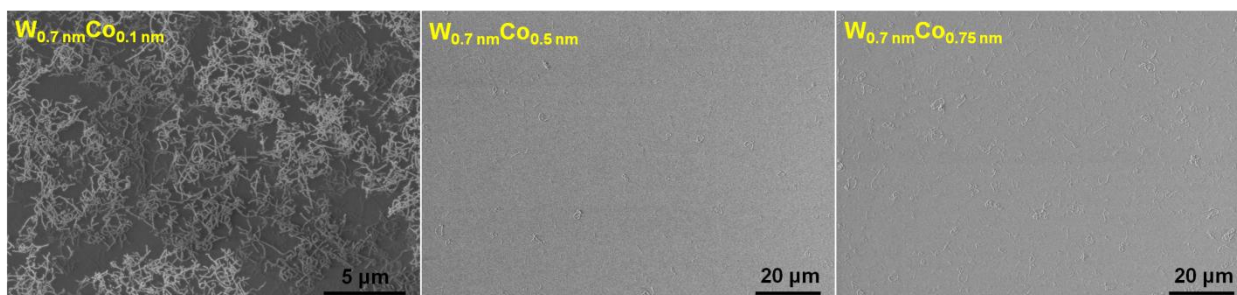


Figure 3.10 SEM images of SWNTs grown with various nominal thickness of Co.

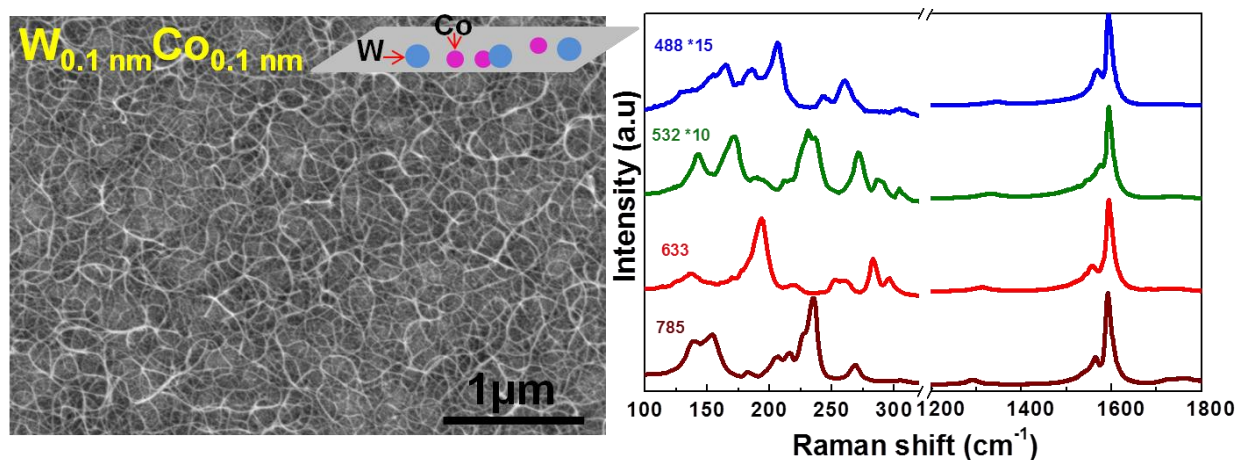


Figure 3.11 SEM images and Raman spectrum of SWNTs grown from $W_{0.1 \text{ nm}}Co_{0.1 \text{ nm}}$. The insert is the schematic showing the relative relation of the Co and W atoms of which the weak interaction between W and Co atoms possibly results in the low selectivity.

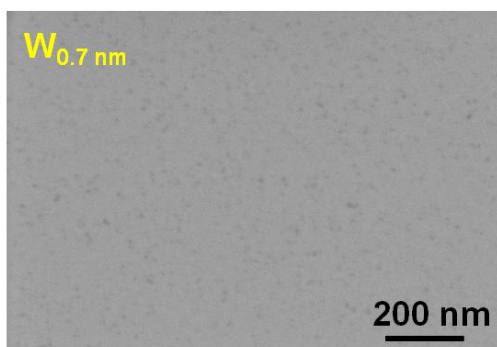


Figure 3.12 SEM image showing no SWNTs are grown from sputtered W.

In order to further check the interaction effect between tungsten and cobalt, much lower amount of W-Co with a nominal thickness of 0.1 nm for both metals is prepared and conducted the growth by ACCVD. The SEM image in Figure 3.11 demonstrates a similar

morphology of SWNTs with that from pure Co. Furthermore, the Raman spectrum also shows similar RBM peaks with broad chirality distribution suggesting the interaction between tungsten and cobalt atoms is very weak leading to the growth of SWNTs mostly from pure Co particles. This means excessive tungsten is necessary to a certain extent to prevent active Co particles from growing SWNTs with broad chirality distribution. Sputtered pure W is also performed with ACCVD to investigate the catalytic property in the growth of SWNTs as shown in Figure 3.12, where no single-walled carbon nanotubes can be grown. This verifies that the Co-related structure is mainly responsible for the growth of SWNTs in the bimetallic W-Co system.

3.3.2 Effect of reduction temperature

Another important factor is the reduction temperature as shown in the Nature paper, because the reduction before the introduction of ethanol predefines the structure of the catalysts which will significantly affect the structure of SWNTs [164]. We have performed various reduction temperatures ranging from 600°C to as high as 1000°C. A two-step reduction and growth strategy has been conducted where the reduction temperature is varied and the growth temperature is fixed. At the relatively low temperature region, the bottom limit of selectivity window is identified by changing the temperature from 600°C to 750°C. In the following part, three typical reduction temperatures will be discussed in detail.

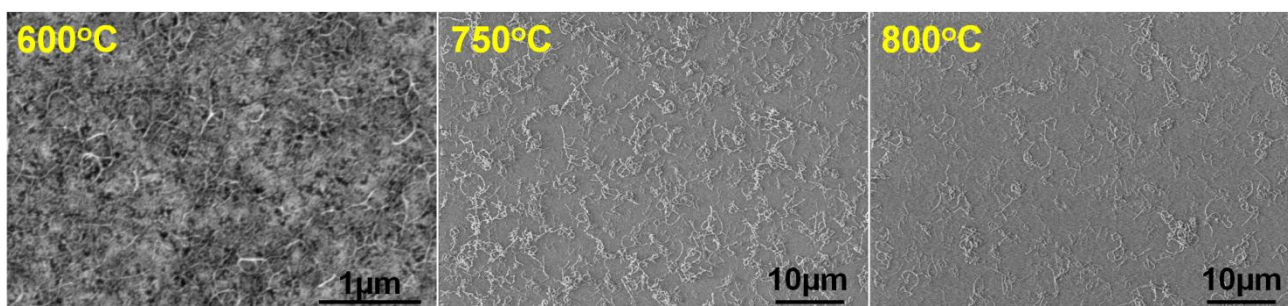


Figure 3.13 SEM images of SWNTs grown at different reduction temperatures. Reproduced from [170] with permission from the Royal Society of Chemistry.

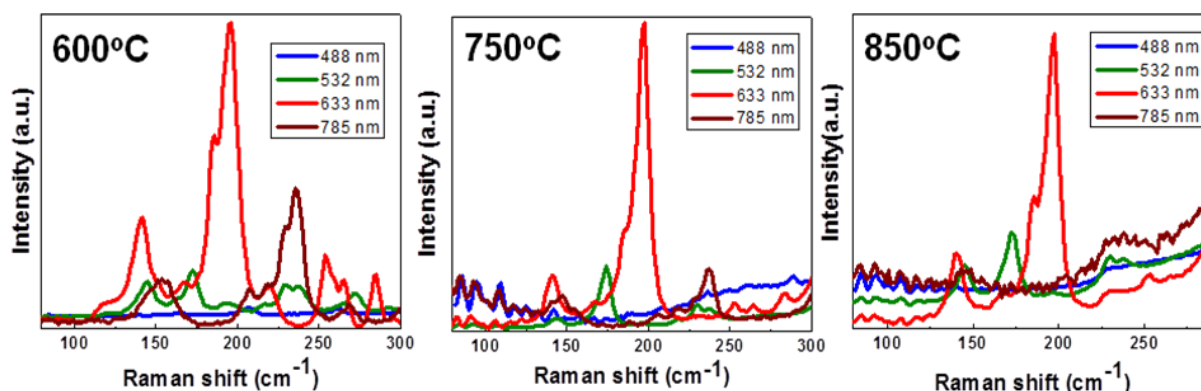


Figure 3.14 Raman spectrum of SWNTs grown at different reduction temperatures. Reproduced from [170] with permission from the Royal Society of Chemistry.

The reduction temperature of the catalyst is found crucial for SWNT yield as well as for the selectivity of (12, 6) SWNTs. Figure 3.13 and 3.14 show SEM images and the corresponding average Raman spectra of SWNTs grown from the W-Co catalyst reduced at three typical temperatures (600°C, 750°C, 850°C). In all three cases, the growth temperature is set the same (750°C) to compare the possible structure change of the W-Co catalyst during reduction. When the reduction temperature is low (600°C), the SWNT yield is much higher than that of the other two samples as illustrated from the SEM images. The Raman spectrum suggests that this low temperature reduced sample is very similar to those grown from pure Co (Figure 3.15). The relative intensity of the 197 cm^{-1} peak (to other peaks) is remarkably decreased. In fact the Raman spectrum for the low-temperature reduced Co is quite similar to 750°C-reduced Co (Figure 3.2). Even though the relative intensity maybe varied due to different reduction temperatures, the chirality distribution is very close to each other where we can regard these kinds of SWNTs as nonselective one in this case. For the samples grown from the higher temperature (750°C) reduced W-Co catalyst, however, the (12, 6) peak significantly dominates the RBM peaks (SWNT yield decreases to 5% roughly estimated from Raman). When the reduction temperature goes up to 850°C, the selectivity slightly improves but the yield becomes much lower. The changes in the relative intensity at the 197 cm^{-1} peak with respect to the total sum intensity are shown in Figure 3.16 revealing a

developing selectivity with the increasing reduction temperature. This trend suggests that despite the reduction at this relatively low temperature, the introduction of W is still effective for the selectivity, which indicates that the catalyst structure may have already changed. Compared to the original report by F. Yang et al., where they claimed that 1030°C is necessary, nearly 300°C lower reduction/growth temperature is puzzling. If not explainable by a further downshift of the bulk phase diagram and therefore the easier formation of the alloy at lower temperatures, there might be some other unidentified factors that are playing a critical role.

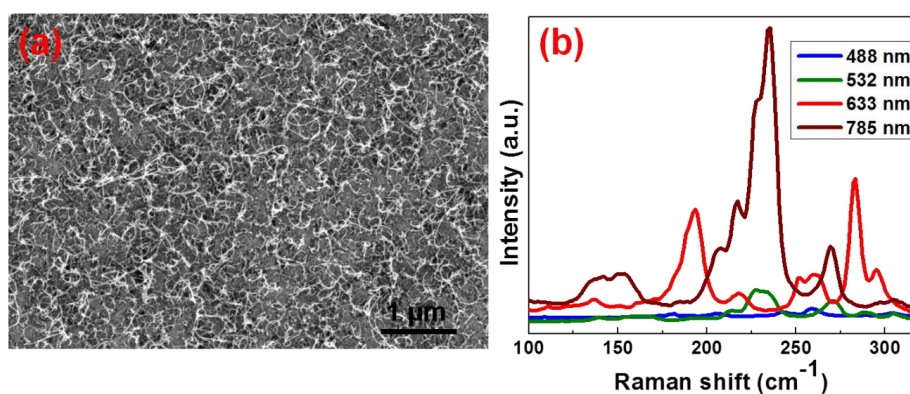


Figure 3.15 SEM image (a) and Raman spectra in RBM region (b) of SWNTs grown from sputtered Co. The catalyst was reduced at 600°C and grown at 750°C.

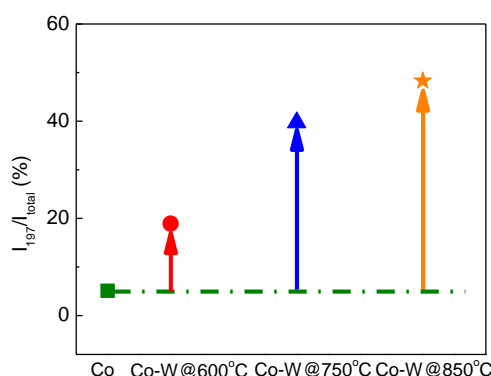


Figure 3.16 Relative intensities of the 197 cm⁻¹ peak with respect to the total sum intensity of RBM peaks changes between different conditions. Reproduced from [170] with permission from the Royal Society of Chemistry.

3.4 Investigation of W-Co catalyst and SWNTs with in-plane TEM

In-plane TEM is performed to tackle this puzzling mechanism on these sputtered W-Co catalysts. In these experiments, the W-Co catalysts are directly prepared onto a SiO₂ microgrid. The advantage of this technique is that this TEM grid can be used for high temperature reactions [111]. Though atomic resolution is not always easy due to the thick SiO₂ background, the most original and realistic catalyst morphology and structure are retained. Furthermore, the in-plane view also provides a chance to access the statistical information of one sample, which is hardly obtainable in conventional TEM observations.

3.4.1 TEM imaging of catalyst morphology

Figure 3.17 shows representative TEM images of samples grown at 750°C but were reduced at different temperatures (similar to samples in Figure 3.13 and 3.14). In Figure 3.17a and b, clear differences in the catalyst morphology are observed between the two samples. At a low reduction temperature (600°C), W and/or Co atoms migrate and form a wormlike/island structure, which may be a transitional morphology from an as-deposited continuous film (not shown) to nano-sized particles. The 750°C reduced catalyst (Figure 3.17b), however, shows a more complex and polycrystal like contrast. Though the melting temperature of W is 3422°C in bulk, it is apparent that W starts to aggregate and form irregular particles at a temperature as low as 750°C. Particularly, the regions near larger W particles seem to have been “swallowed” by the center. Therefore, possibly from this stage, W begins to form an alloy/composite with Co, and those particles with a complex contrast contain both Co and W (structure to be determined later). The 850°C reduced catalysts in Figure 3.17c show a particle-like morphology similar to the 750°C reduced sample, except that the particles are more spherical and the number density is slightly smaller. The simplified illustrations of these changes are shown as the insets of Fig. 3a–c. The in-plane images of these samples after SWNT growth are shown in Figure 3.17d–f. The most noticeable difference is the SWNT

yield, which agrees well with the SEM and Raman observation (Figure 3.13 and 3.14). At the same time, all three samples contain particles with a diameter of 5–30 nm, which are possibly those impurities in SEM observations discussed previously. Besides these three representative samples, we also grew SWNTs from 650°C, 700°C and 800°C reduced W-Co catalysts, which show intermediate morphologies after reduction (Figure 3.18). Three reduction temperatures are shown here to demonstrate a clearer trend from islands to spherical particles. In all these observations, identifying the contrast of SWNTs is very difficult due to the strong background of SiO₂. Few layer graphite sheets are sometimes observed on large particles (possibly excess of W as to be discussed later), but no few- or multi-walled carbon nanotubes exist.

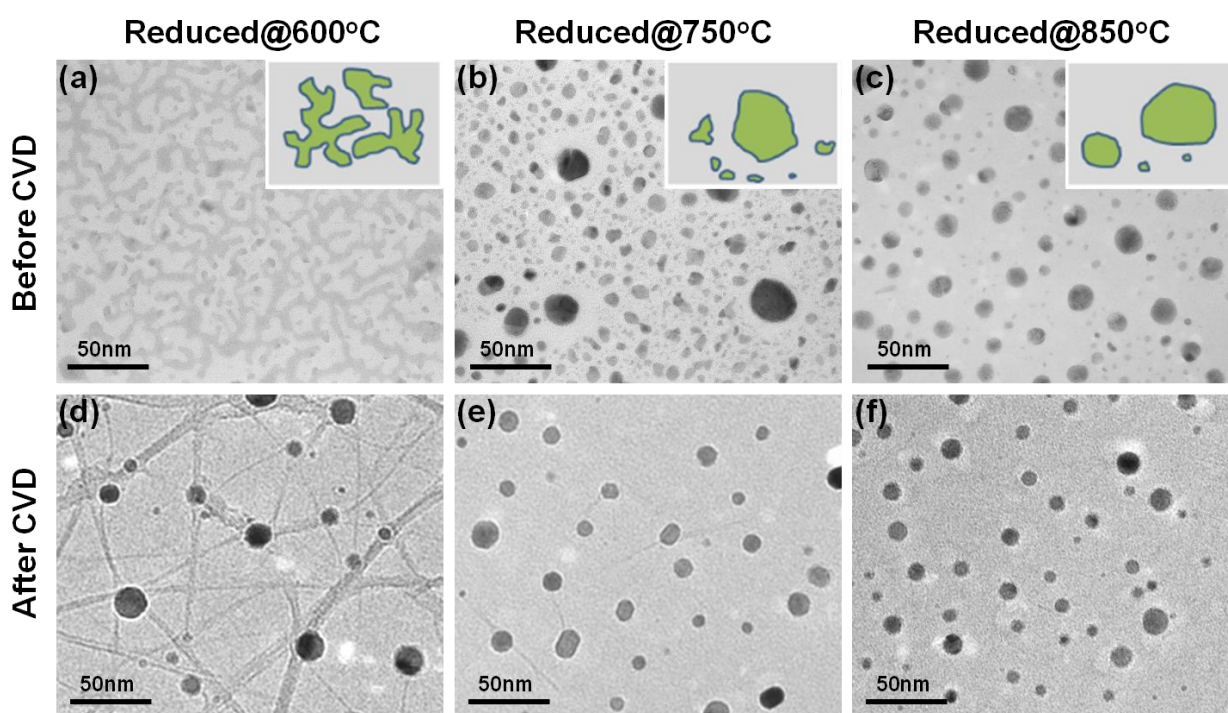


Figure 3.17 TEM micrographs of different temperature reduced (600°C, 750°C and 850°C, respectively) W-Co catalysts. (a), (b), and (c) Before CVD and (d), (e), and (f) after a 5 min growth at 750°C. Reproduced from [170] with permission from the Royal Society of Chemistry.

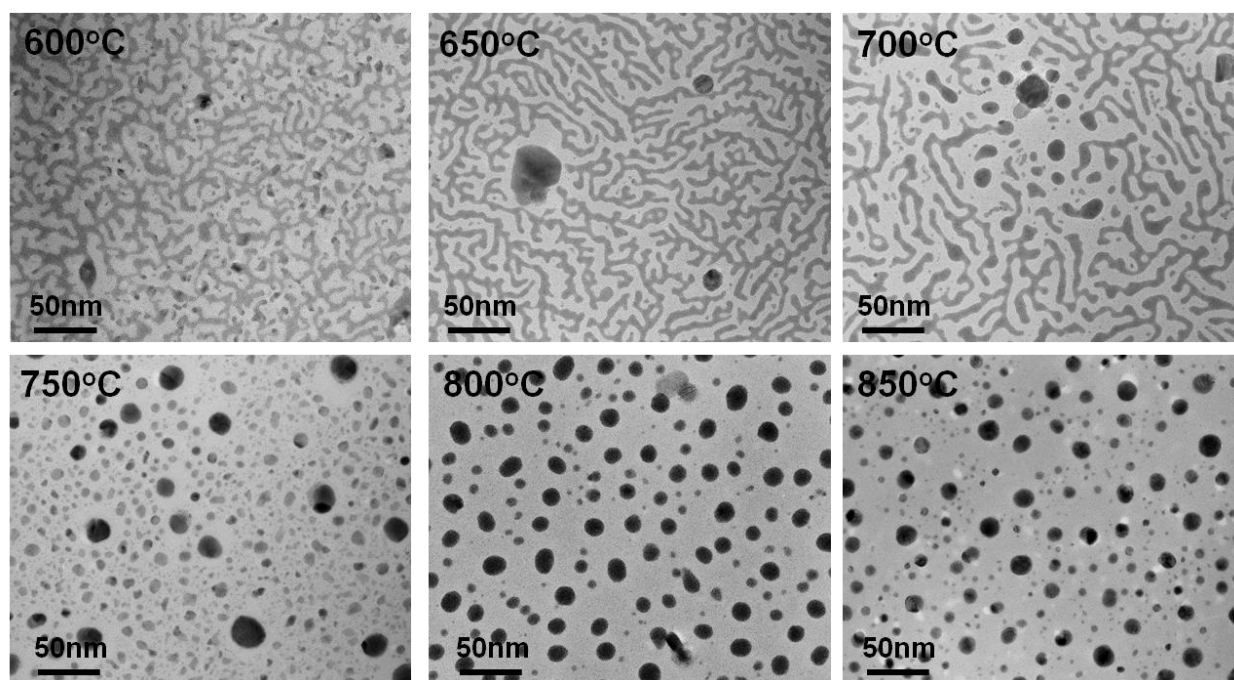


Figure 3.18 Characteristic TEM images of W-Co catalyst reduced at different temperatures (a) 600°C, (b) 650°C, (c) 700°C, (d) 750°C, (e) 800°C, and (f) 850°C, showing the morphology transition from wormlike structure to spherical particles. The strong interaction between Co and W starts from a temperature as low as (c) 700°C. Reproduced from [170] with permission from the Royal Society of Chemistry.

3.4.2 Electron diffraction pattern of the W-Co catalyst particles

The uniqueness of in-plane TEM is its capability of providing comprehensive structural information in a large area. The selected area electron diffraction (SAED) patterns of the samples before and after growth are compared, as shown in Figure 3.19. In this experiment, each diffraction pattern was taken with the selected area aperture diameter of several micrometers, and therefore contains the average information of more than 10 000 particles.

Low-temperature reduced samples show a clear and dominant phase of the BCC structure of metallic W (JCPDS-International Centre for Diffraction Data 2004, card no. PDF#04-0806). Co is not visible possibly due to the lower relative amount, alloying with W and/or oxidized after exposure to air. However, since the obtained SWNTs are very similar to those from pure Co, probably the interaction between Co and W at this lower temperature is less significant and most SWNTs are grown from pure Co. For the high temperature reduced catalysts,

additional diffraction rings appear at around 110 of metallic W (Figure 3.19a), suggesting the formation of a new crystal phase. These diffraction rings match perfectly with $\text{Co}_6\text{W}_6\text{C}$ (card no. PDF#23-0939). Though the as-reduced W-Co catalyst is not supposed to have carbon, this structure is consistently identified in all our experiments where selective growth is achieved. This un-intentionally incorporated carbon (possibly from carbon contaminations and/or residues in CVD apparatus) may contribute to the formation of $\text{Co}_6\text{W}_6\text{C}$. This influence of un-intentionally introduced species is not unique and is also reported previously in an Fe-based system [174].

Since no additional Co related diffraction patterns are observed, it is very likely that this structure is responsible for the nucleation of SWNTs. At this stage, it is not able to rule out the possibility of coexistence of some small amounts of metallic Co particles. However, according to the control experiment described previously, pure Co tends to grow SWNTs with a wide chirality distribution and thus is unlikely dominant in this case. Except this ternary $\text{Co}_6\text{W}_6\text{C}$, no other W-Co alloy phases, e.g. Co_7W_6 , are identified in all our experiments.

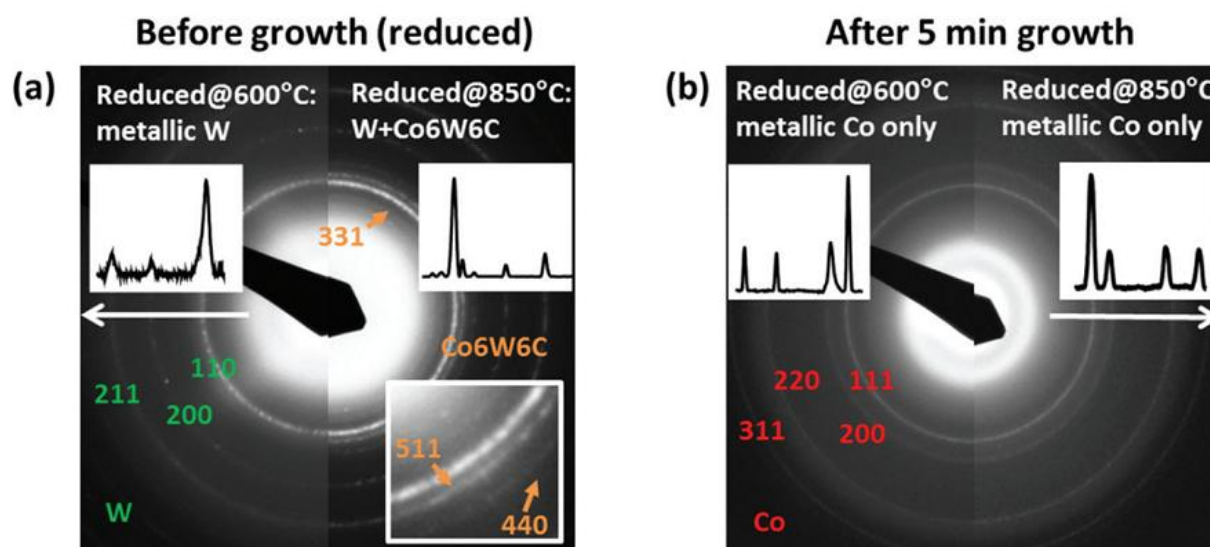


Figure 3.19 Electron diffraction patterns of catalysts reduced at 600°C and 850°C. (a) Before and (b) after CVD growth with the assigned materials and structure. The insets are the relative intensity of electron diffraction rings. Reproduced from [170] with permission from the Royal Society of Chemistry.

Another interesting phenomenon is found that after growth, in both low and high temperature

reduced samples, W related phases disappear almost completely. Neither noticeable metallic W nor any other W related phases remain after a 5 min growth. Only the existence of pure FCC-metallic Co is confirmed by the SAED patterns in Figure 3.19b. The loss of W species is likely due to a reaction with ethanol during the SWNT growth. Ethanol molecules partially decompose into water and ethylene as the main products at the CVD temperature [22]. At the same time, metallic W is reported to be easily oxidized in a water vapor environment to form volatile $\text{WO}_2(\text{OH})_2$, which can easily disappear at high temperatures through the gas phase in the low-pressure CVD system [175].

This dynamic change of the catalyst structure makes it more challenging to identify the active nucleation sites for growth, which suggests that growth time is another important parameter for more precise control over selective growth. Further studies may be focused on CVD time dependent (12, 6) enrichment. Meanwhile, the yield in the present study is extremely low and we are not yet able to increase carbon yield without compensation of selectivity. Also, it is still unclear whether high selectivity and low yield are always strongly coupled (e.g. an earlier work showed no chirality selectivity for W-Co at a higher carbon yield [176]).

Besides growth, more sophisticated characterization may be needed for more precise quantification of SWNTs (e.g. a laser close to 633 nm may excite more SWNT “impurities” that have diameter close to 1.2 nm but are not resonant in current measurement). Nevertheless, we believe that the capability of the W-Co bimetallic catalyst in selective growth is well reproduced and the critical role of W in changing the catalyst structure has been clearly demonstrated. Importantly in this work, the catalyst is prepared by simple sputtering, which is preferable for future larger scale, more uniform synthesis of SWNTs, and hopefully potential applications using chirality specific SWNT samples. This study also brings out more open questions for this complicated system, which definitely needs more efforts from the whole community.

3.5 Summary

In this chapter, a sputtered W-Co bimetallic catalyst is reported to be capable of producing (12, 6) SWNTs with an abundance of 50–70% at milder growth conditions than the previous report. Reduction of the catalysts is crucial for selective growth, which only occurs when the reduction temperature is above 750°C. In-plane TEM reveals clear morphological differences between low-temperature and high-temperature reduced W-Co catalysts. An intermediate structure of $\text{Co}_6\text{W}_6\text{C}$ is unambiguously identified and associated with selective growth of (12, 6) SWNTs. However, the W related structure is also found to be surprisingly unstable in a growth atmosphere after only a few minutes of growth, suggesting that more effort is needed for more precise control of this complex W-Co catalyst for selective growth of SWNTs.

Chapter 4 Structure evolution of W-Co catalyst and the possible mechanism

As discussed in chapter 3, the catalyst structure shows a complicated change from the as-reduced $W+Co_6W_6C$ to Co within 5 min-growth which means the growth time is another important factor that affects the catalyst structure and the selectivity towards (12, 6). In this chapter, a detailed study on the catalyst structural evolution and time-dependent selectivity will be conducted with an ex situ method. An acid treatment has been designed to verify the nonexistence of Co or Co oxide phases in the as-reduced catalyst particles which further validates that the selective synthesis of (12, 6) is related to the Co_6W_6C structure. EDS mapping reveals the elemental distribution of the catalyst particles and a binary structure with W and Co_6W_6C phases. Detailed characterization on the morphology and structure of W-Co catalyst at different growth time demonstrates a complicated evolution from crystallized $W+Co_6W_6C$ and intermediate Co solid solution to the pure Co particles at a 5 min-growth. Based on the study of the bimetallic catalyst, a possible mechanism for the selective growth of (12, 6) with sputtered W-Co has been proposed associated with the detailed structure evolution. The carbide particle selectively offers a nucleation site for (12, 6) cap and the selectivity disappears when all catalyst particles converted to pure Co.

4.1 Detailed characterization of as-reduced catalysts

In chapter 3, we have shown the catalyst particles reduced at 850°C in an Ar/H₂ (3% H₂) atmosphere are a mixture of W and Co_6W_6C phases confirmed by electron diffraction. In order to further check the catalyst composition and the existence of Co phase, an acid

treatment has been developed and the EDS mapping is conducted on the catalyst particles with water-assisted reduction.

4.1.1 Further confirmation of the as-reduced catalysts by acid treatment

The main differences between tungsten and cobalt are not only their melting point but also the solubility in normal acid solution which means their reactivity with hydrogen ion is different. The reduction before growth can give the W and $\text{Co}_6\text{W}_6\text{C}$, and we have not found any Co diffraction pattern after high-temperature reduction. A simple acid treatment experiment is designed to check the as-reduced catalyst compositions on the Si/SiO₂ substrate. The main process is shown in Figure 4.1. Sputtered Co is utilized as a control experiment. The substrate with W-Co catalyst is firstly reduced at 850°C in Ar/H₂ (3% H₂) and cooled to room temperature. The reduced catalyst is then immersed into a 36.5% HCl solution for 30 min, rinsed with water and dried with N₂ gun. The treated substrate is undergone the same growth process with the previous mentioned parameters. The resultant morphology is shown in SEM images in Figure 4.2. The contaminants on left image are displayed to show the focus status. Note that no SWNTs are grown on the acid-treated Co substrate while the treated W-Co catalyst can grow SWNTs in a similar morphology with the non-treated W-Co catalyst. The completely different results indicate a high possibility that only W and $\text{Co}_6\text{W}_6\text{C}$ exist in the as-reduced catalyst otherwise the SWNT morphology grown from acid-treated W-Co catalyst should be much different from the untreated one. Because if metallic Co or oxidized Co is in the as-reduced particles, the acid can remove all of them then the particles in the second-step CVD process is much different from the original reduced particles where Co particles can easily grow many SWNTs resulting in a much higher yield of SWNTs than the acid-treated sample. This interesting result provides a solid clue to the possible selective growth mechanism explained in the following section.

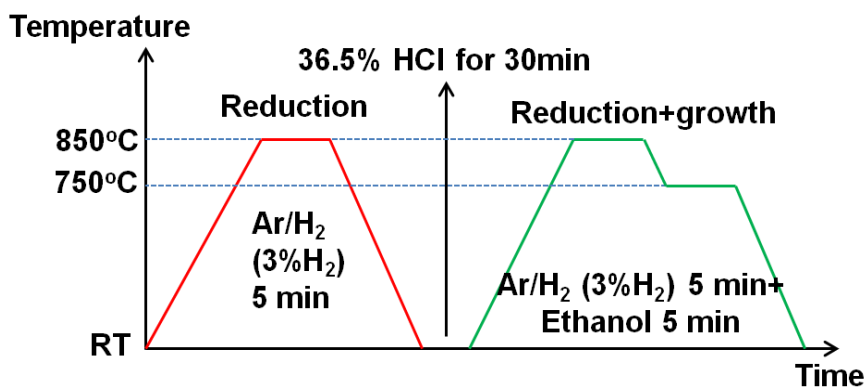


Figure 4.1 Process for the acid treatment and the subsequent CVD growth.

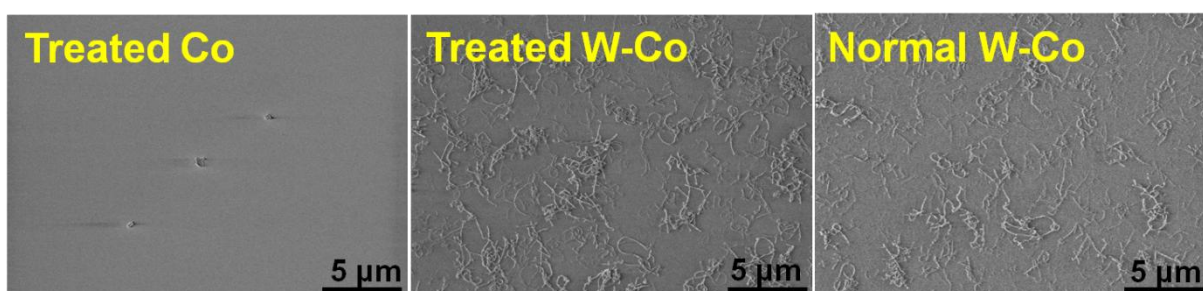


Figure 4.2 SEM images showing the different morphology of SWNT grown after acid treatment.

4.1.2 Elemental distribution of W-Co catalysts

As validated in the CuCo bimetallic system, the in-plane TEM method provides an opportunity to demonstrate the general elemental distribution on a large area of catalysts and the crystal structure of a specific catalyst particle at high resolution for a better understanding of the catalyst composition and structure. Based on this technique, a similar characterization by EDS mapping was performed with sputtered W-Co catalyst. The sample was prepared with a reduction process at 850°C through water-vapor treatment, and the prepared catalyst particles were then observed by in-plane TEM.

A general elemental distribution of W and Co is shown in Figure 4.3. By overlapping the W and Co elements, we can note that there are three kinds of states for W including the free W particles, the $\text{Co}_6\text{W}_6\text{C}$ and the W particles attached to $\text{Co}_6\text{W}_6\text{C}$. In the case of Co, Co only exists in the $\text{Co}_6\text{W}_6\text{C}$ phase which is consistent with the acid-treatment result. The HAADF

image in Figure 4.3d exhibits the image contrast of particles with different sizes. Due to its large atomic number, the W part in the particles reveals a brighter contrast. More interestingly, the extracted spectrum in this mapping area shows a similar atomic ratio of W to Co with the nominal thickness in sputtering suggesting that the control of metal through the nominal amount is reliable. The information in the EDS mapping indicates that the annealed W-Co particles are reduced to W and $\text{Co}_6\text{W}_6\text{C}$. On the other hand, Co can easily form a carbide structure with W atoms and the excessive W and the carbon in the chamber can convert all the Co particles to an intermediate state of $\text{Co}_6\text{W}_6\text{C}$. As a consequence, no free Co phase exists in the as-reduced catalyst particles.

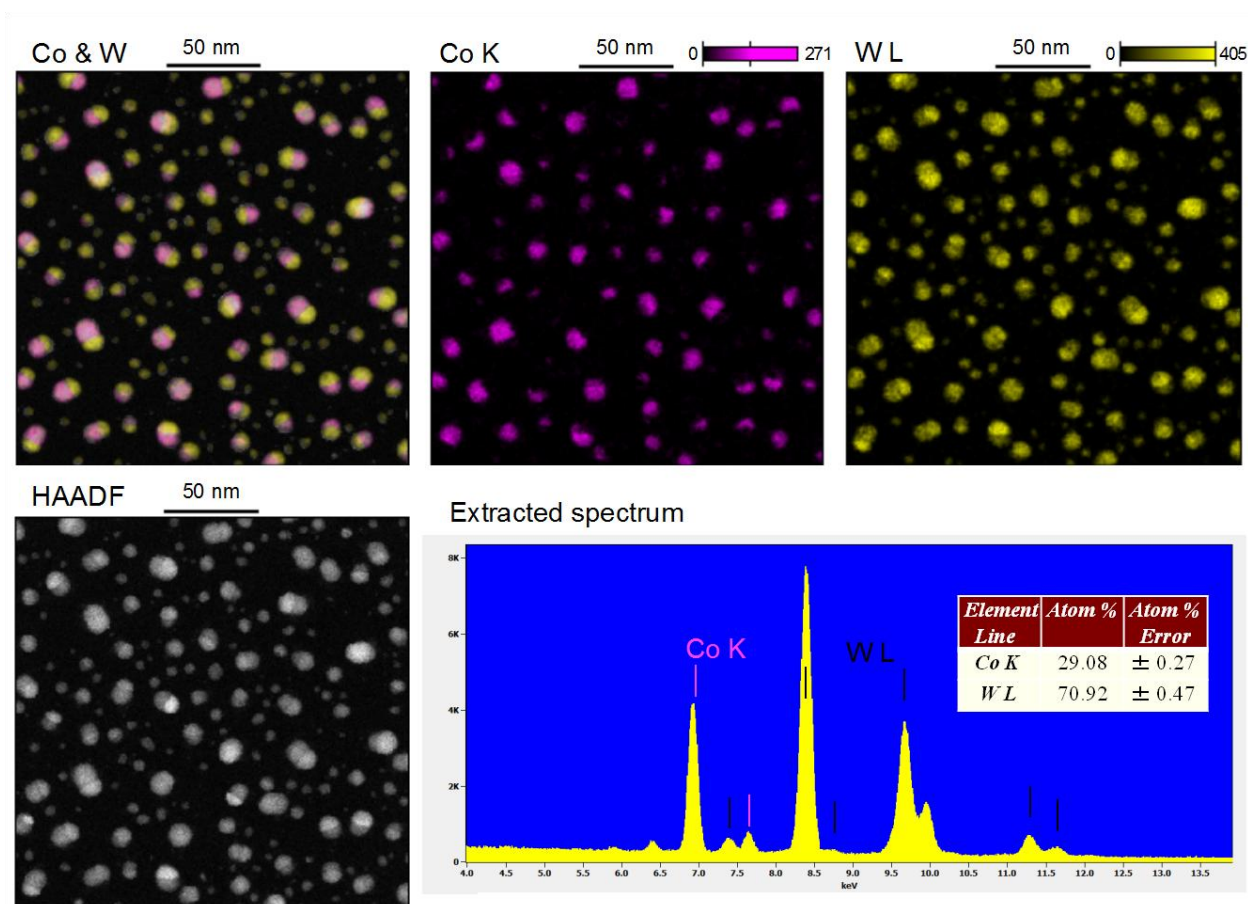


Figure 4.3 Elemental distribution mapping of the W-Co catalyst with water-assisted reduction at 850°C.

It is noticeable to find the junctions of W and $\text{Co}_6\text{W}_6\text{C}$ in the overlapped Co & W image and

the high resolution STEM images show a characteristic junction structure of the binary particle in Figure 4.4. The HAADF image on the left displays a near hexagonal shape of which the perfect lattice structure is assigned to body-centered cubic (BCC) W and the right part is a W-Co alloy while the blurry lattice makes it complex to assign to a certain phase. In fact, this W-Co alloy is very difficult to exhibit crossed lattice fringes even by tilting the sample. However, more TEM images demonstrate super lattice on the W-Co alloy part as shown in Figure 4.5. Since the electron diffraction shows a $\text{Co}_6\text{W}_6\text{C}$ pattern, the W-Co alloy in the junction part is very likely to be $\text{Co}_6\text{W}_6\text{C}$. As to why it is difficult to find a perfect crossed lattice fringes, we have further studied the crystal structure of $\text{Co}_6\text{W}_6\text{C}$.

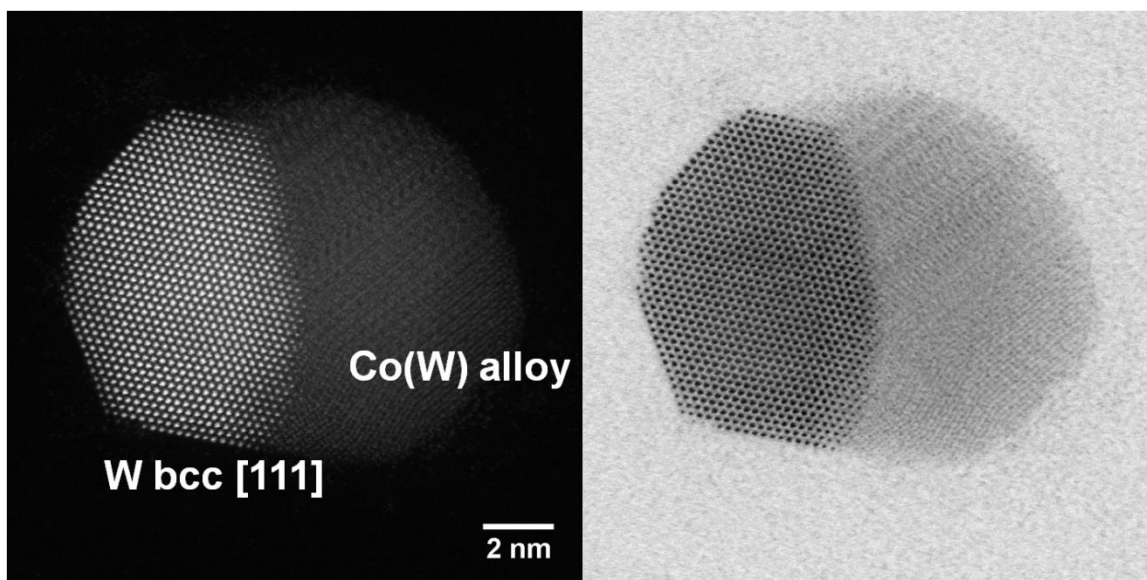


Figure 4.4 High resolution HAADF-STEM imaging and the bright field STEM image of the W-Co catalyst.

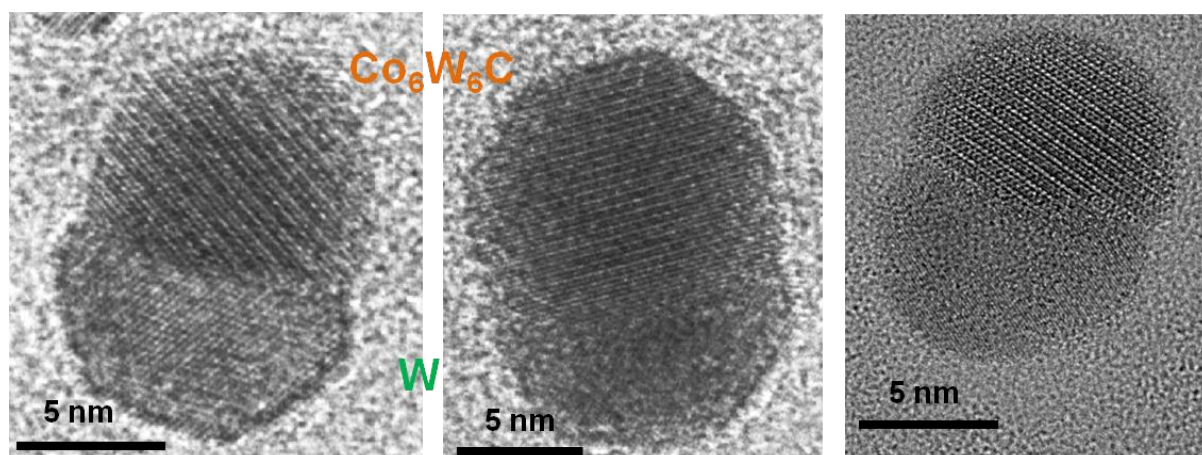


Figure 4.5 Super lattice structure of W-Co₆W₆C junctions with TEM.

Co₆W₆C is a FCC structure with 104 atoms in the unit cell. The 3D model of Co₆W₆C shows the complicated crystal structure. It is worthy to mention that by rotating the 3D model, quite few directions show perfect crossed lattice fringes. On the contrary, it is very easily to display a super lattice from different directions illustrated in Figure 4.6. That is why obtaining explicit crossed lattice fringes is difficult for Co₆W₆C alloy. In this way, the W-Co alloy part in the junction is very likely to be Co₆W₆C.

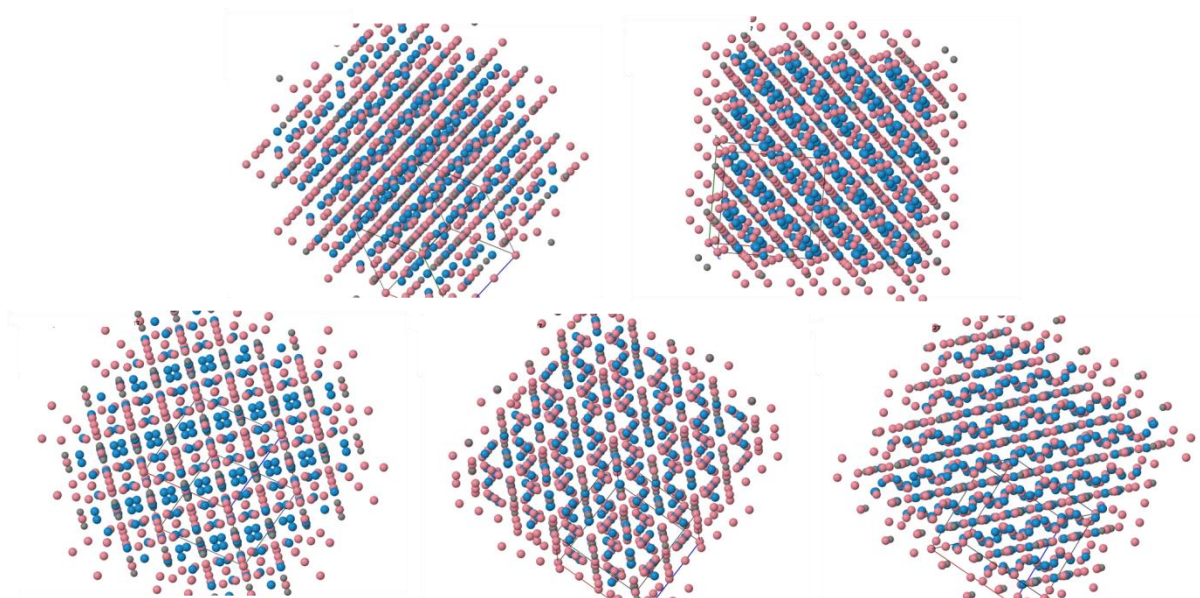


Figure 4.6 Super lattice structure by rotating the 3D model of Co₆W₆C [177].

4.2 Time-dependent growth of SWNTs with sputtered W-Co

The growth time is proved to be essential in the structure evolution of W-Co catalyst during ACCVD process within 5 min [170]. In previous study, SWNTs can grow very quickly upon the introduction of carbon source with Co catalyst from both the theoretical and experimental point of view [178, 179]. The rapid nucleation of SWNTs from catalyst can grow various kinds of chiralities with a general high yield of SWNTs [180]. In the case of W-Co bimetallic catalyst system, based on the aforementioned results, the incorporation of ethanol into the CVD chamber may initiate further structure changes of catalyst particles leading to a time-dependent selectivity on the catalyst structure. In order to investigate the structure evolution of the W-Co catalyst, an ex situ method with different growth time is performed. The W-Co catalyst from ex situ in-plane TEM demonstrates a structural evolution dependent on the growth time and it may indicate some hints towards selective growth of SWNTs.

4.2.1 Time-dependent growth of SWNTs

In order to investigate the time-dependent selectivity of SWNTs towards (12, 6), we first grow SWNTs with sputtered W-Co catalyst at the reduction temperature of 850°C, and manipulate the growth time from 10s to 5 min. The as-grown SWNT samples are then characterized by SEM and Raman spectroscopy with four lasers. The average Raman spectra can roughly show the selectivity and the chirality distribution.

The resultant SEM images in Figure 4.7 show that SWNTs can be found after 1 min growth. Compared with Co and CoMo catalyst, the incubation time of W-Co catalyst system is much longer which is always associated with the selective growth [181]. The obtained Raman spectra are shown in Figure 4.8. The dominant 197 cm^{-1} peak resonant with 633 nm displays the abundance of (12, 6) SWNTs. Note that the 1 min-growth sample shows better selectivity and after 3-min growth, the selectivity remains quite similar with the 5-min growth sample.

The time-dependent study reveals the gradual growth process and the increasing yield of the SWNT products. Consistent with SEM images, the relatively slow growth of SWNTs with W-Co catalyst leads to a lower yield compared to pure Co catalyst. Since Co can grow SWNTs very easily with ethanol, the retarded growth may suggest a quite different catalytic reaction at high temperature which is not as active as Co particles.

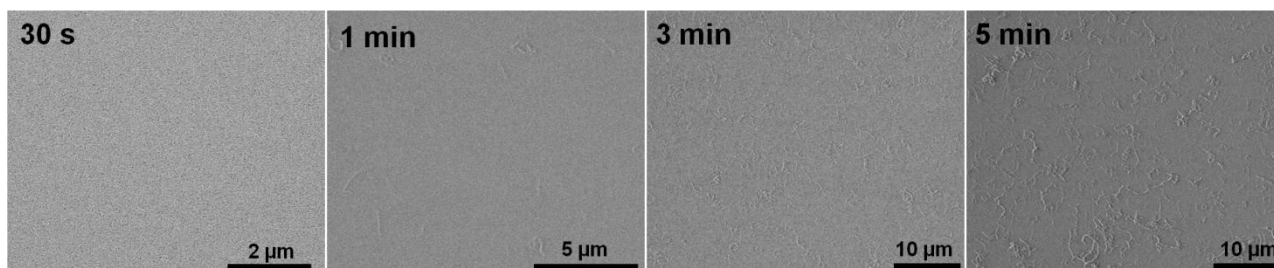


Figure 4.7 SEM images of SWNTs grown from sputtered W-Co with different growth time.

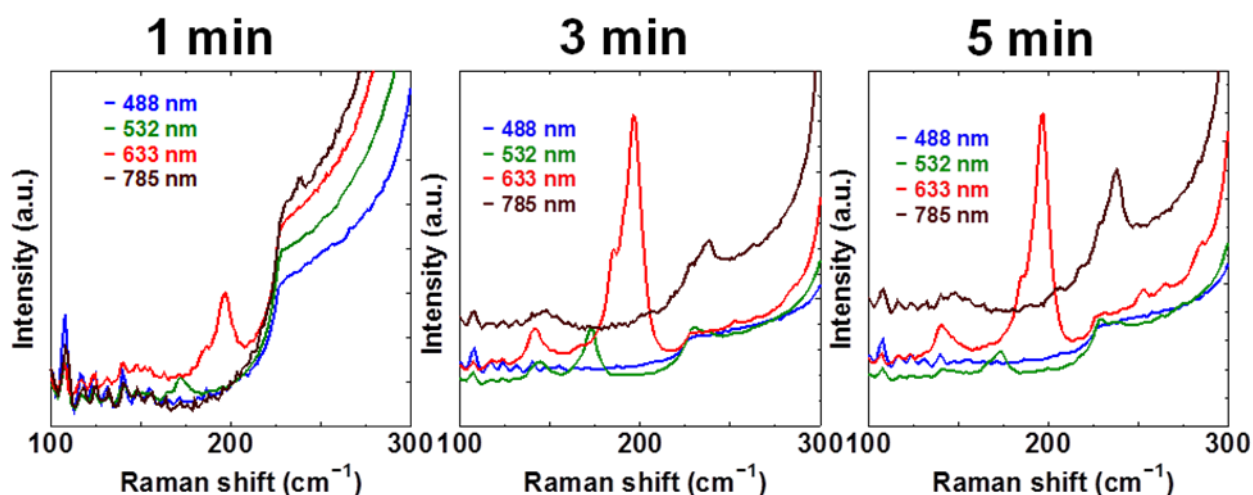


Figure 4.8 Raman spectra of SWNTs grown from sputtered W-Co with different growth time.

4.2.2 In-plane TEM observation of W-Co catalysts at different growth time

The W-Co catalyst structure with different growth time is then characterized by in-plane TEM method. The morphology evolution is shown in Figure 4.9. The catalyst particles can be recognized with different contrast on the microgrid substrate. The catalyst at 10s-growth stage shows similar morphology with the as-reduced ones. Note that from 30s-growth, the catalyst starts to possess some shadow structure with much weaker contrast compared to the

nanoparticles. What's more interesting is that the shadow parts expand while the nanoparticle volume shrinks with the prolongation of the growth time.

The electron diffraction can demonstrate the pattern rings from catalyst phases. The assignment of catalyst crystal phases is accomplished based on the previous study. A quite similar structure is illustrated at 10s-growth to the as-reduced catalyst. With the increase of growth time, the electron diffraction patterns change from W+Co₆W₆C phases to Co₆W₆C and Co related phases as shown in Figure 4.10. Furthermore, the differences between the as-reduced catalyst and the 10 s-growth, 30 s-growth and 1 min-growth catalyst include the relative ratio of strongest peaks from W and Co₆W₆C and the decrease of intensity from all pattern rings compared to the SiO₂ background. The additional rings at 3 min-growth is assigned to Co-related structure which is challenging to a final decision of a specific phase because of the partial oxidation of Co particles. This complicated phase evolution process is consistent with the changes of catalyst morphology and will be discussed later.

To demonstrate the relative amount of W and Co₆W₆C, the profile of the ring intensity is extracted and the ratio of intensity for 511 of Co₆W₆C to 110 of W is shown in the insets in Figure 4.11b. The standard W and Co₆W₆C profile are illustrated in Figure 4.11a for comparison. With the increase of the growth time, the ratio of intensity for Co₆W₆C to W raises indicating that the relative amount of Co₆W₆C is increasing. This means with further introduction of carbon, Co₆W₆C will gradually become the main crystal structure of the particles at the initial stage of growth. By combining with the SEM images, the yield of SWNTs displays a similar trend with Co₆W₆C at the early stage, which implies a hidden dependence of the nucleation of SWNTs on the Co₆W₆C particles in the W-Co catalyst system.

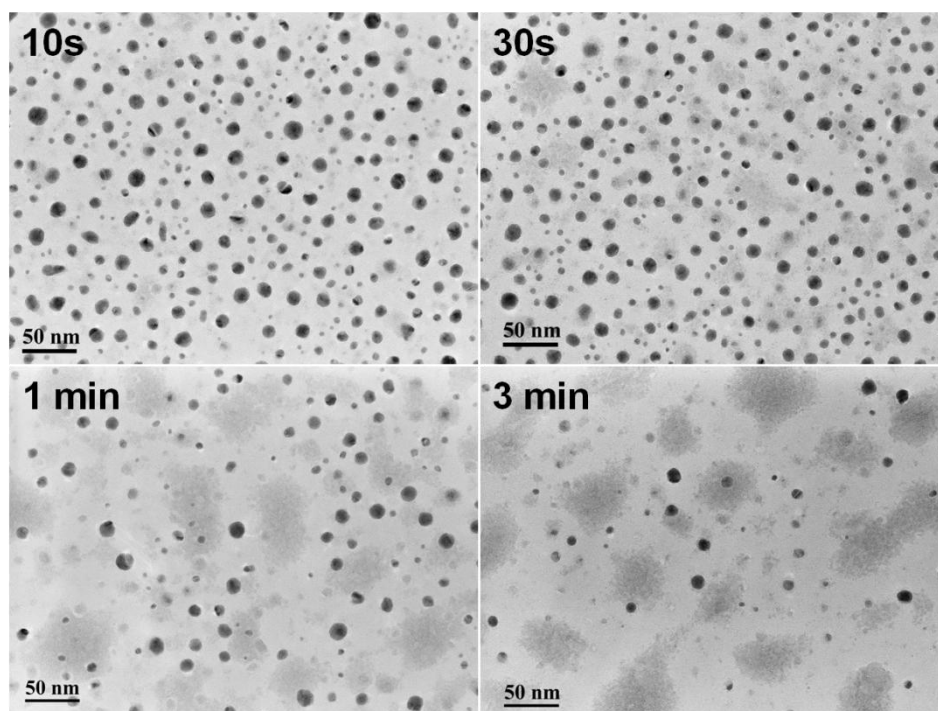


Figure 4.9 TEM morphology of W-Co catalyst system with different growth time.

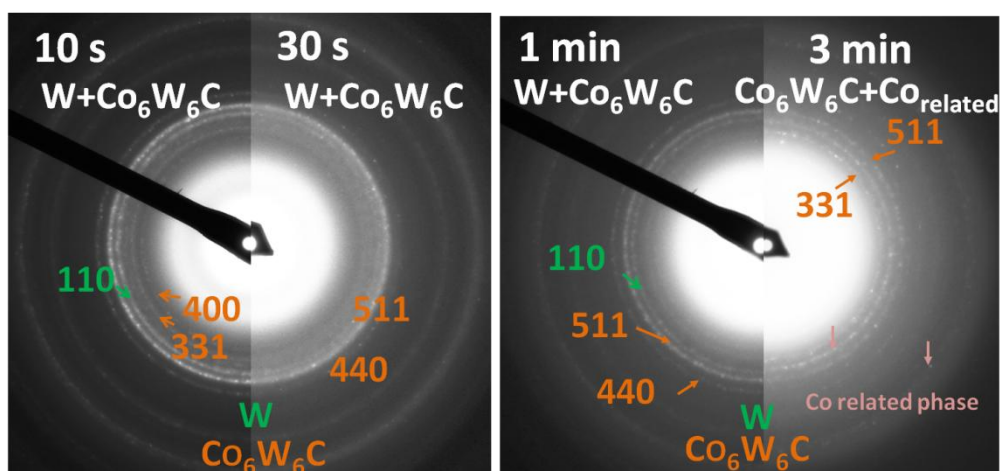


Figure4.10 Electron diffraction patterns of W-Co catalyst with different growth time.

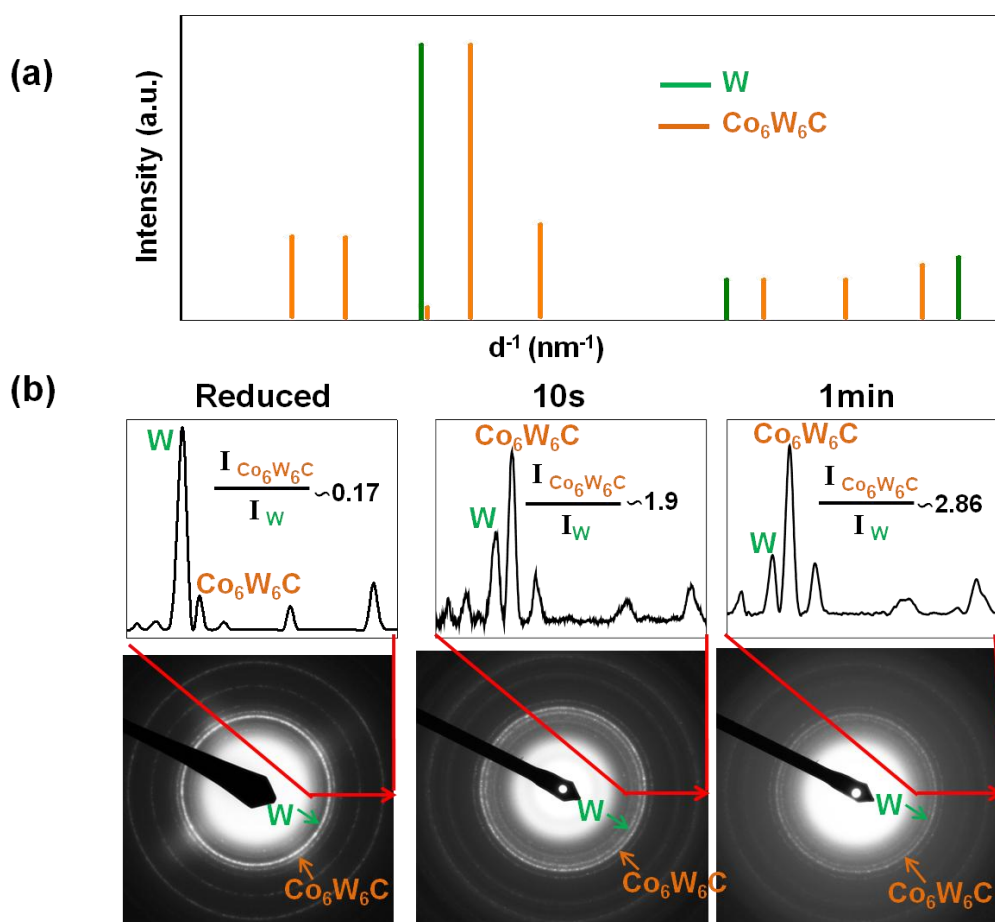


Figure 4.11 (a) Standard plot file of W and Co₆W₆C in PDF card. (b) Comparison of the relative amount of W and Co₆W₆C according to the intensity profile from the electron diffraction pattern.

In order to show the reduction tendency of W more clearly, the extracted EDS spectra with different growth time are normalized to Co and demonstrated in Figure 4.13. The distinct reduction of W and the corresponding atomic ratio provides a proof that W is “eaten” gradually during the CVD growth.

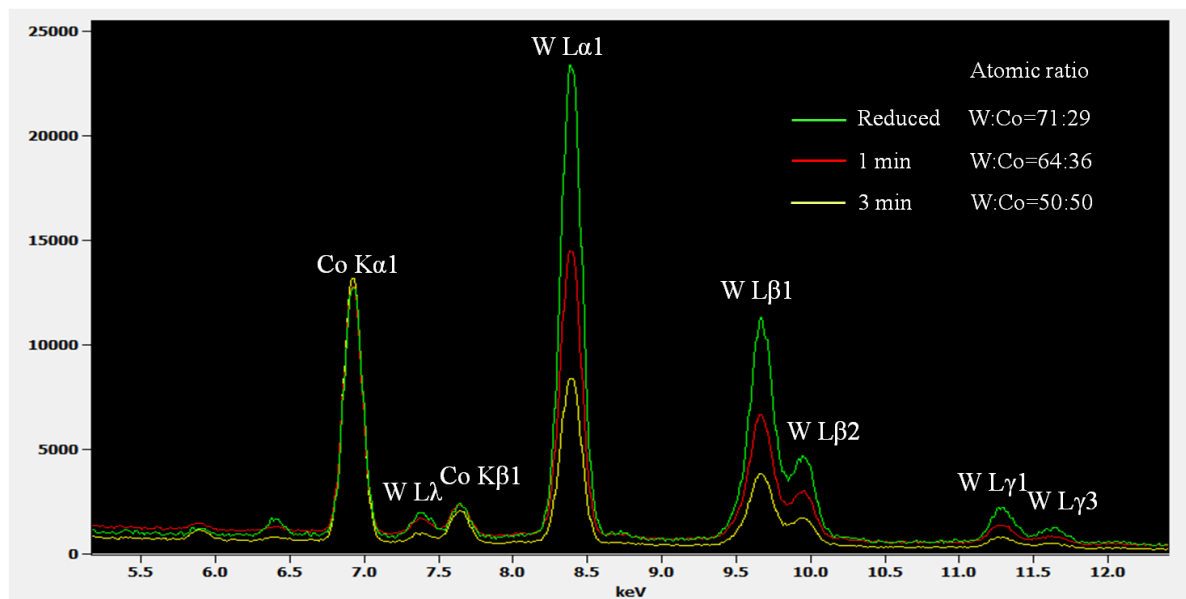


Figure 4.12 Time dependent EDS spectrum of W-Co catalyst showing a reduction tendency of W.

4.2.3 Discussions on the W-Co catalyst evolution with phase diagram

The study of growth mechanism and the structural changes of catalysts at high temperature are always accompanied with the phase diagram. Even though the nanoscale catalyst particles have some physical properties different from bulk materials, the supplementary information from the phase diagram also show some clues on the catalyst state at the carbonaceous surroundings and the possible mechanisms of the SWNT growth [182].

The W-Co-C ternary phase diagram from the literature at 1000°C (1273K) is shown in Figure 4.13 [183]. The $M_{12}C$ and M_6C represent Co_6W_6C and Co_3W_3C respectively. Note that there is a FCC phase of Co solid solution located at a Co-enriched corner of the diagram where C and W can dissolve into Co at this high temperature. A certain amount of Co_6W_6C has been produced during the heating and reduction process. The constituent point after reduction is corresponding to the mole fraction point at 0.7 from the sputtering parameter and EDS spectrum. It is probably on the segment of Co_6W_6C -W at the lower right region of the diagram shown as the asterisk since we can only find the electron diffraction pattern of W and Co_6W_6C without any Co_3W_3C and Co_7W_6 . After the introduction of ethanol, at the high

growth temperature, ethanol is decomposed to carbon and other species. Consequently, W can be oxidized and removed from the substrate in this condition through a gas phase reaction, resulting in an increase of the ratio of $\text{Co}_6\text{W}_6\text{C}$ with a left-shift of component point towards lower mole fraction of W. The further loss of W leads to a further shift to the possible state of FCC Co-enriched solid solution through the blue arrows where the precipitation of Co can be realized. Finally, at 5 min-growth, all the catalyst particles are converted to Co.

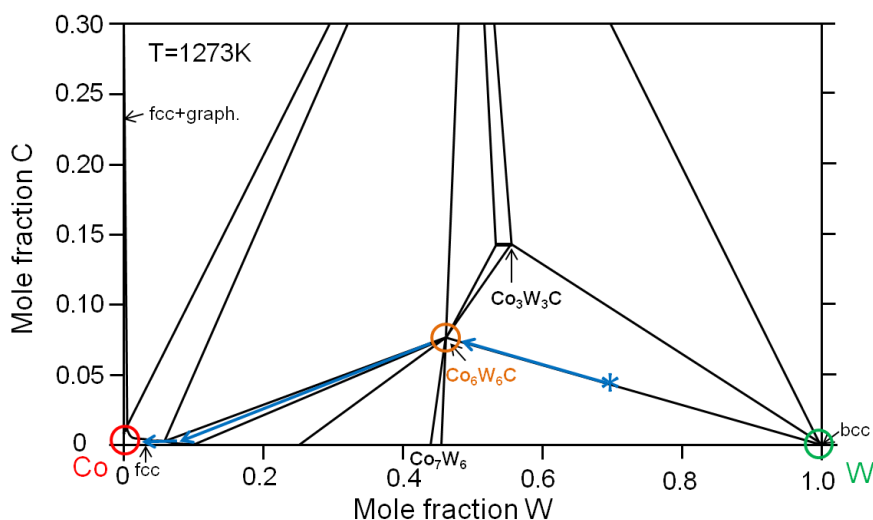


Figure 4.13 Phase diagram in literature to explain the phase evolution during the ACCVD process. Image drawn with reference to [183], Copyright (2005) with permission of Springer.

4.2.4 Intermediate structure of W-Co catalyst particles

A vivid characterization of time-dependent elemental distribution with EDS mapping is conducted and the images of as-reduced, 1 min and 3 min growth are shown in Figure 4.14. The as-reduced W-Co catalyst particles have been confirmed to be W+ $\text{Co}_6\text{W}_6\text{C}$ with a W- $\text{Co}_6\text{W}_6\text{C}$ binary junction morphology. Compared to the as-reduced W-Co particles, the 1 min-growth catalyst displays a similar elemental distribution with individual W particles and the W-Co binary particles, but some particles have an enrichment of Co. With the time going on, the 3 min-growth sample shows more Co enriched area than the 1 min-growth sample and some particles have completed the structure transformation to pure Co.

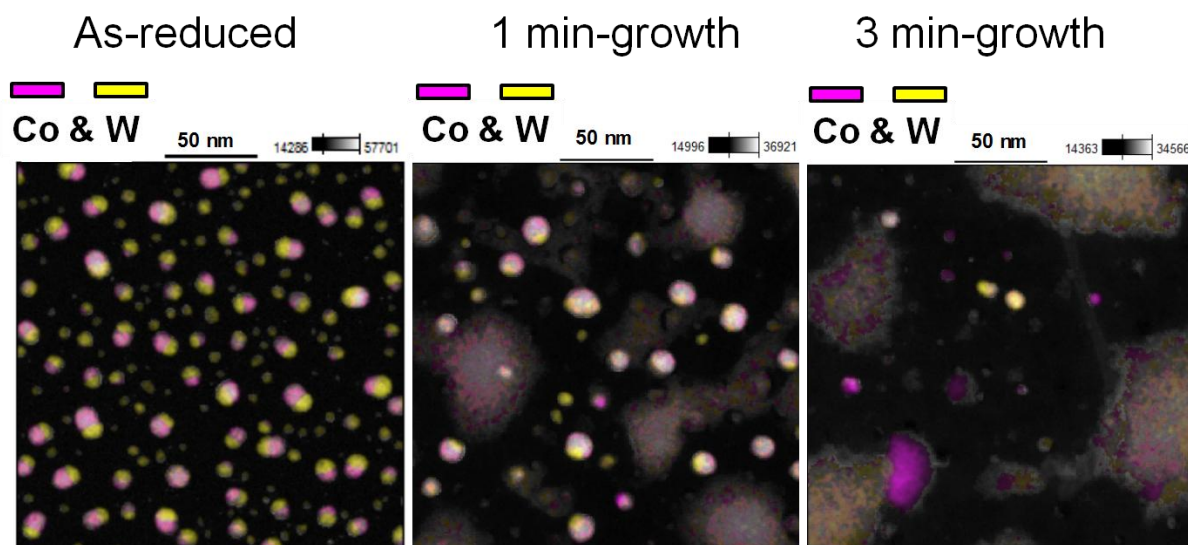


Figure 4.14 Elemental distribution of the W-Co catalyst at different growth time.

The structural changes experienced by individual catalyst particles are characterized by high resolution TEM techniques. During the ACCVD growth, we could find a binary structure shown in Figure 4.15. The left part displays a super lattice while the right part shows perfect crossed fringes with a right angle. This lattice from the right part indicates the crystal structure is very simple with an interplanar spacing of 1.98\AA . However, this interplanar spacing can neither match with a BCC W nor a FCC Co shown in Figure 4.16 where the cross angle is 90° . Note that the value from the intermediate phase of W-Co catalyst is somehow located between BCC W and FCC Co. Other phases from W or Co related phases possibly in this system are excluded because of their complex crystal structure (from 3D model) or the image contrast. Thus it is probably a Co enriched solid solution in accordance with the phase diagram. The unique orientation of the interface in the binary particle may highlight a stability mechanism from the W-Co alloy for the solid solution which needs further study on these special binary particles.

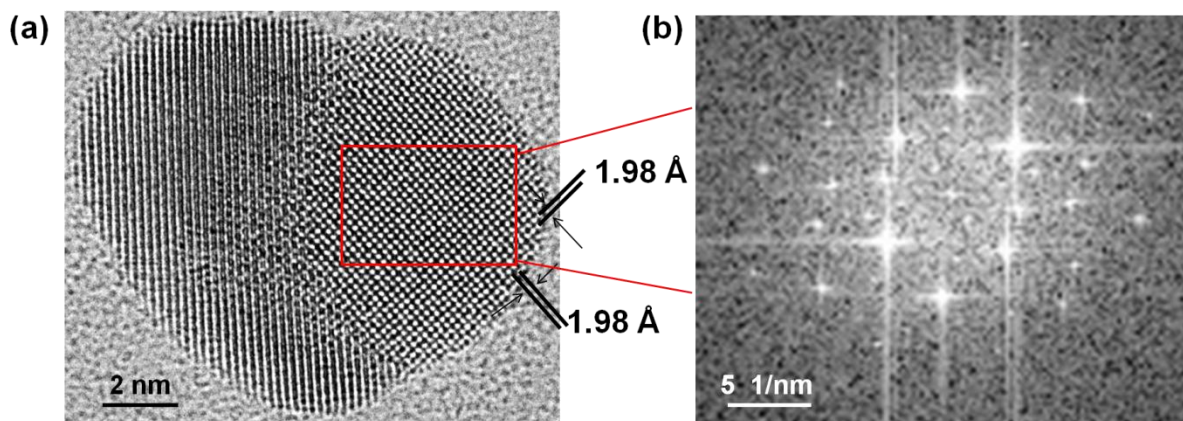


Figure 4.15 (a) Lattice structure of the W-Co junction particle during ACCVD growth, (b) FFT pattern of the W-Co particle from the red rectangle part in (a).

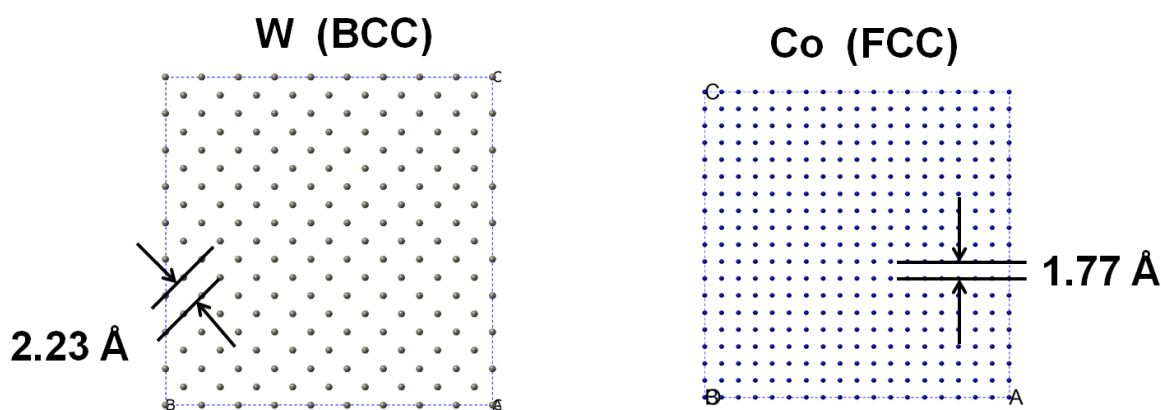


Figure 4.16 The lattice pattern from W and Co crystal with the direction showing a right angle.

This kind of intermediate solid solution can be further characterized by STEM in Figure 4.17. The high resolution bright field image on the right in Figure 4.17 (a) also displays a simple lattice structure. However, the HAADF image on the left shows an elemental distribution of W and Co with different contrast. The image contrast of atoms is dependent on their atomic number where the bright atoms are W and the gray atoms are Co. As demonstrated in the HAADF image, the atoms distribute uniformly with the lattice fringes only at the lower right corner of this particle while other parts of this particle displays a nonuniform image contrast indicating the disordered atom distribution. The EDS mapping images in Figure 4.17(b) further verify a Co-enriched particle with an ordered lattice at the corner clarifying a potential Co solid solution phase.

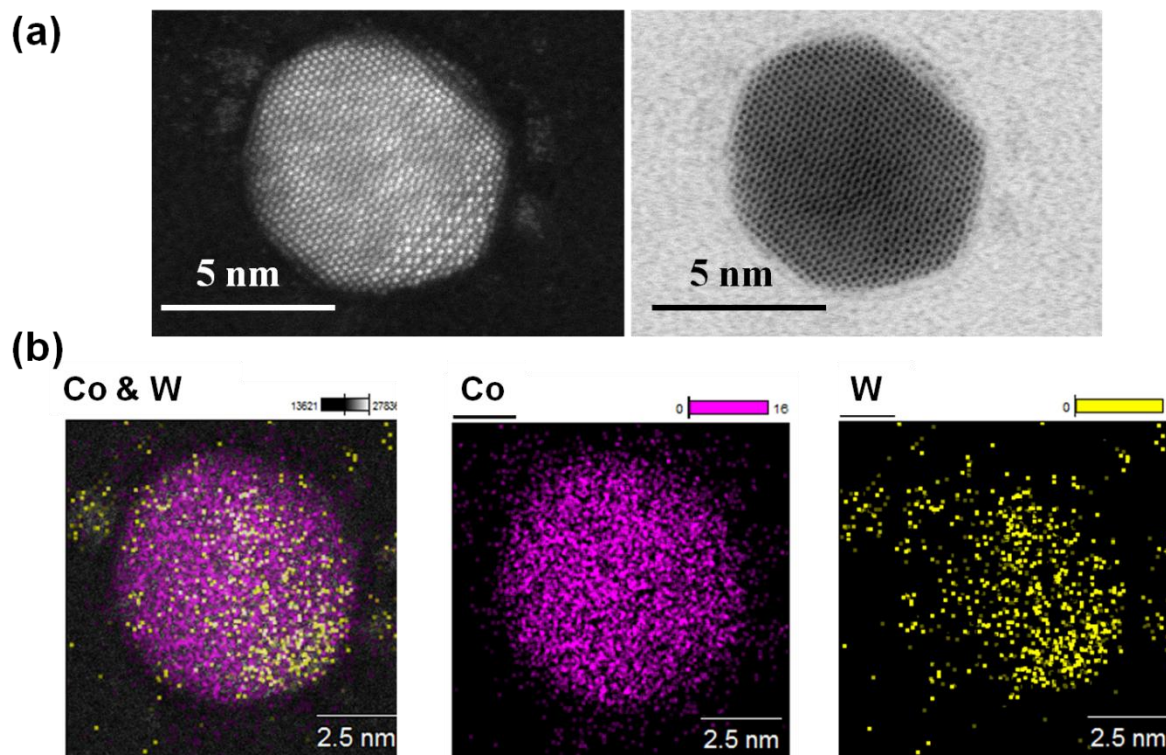


Figure 4.17 STEM images (a) and the elemental distribution (b) of the W-Co particle.

4.2.5 Possible mechanism of the structure evolution of W-Co catalyst during the growth of SWNTs with ethanol

Based on the previous study about the structure evolution of W-Co catalyst particles, a possible mechanism is proposed as shown in Figure 4.18. As discussed previously, the as-reduced particles are W and $\text{Co}_6\text{W}_6\text{C}$ junctions, after the introduction of ethanol, tungsten will be progressively removed by the products of ethanol decomposition and the relative amount of $\text{Co}_6\text{W}_6\text{C}$ will be increased. As the loss of W going on, the ratio of $\text{Co}_6\text{W}_6\text{C}$ keep increasing while the total amount of W is decreasing shown at 1 min-growth in Figure 4.18. With further losing of W, after 3 min-growth, a Co or Co solid solution will be precipitated from the alloy particles. At this stage, the (12, 6) SWNT cap may be selectively formed from Co part because no SWNTs can be grown from W as shown in Figure 3.12. Finally, most of the catalyst particles are converted to Co at 5 min-growth with a selectivity towards (12, 6). As discussed above, $\text{Co}_6\text{W}_6\text{C}$ is strongly related to the nucleation stage of (12, 6) SWNTs. More pure $\text{Co}_6\text{W}_6\text{C}$ particles may further enhance the selectivity which offers a possible

strategy to synthesize single-chirality SWNTs for future large-scale applications.

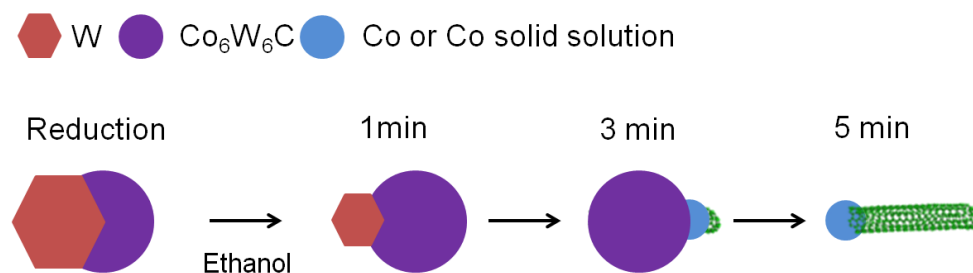


Figure 4.18 Structure evolution of W-Co catalyst during the growth of SWNTs with ethanol.

4.3 Summary

In this chapter, a detailed investigation of catalyst structure and evolution during the growth process in ACCVD is demonstrated. The as-reduced catalyst particles are verified to be W and Co₆W₆C with an experimental acid treatment and elemental mapping of the catalyst particles. The as-reduced catalyst particles will undergo a complicated dynamic evolution upon the introduction of ethanol at the growth temperature. The evolution of catalyst shows a transitional process from W+ Co₆W₆C to pure Co within 5 min-growth indicating a possible mechanism of selective growth towards (12, 6) with W-Co bimetallic catalyst system. Further efforts are needed to obtain single-chirality SWNTs to improve the performance of SWNTs-based nanodevices.

Chapter 5 Conclusions

5.1 Summary of the dissertation

The specific structure of single-walled carbon nanotubes (SWNTs) defines their physical properties and the corresponding applications of SWNTs. Various chiralities of SWNTs due to the diversity of rolling up process from a graphene sheet enrich the SWNT families and provide plentiful properties with discrete changes. The structure-dependent properties enable diverse possibilities for the applications in various kinds of nanodevices. In sophisticated technology, even though the variety of SWNTs provides a broad performance window, a more definite property from homogeneous materials for nanodevices is required. It suggests that SWNTs with homogeneous structure-single chirality, is highly desired in SWNTs-based nanodevices.

Synthesis of SWNTs with specific chirality is challenging not only because of the uncertainty of catalyst structure at high growth temperature but also due to the lack of understanding of detailed growth mechanism. An in-plane TEM method is proposed to further investigate the underlying mechanism with various mono and bimetallic catalyst compositions. The in-plane TEM method proves to be successful with the study of small-diameter SWNTs grown from CuCo bimetallic catalyst. This method provides a powerful tool for the investigation of growth mechanism of SWNTs.

A simple sputtering method is utilized to prepare the W-Co catalyst and this bimetallic catalyst shows a similar selectivity towards (12, 6) to the previous report. The as-grown SWNTs are characterized to estimate the content of (12, 6) with absorption and statistical Raman mapping method. The abundance of (12, 6) grown from sputtered W-Co can be as high as 50%-70%. The intermediate state of $\text{Co}_6\text{W}_6\text{C}$ is identified with in-plane TEM. This carbide structure is found to be correlated with the selectivity at high reduction temperature which is much more different from the catalyst structure at low reduction temperature.

The as-reduced catalyst particles are verified to be W and $\text{Co}_6\text{W}_6\text{C}$ based on the acid-treatment experiment and the EDS elemental mapping with in-plane TEM method. Time-dependent study demonstrates a consistent relationship between the selectivity and the structure evolution of W-Co bimetallic catalyst. Further investigation on the selective growth with $\text{Co}_6\text{W}_6\text{C}$ is needed to understand the hidden mechanism and to realize the single-chirality synthesis of SWNTs.

5.2 Prospects

Future work on this topic will mainly focus on the optimization of the selectivity and the selective synthesis of SWNTs towards other chiralities possibly semiconducting SWNTs for applications in nanodevices. Characterization on the catalyst structure and SWNTs needs further efforts and the *in situ* TEM study on the structure evolution of catalyst and the dependence of carbon content on the nucleation and growth of SWNTs will help further understanding of the selective mechanisms.

Not only the successful selective growth of SWNTs is important but also the failure of selectivity of SWNTs at other CVD conditions plays an important role in the synthetic field of SWNTs. The hard metal of W-Co-C is widely studied in the engineering applications, in this case, the well prepared $\text{Co}_6\text{W}_6\text{C}$ nanoparticles may bring a much better selectivity based on the mechanism study of W-Co bimetallic catalyst system.

Bibliography

- [1] L.P. Biró, P. Nemes-Incze, P. Lambin. “Graphene: nanoscale processing and recent applications”. *Nanoscale*, 2012, **4**:1824-1839.
- [2] M.S. Dresselhaus, G. Dresselhaus, R. Saito, A. Jorio. “Raman spectroscopy of carbon nanotubes”. *Physics Reports*, 2005, **409**: 47-99.
- [3] R. Saito, G. Dresselhaus and M. S. Dresselhaus, “Physical properties of Carbon Nanotubes”, Imperial Collage Press, 2007.
- [4] S. Iijima, T. Ichihashi, “ Single-shell carbon nanotubes of 1-nm diameter”. *Nature*, 1993, **363**: 603-605.
- [5] D.S. Bethune, C.H. Kiang, M.S. de Vries, G. Gorman, R. Savoy, J. Vazquez, R. Beyers. “Cobalt-catalysed growth of carbon nanotubes with single-atomic-layer walls”. *Nature*, 1993, **363**: 605-607.
- [6] N. Arora, N.N. Sharma. “Arc discharge synthesis of carbon nanotubes: Comprehensive review”. *Diamond & Related Materials*, 2014, **50**: 135-150.
- [7] J. Prasek, J. Drbohlavova, J. Chomoucka, J. Hubalek, O. Jasek, V. Adam, R. Kizek. “Methods for carbon nanotubes synthesis-review”. *Journal of Materials Chemistry*, 2011, **21**: 15872-15884.
- [8] T. Guo, P. Nikolaev, A. Thess, D.T. Colbert, R.E. Smalley. “Catalytic growth of single-walled nanotubes by laser vaporization”. *Chemical Physics Letters*, 1995, 243: 49-54.
- [9] M. Wilson, K. Kannagara, G. Smith, M. Simmons, B. Raguse. “Nanotechnology: Basic science and emerging technologies”. Chapman and Hall/CRC Press, 2002.
- [10] S. Maruyama, R. Kojima, Y. Miyauchi, S. Chiashi, M. Kohno. “Low-temperature synthesis of high-quality single-walled carbon nanotubes from alcohol”. *Chemical Physics Letters*, 2002, **360**: 229-234.
- [11] M. Cantoro, S. Hofmann, S. Pisana, V. Scardaci, A. Parvez, C. Ducati, A.C. Ferrari, A.M. Blackburn, K. Wang, J. Robertson. “Catalytic chemical vapor deposition of single-walled

carbon nanotubes at low temperature”. *Nano Letters*, 2006, **6** (6):1107-1112.

[12] J. Kong, A.M. Cassell, H. Dai. “Chemical vapor deposition of methane for single-walled carbon nanotubes”. *Chemical Physics Letters*, 1998, **292**: 567-574.

[13] M. Kumar, Y. Ando. “Chemical vapor deposition of carbon nanotubes: a review on growth mechanism and mass production”. *Journal of Nanoscience and nanotechnology*, 2010, **10**: 3739-3758.

[14] T. Umino, T. Inoue, S. Chiashi, S. Maruyama. “Cloning growth of single-walled carbon nanotubes from activated nanotube edges”. *46th Fullerenes-Nanotubes-Graphene General Symposium*, 2014.

[15] D. Yuan, L. Ding, H. Chu, Y. Feng, T.P. McNicholas, J. Liu. “Horizontally aligned single-walled carbon nanotube on quartz from a large variety of metal catalysts”. *Nano Letters*, 2008, **8**(8): 2576-2579.

[16] B. Hou. “CVD growth of super-small diameter single-walled carbon nanotubes”, Tokyo, University of Tokyo, 2015, 1-105.

[17] R.T.K. Baker, P.S. Harris, R.B. Thomas, R.J. Waite. “Formation of filamentous carbon from iron, cobalt, and chromium catalyzed decomposition of acetylene”. *Journal of Catalysis*, 1973, **30**: 86-95.

[18] R.S. Wagner, W.C. Ellis. “Vapor-liquid-solid mechanism of single crystal growth”. *Applied Physics Letters*, 1964. **4**(5): 89-90.

[19] E.F. Kukovitsky, S.G. L’vov, N.A. Sainov. “VLS-growth of carbon nanotubes from the vapor”. *Chemical Physics Letters*, 2000, **317**: 65-70.

[20] V. Jourdain, C. Bichara. “Current understanding of the growth of carbon nanotubes in catalytic chemical vapour deposition”. *Carbon*, 2013, **58**: 2-39.

[21] R.A. Couttenye, M.H. De Vila, S.L. Suib, “Decomposition of methane with an autocatalytically reduced nickel catalyst”. *Journal of Catalysis*, 2005, **233**(2): 317-326.

[22] B. Hou, R. Xiang, T. Inoue, E. Einarsson, S. Chiashi, J. Shiomi, A. Miyoshi, S. Maruyama. “Decomposition of ethanol and dimethyl ether during chemical vapor deposition synthesis of single-walled carbon nanotubes”. *Japanese Journal of Applied Physics*, 2011, **50**:

065101.

[23] Q. Wang, M.F. Ng, S.W. Yang, Y. Yang, Y. Chen. "The mechanism of single-walled carbon nanotube growth and chirality selection induced by carbon atom and dimer addition". *ACS Nano*, 2010, **4**(2): 939-946.

[24] A.J. Page, Y. Ohta, S. Irle, A.K. Morokuma. "Mechanisms of single-walled carbon nanotube nucleation, growth, and healing determined using QM/MD methods". *Accounts of Chemical Research*, 2010, **43**(10): 1375-1385.

[25] R. Xiang, B. Hou, E. Einarsson, P. Zhao, S. Harish, K. Morimoto, Y. Miyauchi, S. Chiashi, Z. Tang, S. Maruyama. "Carbon atoms in ethanol do not contribute equally to formation of single-walled carbon nanotubes". *ACS Nano*, 2013, **7**(4): 3095-3103.

[26] M. Yudasaka, Y. Kasuya, F. Kokai, K. Takahashi, M. Takizawa, S. Bandow, S. Iijima. "Causes of different catalytic activities of metals in formation of single-wall carbon nanotubes". *Applied Physics A*, 2002, **74**: 377-385.

[27] M. Takagi. "Electron-diffraction study of liquid-solid transition of thin metal films". *Journal of the Physical Society of Japan*, 1954, **9**(3): 359-363.

[28] H. Yoshida, T. Shimizu, T. Uchiyama, H. Kohno, Y. Homma, S. Takeda. "Atomic-scale analysis on the role of molybdenum in iron-catalyzed carbon nanotube growth". *Nano Letters*, 2009, **9**(11):3810-3815.

[29] Y. Shiratori, H. Hiraoka, M. Yamamoto. "Vertically aligned carbon nanotubes produced by radio-frequency plasma-enhanced chemical vapor deposition at low temperature and their growth mechanism". *Materials Chemistry and Physics*, 2004, **87**:31-38.

[30] M. Diarra, A. Zappelli, H. Amara, F. Ducastelle, C. Bichara. "Importance of carbon solubility and wetting properties of nickel nanoparticles for single wall nanotube growth". *Physical Review Letters*, 2012, **109**: 185501.

[31] O.V. Yazyev, A. Pasquarello. "Effect of metal elements in catalytic growth of carbon nanotubes". *Physical Review Letters*, 2008, **100**:156102.

[32] S. Esconjauregui, C.M. Whelan, K. Maex. "The reasons why metals catalyze the nucleation and growth of carbon nanotubes and other carbon nanomorphologies". *Carbon*,

2009, **47**: 659-669.

[33] C. Emmenegger, J.-M. Bonard, P. Mauron, P. Sudan, A. Lepora, B. Grobety, A. Züttel, L. Schlapbach. "Synthesis of carbon nanotubes over Fe catalyst on aluminium and suggested growth mechanism". *Carbon*, 2003, **41**: 539-547.

[34] R. Sharma, E. Moore, P. Rez, M.J. Treacy. "Site-specific fabrication of Fe particles for carbon nanotube growth". *Nano Letters*, 2009, **9(2)**: 689-694.

[35] H. Yoshida, S. Takeda, T. Uchiyama, H. Kohno, Y. Homma. "Atomic-scale in-situ observation of carbon nanotube growth from solid state iron carbide nanoparticles". *Nano Letters*, 2008, **8(7)**: 2082-2086.

[36] J.A. Rodríguez-Manzo, M. Terrones, H. Terrones, H.W. Kroto, L. Sun, F. Banhart. "In situ nucleation of carbon nanotubes by the injection of carbon atoms into metal particles". *Nature Nanotechnology*, 2007, **2**: 307-311.

[37] X. Qin, F. Peng, F. Yang, X. He, H. Huang, D. Luo, J. Yang, S. Wang, H. Liu, L. Peng, Y. Li. "Growth of semiconducting single-walled carbon nanotubes by using ceria as catalyst supports". *Nano Letters*, 2014, **14**: 512-517.

[38] S. Reich, L. Li, J. Robertson. "Control of chirality of carbon nanotubes by epitaxial growth". *Chemical Physics Letters*, 2006, **421**: 469-472.

[39] L. Kang, S. Zhang, Q. Li, J. Zhang. "Growth of horizontal semiconducting SWNT arrays with density higher than 100 tubes/ μm using ethanol/methane CVD". *Journal of American Chemical Society*, 2016, **138(21)**: 6727-6730.

[40] Q. Zhao, Z. Xu, Y. Hu, F. Ding, J. Zhang. "Chemical vapor deposition synthesis of near-zigzag single-walled carbon nanotubes with stable tube-catalyst interface". *Science Advances*, 2016, **2(5)**: e1501729.

[41] S. Sakurai, M. Yamada, H. Sakurai, A. Sekiguchi, D.N. Futaba, K. Hata. "A phenomenological model for selective growth of semiconducting single-walled carbon nanotubes based on catalyst deactivation". *Nanoscale*, 2016, **8**: 1015-1023.

[42] P. Diao, Z. Liu. "Vertically aligned single-walled carbon nanotubes by chemical assembly- methodology, properties, and applications". *Advanced Materials*, 2010, **22**:

1430-1449.

[43] H. Chen, A. Roy, J. Baek, L. Zhu, J. Qu, L. Dai. "Controlled growth and modification of vertically aligned carbon nanotubes for multifunctional applications". *Materials Science and Engineering R*, 2010, **70**: 63-91.

[44] J. Zaumseil. "Single-walled carbon nanotubes networks for flexible and printed electronics". *Semiconductor Science and Technology*, 2015, **30**: 074001.

[45] T. Chen, Y. Zhang, Y. Hu, L. Kang, S. Zhang, H. Xie, D. Liu, Q. Zhao, Q. Li, J. Zhang. "State of the art of single-walled carbon nanotube synthesis on surfaces". *Advanced Materials*, 2014, **26**: 5898-5922.

[46] L.M. Ericson, H. Fan, H. Peng, V.A. Davis, W. Zhou, J. Sulpizio, Y. Wang, R. Booker, J. Vavro, C. Guthy, A. Nicholas, G.P. Vasquez, M.J. Kim, S. Ramesh, R.K. Saini, C. Kittrell, G. Lavin, H. Schmidt, W.W. Adams, W.E. Billups, M. Pasquali, W. Hwang, R.H. Hauge, J.E. Fischer, R.E. Smalley. "Macroscopic, neat, single-walled carbon nanotube fibers". *Science*, 2004, **305**: 1447-1450.

[47] P.W. Barone, S. Baik, D.A. Heller, M.S. Strano. "Near-infrared optical sensors based on single-walled carbon nanotubes". *Nature Materials*, 2005, **4**: 86-92.

[48] Z. Chen, J. Appenzeller, Y. Lin, J.S. Oakley, A.G. Rinzler, J. Tang, S.J. Wind, P.M. Solomon, P. Avouris. "An integrated logic circuit assembled on a single carbon nanotube". *Science*, 2006, **311**: 1735.

[49] I. Heller, J. Kong, H.A. Heering, K.A. Williams, S.G. Lemay, C. Dekker. "Individual single-walled carbon nanotubes as nanoelectrodes for electrochemistry". *Nano Letters*, 2005, **5** (1): 137-142.

[50] A.D. Franklin, M. Luisier, S. Han, G. Tulevski, C.M. Breslin, L. Gignac, M.S. Lundstrom, W. Haensch. "Sub-10 nm carbon nanotube transistor". *Nano Letters*, 2012, **12**: 758-762.

[51] S.B. Desai, S.R. Madhvapathy, A.B. Sachid, J.P. Llinas, Q. Wang, G.H. Ahn, G. Pitner, M.J. Kim, J. Bokor, C. Hu, H.P. Wong, A. Javey. "MoS₂ transistors with 1-nanometer gate lengths". *Science*, 2016, **354**(6308):99-102.

- [52] Y. Murakami, S. Chiashi, Y. Miyauchi, M. Hu, M. Ogura, T. Okubo, S. Maruyama. "Growth of vertically aligned single-walled carbon nanotube films on quartz substrates and their optical anisotropy". *Chemical Physics Letters*, 2004, **385**: 298-303.
- [53] Y. Ma, B. Wang, Y. Wu, Y. Huang, Y. Chen. "The production of horizontally aligned single-walled carbon nanotubes". *Carbon*, 2011, **49**:4098-4110.
- [54] T. Inoue, D. Hasegawa, S. Badar, S. Aikawa, S. Chiashi, S. Maruyama. "Effect of gas pressure on the density of horizontally aligned single-walled carbon nanotubes grown on quartz substrates". *The Journal of Physical Chemistry C*, 2013, **117**(22): 11804-11810.
- [55] D. Zhang, K. Ryu, X. Liu, E. Polikarpov, J. Ly, M.E. Tompson, C. Zhou. "Transparent, conductive, and flexible carbon nanotube films and their application in organic light emitting diodes". *Nano Letters*, 2006, **6** (9): 1880-1886.
- [56] L.M. Ericson, H. Fan, H. Peng, V.A. Davis, W. Zhou, J. Sulpizio, Y. Wang, R. Booker, J. Vavro, C. Guthy, A.N.G. Parra-Vasquez, M.J. Kim, S. Ramesh, R.K. Saini, C. Kittrell, G. Lavin, H. Schmidt, W.W. Adams, W.E. Billups, M. Pasquali, W. Hwang, R.H. Hauge, J.E. Fischer, R.E. Smalley. "Macroscopic, neat, single-walled carbon nanotube fibers". *Science*, 2004, **305**: 1447-1450.
- [57] K. Cui, T. Chiba, S. Omiya, T. Thurakitseree, P. Zhao, S. Fujii, H. Kataura, E. Einarsson, S. Chiashi, S. Maruyama, "Self-assembled microhoneycomb network of single-walled carbon nanotubes for solar cells". *The Journal of Physical Chemistry Letters*, 2013, **4**:2571-2576.
- [58] G.J. Brady, A.J. Way, N.S. Safron, H.T. Evensen, P. Gopalan, M.S. Arnold. "Quasi-ballistic carbon nanotube array transistors with current density exceeding Si and GaAs". *Science Advance*, 2016, **2** (9): e1601240.
- [59] Z. Wu, Z. Chen, X. Du, J.M. Logan, J. Sippel, M. Nikolou, K. Kamaras, J.R. Reynolds, D.B. Tanner, A.F. Hebard, A.G. Rinzler. "Transparent, conductive carbon nanotube films". *Science*, 2004, **305**: 1273-1276.
- [60] K. Cui, A.S. Anisimov, T. Chiba, S. Fujii, H. Kataura, A.G. Nasibulin, S. Chiashi, E. I. Kauppinen, S. Maruyama. "Air-stable high-efficiency solar cells with dry-transferred single-walled carbon nanotube films". *J. Mater. Chem. A*, 2014, **2**, 11311-11318.

- [61] H. Koo, W. Lee, Y. Choi, J. Sun, J. Bak, J. Noh, V. Subramanian, Y. Azuma, Y. Majima, G. Cho. "Scalability of carbon-nanotube-based thin film transistors for flexible electronic devices manufactured using an all roll-to-roll gravure printing system". *Sci. Rep.*, 2015, **5**: 14459.
- [62] M.C. LeMieux, M. Roberts, S. Barman, Y.W. Jin, J.M. Kim, Z. Bao. "Self-sorted, aligned nanotube networks for thin-film transistors". *Science*, 2008, **321**: 101-104.
- [63] R.H. Baughman, A.A. Zakhidov, W.A. de Heer. "Carbon nanotubes-the route toward applications". *Science*, 2002, **297**: 787-792.
- [64] B. Liu, C. Wang, J. Liu, Y. Che, C. Zhou. "Aligned carbon nanotubes: from controlled synthesis to electronic applications". *Nanoscale*, 2013, **5**: 9483-9502.
- [65] T. Dürkop, S.A. Getty, E. Cobas, M.S. Fuhrer. "Extraordinary mobility in semiconducting carbon nanotubes". *Nano Letters*, 2004, **4** (1): 35-39.
- [66] M.C. Hersam. "Progress towards monodisperse single-walled carbon nanotubes". *Nature Nanotechnology*, 2008, **3**: 387-394.
- [67] J.P. Tessonier, D.S. Su. "Recent progress on the growth mechanism of carbon nanotubes: a review". *ChemSusChem*, 2011, **4**: 824-847.
- [68] Y. Murakami, Y. Miyauchi, S. Chiashi, S. Maruyama, "Direct synthesis of high-quality single-walled carbon nanotubes on silicon and quartz substrates". *Chemical Physics Letters*, 2003, **377**: 49-54.
- [69] K. Wasa. "Handbook of sputter deposition technology, second edition: fundamentals and applications for functional thin films, nano-materials and MEMS". Elsevier Inc. 2012.
- [70] K. Ogura, M. Kadowaki, J. Okawa, E. Einarsson, and S. Maruyama, "Growth mechanism of vertically aligned SWNTs by in-situ absorption measurements," *33rd Fullerene Nanotube General Symposium*, 2007.
- [71] E. Smith, G. Dent. "Modern Raman spectroscopy-a practical approach". John Wiley & Sons, Ltd. 2005.
- [72] J.R. Ferraro. "Introductory Raman spectroscopy, second edition". Elsevier, 2003.
- [73] A. Jorio, M. Dresselhaus, R. Saito, G.F. Dresselhaus. "Raman spectroscopy in graphene

related systems". Wiley-VCH, 2013.

[74] A. Jorio, A.G.Souza Filho, G. Dresselhaus, M.S. Dresselhaus, A.K. Swan, M.S. Ünlü, B.B. Goldberg, M.A. Pimenta, J.H. Hafner, C.M. Lieber, R. Saito. "G-band Raman spectra of isolated single wall carbon nanotubes: diameter and chirality dependence". *Materials Research Society Symposium Proceedings*, 2002, **707**: Z6.19.

[75] S.D.M. Brown, A. Jorio, P. Corio. "Origin of the Breit-Wigner-Fano lineshape of the tangential G-band feature of metallic carbon nanotubes". *Physical Review B*, 2001, **63**: 155414.

[76] A. Jorio, M.A. Pimenta, A.G. Souza Filho, R. Saito, G. Dresselhaus, M.S. Dresselhaus. "Characterizing carbon nanotube samples with resonance Raman scattering". *New Journal of Physics*, 2003, **5**: 139.1-139.7.

[77] H. Telg, J.G. Duque, M. Staiger, X. Tu, F. Hennrich, M.M. Kappes, M. Zheng, J. Maultzsch, C.Thomsen, S.K. Doorn. "Chiral index dependence of the G^+ and G^- Raman modes in semiconducting carbon nanotubes". *ACS Nano*, 2012, **6** (1) 904-911.

[78] A.I. López-Lorente, B.M. Simonet, M. Valcárcel. "Raman spectroscopic characterization of single walled carbon nanotubes: influence of the sample aggregation state". *Analyst*, 2014, **139**: 290-298.

[79] V.M. Irurzun, M.P. Ruiz, D.E. Resasco. "Raman intensity measurements of single-walled carbon nanotube suspensions as a quantitative technique to assess purity". *Carbon*, 2010, **48**: 2873-2881.

[80] Y. Miyata, K. Mizuno, H. Kataura. "Purity and defect characterization of single-wall carbon nanotubes using Raman spectroscopy". *Journal of Nanomaterials*, 2011, **2011**: 786763.

[81] J. Maultzsch, H. Telg, S. Reich, C. Thomsen. "Radial breathing mode of single-walled carbon nanotubes: optical transition energies and chiral-index assignment". *Physical Review B*, 2005, **72**: 205438.

[82] P.T. Araujo, I.O. Maciel, P.B.C. Pesce, M.A. Pimenta, S.K. Doorn, H. Qian, A. Hartschuh, M. Steiner, L. Grigorian, K. Hata, A. Jorio. "Nature of the constant factor in the

relation between radial breathing mode frequency and tube diameter for single-wall carbon nanotubes". *Physical Review B*, 2008, **77**: 241403.

[83] A. Jorio, R. Saito, J.H. Hafner, C.M. Lieber, M. Hunter, T. McClure, G. Dresselhaus, M.S. Dresselhaus. "Structural (n, m) determination of isolated single-wall carbon nanotubes by resonant Raman scattering". *Physical Review Letters*, 2001, **86** (6): 1118-1121.

[84] H. Kuzmany, W. Plank, M. Hulman, Ch. Kramberger, A. Grüneis, Th. Pichler, H. Peterlik, H. Kataura, Y. Achiba. "Determination of SWCNT diameters from the Raman response of the radial breathing mode". *The European Physical Journal B*, 2001, **22**: 307-320.

[85] A. Jorio, F.M. Matinaga, A. Righi, M.S.S. Dantas, M.A. Pimenta, A.G. Souza Filho, J. Mendes Filho, J.H. Hafner, C.M. Lieber, R. Saito, G. Dresselhaus, M.S. Dresselhaus. "Resonance Raman scattering: nondestructive and noninvasive technique for structural and electronic characterization of isolated single-wall carbon nanotubes". *Brazilian Journal of Physics*, 2002, **32** (4): 921-924.

[86] R. Xiang, E. Einarsson, Y. Murakami, J. Shiomi, S. Chiashi, Z. Tang, S. Maruyama. "Diameter modulation of vertically aligned single-walled carbon nanotubes". *ACS Nano*, 2012, **6** (8): 7472-7479.

[87] Y. Miyauchi, S. Chiashi, Y. Murakami, Y. Hayashida, S. Maruyama. "Fluorescence spectroscopy of single-walled carbon nanotubes synthesized from alcohol". *Chemical Physics Letters*, 2004, **387**: 198-203.

[88] T. Koyama, S. Shimizu, T. Saito, Y. Miyata, H. Shinohara, A. Nakamura. "Ultrafast luminescence kinetics of metallic single-walled carbon nanotubes: possible evidence for excitonic luminescence". *Physical Review B*, 2012, **85**: 045428.

[89] Y. Oyama, R. Saito, K. Sato, J. Jiang, Ge.G. Samsonidze, A. Grüneis, Y. Miyauchi, S. Maruyama, A. Jorio, G. Dresselhaus, M.S. Dresselhaus. "Photoluminescence intensity of single-wall carbon nanotubes". *Carbon*, 2006, **44**: 873-879.

[90] Y. Murakami, E. Einarsson, T. Edamura, S. Maruyama. "Optical absorption properties of single-walled carbon nanotubes". *Thermal Science & Engineering*, 1999, **7** (4):10-11.

- [91] S.M. Tabakman, K. Welsher, G. Hong, H. Dai. "Optical properties of single-walled carbon nanotubes separated in a density gradient: length, bundling, and aromatic stacking effects". *The Journal of Physical Chemistry C*, 2010, **114**: 19569-19575.
- [92] E. Malic, A. Knorr. "Graphene and carbon nanotubes: ultrafast relaxation dynamics and optics". Wiley-VCH Verlag GmbH & Co. KGaA. 2013.
- [93] A.J. Blanch, C.E. Lenehan, J. S. Quinton. "Optimizing surfactant concentrations for dispersion of single-walled carbon nanotubes in aqueous solution". *The Journal of Physical Chemistry B*, 2010, **114**: 9805-9811.
- [94] Y. Zhang, A. Chang, J. Cao, Q. Wang, W. Kim, Y. Li, N. Morris, E. Yenilmez, J. Kong, H. Dai. "Electric-field directed growth of aligned single-walled carbon nanotubes". *Applied Physics Letters*, 2001, **79** (9): 3155-3157.
- [95] S. Huang, X. Cai, J. Liu. "Growth of millimeter-long and horizontally aligned single-walled carbon nanotubes on flat substrates". *Journal of the American Chemical Society*, 2003, **125**: 5636-5637.
- [96] C. Kocabas, S.H. Hur, A. Gaur, M.A. Meitl, M. Shim, J.A. Rogers. "Guided growth of large-scale, horizontally aligned arrays of single-walled carbon nanotubes and their use in thin film transistors". *Small*, 2005, **1** (11): 1110-1116.
- [97] Z. Jin, H. Chu, J. Wang, J. Hong, W. Tan, Y. Li. "Ultralow feeding gas flow guiding growth of large-scale horizontally aligned single-walled carbon nanotube arrays". *Nano Letters*, 2007, **7** (7): 2073-2079.
- [98] J. Li, Y. He, Y. Han, K. Liu, J. Wang, Q. Li, S. Fan, K. Jiang. "Direct identification of metallic and semiconducting single-walled carbon nanotubes in scanning electron microscopy". *Nano Letters*, 2012, **12**: 4095-4101.
- [99] S. Iijima. "Helical microtubules of graphitic carbon". *Nature*, 1991, **354**: 56-58.
- [100] E. Einarsson, M. Kadowaki, K. Ogura, J. Okawa, R. Xiang, Z. Zhang, T. Yamamoto, Y. Ikuhara, S. Maruyama. "Growth mechanism and internal structure of vertically aligned single-walled carbon nanotubes". *Journal of Nanoscience and Nanotechnology*, 2008, **8** (11): 1-6.

- [101] P. Hillion, S. Quinnez. "Huygens-Fresnel principle in the spinor theory of light". *Journal of Optics*, 1983, **14** (3): 143-160.
- [102] X. Chen, R. Xiang, P. Zhao, H. An, T. Inoue, S. Chiashi, S. Maruyama. "Chemical vapor deposition growth of large single-crystal bernal-stacked bilayer graphene from ethanol". *Carbon*, 2016, **107**: 852-856.
- [103] H.E. du Plessis, J.P.R. de Villiers, A. Tuling, E.J. Olivier. "Stacking disorder in silicon carbide supported cobalt crystallites: an X ray- diffraction, electron diffraction and high resolution electron microscopy study". *Physical Chemistry Chemical Physics*, 2016, **18**: 30183-30188.
- [104] G. Rupprechter, K. Hayek, H. Hofmeister. "Electron microscopy of thin-film model catalysts: activation of alumina-supported rhodium nanoparticles". *Journal of Catalysis*, 1998, **173**: 409-422.
- [105] P.B. Balbuena, J. Zhao, S. Huang, Y. Wang, N. Sakulchaicharoen, D.E. Resasco. "Role of the catalyst in the growth of single-wall carbon nanotubes". *Journal of Nanoscience and Nanotechnology*, 2006, **6**:1-12.
- [106] Y. Li, R. Cui, L. Ding, Y.Liu, W. Zhou, Y. Zhang, Z. Jin, F. Peng, J. Liu. "How catalyst affect the growth of single-walled carbon nanotubes on substrates". *Advanced Materials*, 2010, **22**: 1508-1515.
- [107] D. Yuan, L. Ding, H. Chu, Y. Feng, T.P. McNicholas, J. Liu. "Horizontally aligned single-walled carbon nanotubes on quartz from a large variety of metal catalysts". *Nano Letters*, 2008, **8** (8): 2576-2579.
- [108] Y. Sun, J.A. Rogers. "Semiconductor nanomaterials for flexible technologies: from photovoltaics and electronic to sensors and energy storage (micro and nano technologies)". William Andrew; 1e dition. 2010.
- [109] S.M. Bachilo, L. Balzano, J.E. Herrera, F. Pompeo, D.E. Resasco, R.B. Weisman. "Narrow (n, m) distribution of single-walled carbon nanotubes grown using a solid supported catalyst". *Journal of the American Chemical Society*, 2003, **125**: 11186-11187.
- [110] X. Li, X. Tu, S. Zaric, K. Welsher, W.S. Seo, W. Zhao, H. Dai. "Selective synthesis

combined with chemical separation of single-walled carbon nanotubes for chirality selection". *Journal of the American Chemical Society*, 2007, **129**: 15770-15771.

[111] K. Cui, A. Kumamoto, R. Xiang, H. An, B. Wang, T. Inoue, S. Chiashi, Y. Ikuhara, S. Maruyama. "Synthesis of subnanometer-diameter vertically aligned single-walled carbon nanotubes with copper-anchored cobalt catalysts". *Nanoscale*, 2016, **8**: 1608-1617.

[112] J. Ma, J.N. Wang, X.X. Wang. "Large-diameter and water-dispersible single-walled carbon nanotubes: synthesis, characterization and applications". *Journal of Materials Chemistry*, 2009, **19**: 3033-3041.

[113] M. He, A.I. Chernov, P.V. Fedotov, E.D. Obraztsova, J. Sainio, E. Rikkinen, H. Jiang, Z. Zhu, Y. Tian, E.I. Kauppinen, M. Niemelä, A.O.I. Krause. "Predominant (6, 5) single-walled carbon nanotube growth on a copper-promoted iron catalyst". *Journal of the American Chemical Society*, 2010, **132**: 13994-13996.

[114] M. He, B. Liu, A.I. Chernov, E.D. Obraztsova, I. Kauppi, H. Jiang, I. Anoshkin, F. Cavalca, T.W. Hansen, J.B. Wagner, A.G. Nasibulin, E.I. Kauppinen, J. Linnekoski, M. Niemelä, J. Lehtonen. "Growth mechanism of single-walled carbon nanotubes on iron-copper catalyst and chirality studies by electron diffraction". *Chemistry of Materials*, 2012, **24**: 1796-1801.

[115] M. He, A.I. Chernov, E.D. Obraztsova, H. Jiang, E.I. Kauppinen, J. Lehtonen. "Synergistic effects in FeCu bimetallic catalyst for low temperature growth of single-walled carbon nanotubes". *Carbon*, 2013, **52**: 590-594.

[116] B. Corain, G. Schmid, N. Toshima, "Metal Nanoclusters in catalysis and materials science". Elsevier Science, 2007.

[117] W. Zhou, Z. Han, J. Wang, Y. Zhang, Z. Jin, X. Sun, Y. Zhang, C. Yan, Y. Li. "Copper catalyzing growth of single-walled carbon nanotubes on substrates". *Nano Letters*, 2006, **6** (12): 2987-2990.

[118] R. Cui, Y. Zhang, J. Wang, W. Zhou, Y. Li. "Comparison between copper and iron as catalyst for chemical vapor deposition of horizontally aligned ultralong single-walled carbon nanotubes on silicon substrates". *The Journal of Physical Chemistry C*, 2010, **114**:

15547-15552.

- [119] X. Zhao, Y. Liu, R. Cui, Y. Li. "Nucleation of copper nanoparticles on quartz as catalysts to grow single-walled carbon nanotubes arrays". *Carbon*, 2016, **110**: 390-395.
- [120] A.G. Nasibulin, P.V. Pikhitsa, H. Jiang, E.I. Kauppinen. "Correlation between catalyst particle and single-walled carbon nanotube diameters". *Carbon*, 2005, **43**: 2251-2257.
- [121] G. Chen, R.C. Davis, D.N. Futaba, S. Sakurai, K. Kobashi, M. Yumura, K. Hata. "A sweet spot for highly efficient growth of vertically aligned single-walled carbon nanotube forests enabling their unique structures and properties". *Nanoscale*, 2016, **8**: 162-171.
- [122] Y. Fukamori, M. König, B. Yoon, B. Wang, F. Esch, U. Heiz, U. Langman. "Fundamental insight into the substrate-dependent ripening of monodisperse clusters". *ChemCatChem ChemPubSoc Europe*, 2013, **5**: 3330-3341.
- [123] M. Hu, Y. Murakami, M. Ogura, S. Maruyama, T. Okubo. "Morphology and chemical state of Co-Mo catalysts for growth of single-walled carbon nanotubes vertically aligned on quartz substrates". *Journal of Catalysis*, 2004, **225**: 230-239.
- [124] M.S. Dresselhaus, G. Dresselhaus, P. Avouris. "Carbon nanotubes-synthesis, structure, properties, and applications". Springer Science & Business Media, 2001.
- [125] R. Krupke, F. Hennrich, H.v. Löhneysen, M.M. Kappes: "Separation of metallic from semiconducting single-walled carbon nanotubes". *Science*, 2003, **301**: 344-347.
- [126] M.S. Arnold, S.I. Stupp, M.C. Hersam. "Enrichment of single-walled carbon nanotubes by diameter in density gradients". *Nano Letters*, 2005, **5** (4): 713-718.
- [127] M.L. Usrey, E.S. Lippmann, M.S. Strano. "Evidence for a two-step mechanism in electronically selective single-walled carbon nanotube reactions". *Journal of the American Chemical Society*, 2005, **127**: 16129-16135.
- [128] S. Banerjee, T. Hemraj-Benny, S.S. Wong. "Covalent surface chemistry of single-walled carbon nanotubes". *Advanced Materials*, 2005, **17** (1): 17-29.
- [129] M. Zheng, A. Jagota, M.S. Strano, A.P. Santos, P. Barone, S.G. Chou, B.A. Diner, M.S. Dresselhaus, R.S. Mclean, G.B. Onoa, G.G. Samsonidze, E.D. Semke, M. Usrey, D.J. Walls. "Structure-based carbon nanotube sorting by sequence-dependent DNA assembly". *Science*,

2003, **302**: 1545-1548.

[130] P. Zhao, E. Einarsson, R. Xiang, Y. Murakami, S. Maruyama. "Controllable expansion of single-walled carbon nanotub dispersions using density gradient ultracentrifugation". *Journal of Physical Chemistry C*, 2010, **114**: 4831-4834.

[131] I. Yahya, F. Bonaccorso, S.K. Clowes, A.C. Ferrari. "Temperature dependent separation of metallic and semiconducting carbon nanotubes using gel agarose chromatography". *Carbon*, 2015, **93**: 574-594.

[132] X. He, W. Gao, L. Xie, B. Li, Q. Zhang, S. Lei, J.M. Robinson, E.H. H  roz, S.K. Doorn, W. Wang, R. Vajtai, P.M. Ajayan, W.W. Adams, R.H. Hauge, J. Kono. "Wafer-scale monodomain films of spontaneously aligned single-walled carbon nanotubes". *Nature Nanotechnology*, 2016, **11**: 633-638.

[133] P. Diao, Z. Liu. "Vertically aligned single-walled carbon nanotubes by chemical assembly-methodology, properties, and applications". *Advanced Materials*, 2010, **22**:1430-1449.

[134] G. Lolli, L. Zhang, L. Balzano, N. Sakulchaicharoen, Y. Tan, D.E. Resasco. "Tailoring (n, m) structure of single-walled carbon nanotubes by modifying reaction conditions and the nature of the support of CoMo catalysts". *The Journal of Physical Chemistry B*, 2006, **110**: 2108-2115.

[135] T. Thurakitseree, C. Kramberger, A. Kumamoto, S. Chiashi, E. Einarsson, S. Maruyama. "Reversible diameter modulation of single-walled carbon nanotubes by acetonitrile-containing feedstock". *ACS Nano*, 2013, **7(3)**: 2205-2211.

[136] Y. Homma. "Gold nanoparticles as the catalyst of single-walled carbon nanotube synthesis". *Catalysts*, 2014, **4**: 38-48.

[137] W. Chiang, R.M. Sankaran. "The influence of bimetallic catalyst composition on single-walled carbon nanotube yield". *Carbon*, 2012, **50**: 1044-1050.

[138] G. Chen, Y. Seki, H. Kimura, S. Sakurai, M. Yumura, K. Hata, D.N. Futaba. "Diameter control of single-walled carbon nanotube forests from 1.3-3.0 nm by arc plasma deposition". *Scientific Reports*, 2014, **4**:3804.

- [139] L. Durrer, J. Greenwald, T. Helbling, M. Muoth, R. Riek, C. Hierold. “Narrowing SWNT diameter distribution using size-separated ferritin-based Fe catalysts”. *Nanotechnology*, 2009, **20**:355601.
- [140] T. Ohashi, T. Shima. “Synthesis of vertically aligned single-walled carbon nanotubes with metallic chirality through facet control of catalysts”. *Carbon*, 2015, **87**:453-461.
- [141] Y. Hu, L. Kang, Q. Zhao, H. Zhong, S. Zhang, L. Yang, Z. Wang, J. Lin, Q. Li, Z. Zhang, L. Peng, Z. Liu, J. Zhang. “Growth of high-density horizontally aligned SWNT arrays using Trojan catalysts”. *Nature Communications*, 2015, **6**: 6099.
- [142] Y. Miyauchi, S. Chiashi, Y. Murakami, Y. Hayashida, S. Maruyama. “Fluorescence spectroscopy of single-walled carbon nanotubes synthesized from alcohol”. *Chemical Physics Letters*, 2004, **387**:198-203.
- [143] L. Ding, A. Tselev, J. Wang, D. Yuan, H. Chu, T.P. McNichlas, Y. Li, J. Liu. “Selective growth of well-aligned semiconducting single-walled carbon nanotubes”. *Nano Letters*, 2009, **9**(2):800-805.
- [144] W. Zhou, S. Zhan, L. Ding, J. Liu. “General rules for selective growth of enriched semiconducting single-walled carbon nanotubes with water vapor as in situ etchant”. *Journal of the American Chemical Society*, 2012, **134**(34): 14019-14026.
- [145] J. Li, C. Ke, K. Liu, P. Li, S. Liang, G. Finkelstein, F. Wang, J. Liu. “Importance of diameter control on selective synthesis of semiconducting single-walled carbon nanotubes”. *ACS Nano*, 2014, **8**(8): 8564–8572.
- [146] G. Hong, B. Zhang, B. Peng, J. Zhang, W. M. Choi, J. Y. Choi, J. M. Kim, Z. Liu. “Direct growth of semiconducting single-walled carbon nanotube array”. *Journal of American Chemical Society*, 2009, **131**(41): 14642–14643.
- [147] A. R. Harutyunyan, G. Chen, T. M. Paronyan, E. M. Pigos, O. A. Kuznetsov, K. Hewaparakrama, S. M. Kim, D. Zakharov, E. A. Stach, G. U. Sumanasekera. “Preferential growth of single-walled carbon nanotubes with metallic conductivity”. *Science*, 2009, **326**: 116–120.
- [148] H. Wang, B. Wang, X. Y. Quek, L. Wei, J. Zhao, L. Li, M. B. Chan-Park, Y. Yang, Y.

- Chen. “Selective synthesis of (9, 8) single walled carbon nanotubes on cobalt incorporated TUD-1 catalysts”. *Journal of American Chemical Society*, 2010, **132**(47): 16747–16749.
- [149] H. Wang, L. Wei, F. Ren, Q. Wang, L. D. Pfefferle, G. L. Haller and Y. Chen. “Chiral-selective $\text{CoSO}_4/\text{SiO}_2$ catalysts for (9, 8) single-walled carbon nanotube growth”. *ACS Nano*, 2013, **7**(1): 614–626.
- [150] L. Wei, B. Liu, X. Wang, H. Gui, Y. Yuan, S. Zhai, A. K. Ng, C. Zhou. Y. Chen. “(9, 8) Single-walled carbon nanotube enrichment via aqueous two-phase separation and their thin-film transistor applications”. *Advanced Electronic Materials*, 2015, **1**: 1500151.
- [151] F. Ding, A. R. Harutyunyan, B. I. Yakobson. “Dislocation theory of chirality-controlled nanotube growth”. *Proceedings of the National Academy of Sciences*, 2009, **106**: 2506–2509.
- [152] R. Rao, D. Liptak, T. Cherukuri, B. I. Yakobson, B. Maruyama. “In situ evidence for chirality-dependent growth rates of individual carbon nanotubes”. *Nature Materials*, 2012, **11**: 213–216.
- [153] V. I. Artyukhov, E. S. Penev, B. I. Yakobson. “Why nanotubes grow chiral”. *Nature Communications*, 2014, **5**: 4892.
- [154] L. Zhang, P. Hou, S. Li, C. Shi, H. Cong, C. Liu, H. Cheng. “In situ TEM observations on the sulfur-assisted catalytic growth of single-walled carbon nanotubes”. *The Journal of Physical Chemistry Letters*, 2014, **5**(8): 1427-1432.
- [155] J.A. Rodríguez-Manzo, I. Janowska, C. Pham-Huu, A. Tolvanen, A.V. Krashenninnikov, K. Nordlund, F. Banhart. “Growth of single-walled carbon nanotubes from sharp metal tips”. *Small*, 2009, **5**(23): 2710-2715.
- [156] M. He, H. Jiang, B. Liu, P.V. Fedotov, A.I. Chernov, E.D. Obraztsova, F. Cavalca, J.B. Wagner, T.W. Hansen, I.V. Anoshkin, E.A. Obraztsova, A.V. Belkin, E. Sairanen, A.G. Nasibulin, J. Lehtonen, E.I. Kauppinen. “Chiral-selective growth of single-walled carbon nanotubes on lattice-mismatched epitaxial cobalt nanoparticles”. *Scientific Reports*, 2013, **3**: 1460.
- [157] M. He, H. Amara, H. Jiang, J. Hassinen, C. Bichara, R.H.A. Ras, J. Lehtonen, E.I.

- Kauppinen, A. Loiseau. "Key roles of carbon solubility in single-walled carbon nanotube nucleation and growth". *Nanoscale*, 2015, **7**:20284-20289.
- [158] M. Fouquet, B.C. Bayer, S. Esconjauregui, R. Blume, J.H. Warner, S. Hofmann, R. Schlögl, C. Thomsen, J. Robertson. "Highly chiral-selective growth of single-walled carbon nanotubes with a simple monometallic Co catalyst". *Physical Review B*, 2012, **85**:235411.
- [159] P. Li, X. Zhang, J. Liu. "Aligned single-walled carbon nanotube arrays from rhodium catalysts with unexpected diameter uniformity independent of the catalyst size and growth temperature". *Chemistry of Materials*, 2016, **28**: 870-875.
- [160] L. Kang, S. Deng, S. Zhang, Q. Li, J. Zhang. "Selective growth of subnanometer diameter single-walled carbon nanotube arrays in hydrogen-free CVD". *Journal of the American Chemical Society*, 2016, **138**: 12723-12726.
- [161] X. Li, X. Tu, S. Zaric, K. Welsher, W.S. Seo, W. Zhao, H. Dai. "Selective synthesis combined with chemical separation of single-walled carbon nanotubes for chirality selection". *Journal of the American Chemical Society*, 2007, **129**: 15770-15771.
- [162] X. Wang, W. Yue, M. He, M. Liu, J. Zhang, Z. Liu. "Bimetallic catalysts for the efficient growth of SWNTs on surface". *Chemistry of Materials*, 2004, **16**(5):799-805.
- [163] B. Liu, W. Ren, S. Li, C. Liu, H. Cheng. "High temperature selective growth of single-walled carbon nanotubes with a narrow chirality distribution from a CoPt bimetallic catalysts". *Chemical Communications*, 2012, **48**(18): 2409-2411.
- [164] F. Yang, X. Wang, D. Zhang, J. Yang, D. Luo, Z. Xu, J. Wei, J. Wang, Z. Xu, F. Peng, X. Li, R. Li, Y. Li, M. Li, X. Bai, F. Ding, Y. Li. "Chirality-specific growth of single-walled carbon nanotubes on solid alloy catalysts". *Nature*, 2014, **510**: 522-524.
- [165] F. Yang, X. Wang, D. Zhang, K. Qi, J. Yang, Z. Xu, M. Li, X. Zhao, X. Bai, Y. Li. "Growing zigzag (16, 0) carbon nanotubes with structure defined catalysts". *Journal of the American Chemical Society*, 2015, **137** (27): 8688-8691.
- [166] F. Yang, X. Wang, J. Si, X. Zhao, K. Qi, C. Jin, Z. Zhang, M. Li, D. Zhang, J. Yang, Z. Zhang, Z. Xu, L. Peng, X. Bai, Y. Li. "Water-assisted preparation of high-purity semiconducting (14, 4) carbon nanotubes". *ACS Nano*, 2016, Doi:10.1021/acsnano.6b06890.

- [167] T. Yamada, T. Namai, K. Hata, D.N. Futaba, K. Mizuno, J. Fan, M. Yudasaka, M. Yumura, S. Iijima. "Size-selective growth of double-walled carbon nanotube forests from engineered iron catalysts". *Nature Nanotechnology*, 2006, **1**: 131-136.
- [168] D. Zhang, J. Yang, F. Yang, R. Li, M. Li, D. Ji, Y. Li. "(n, m) assignments and quantification for single-walled carbon nanotubes on SiO₂/Si substrates by resonant Raman spectroscopy". *Nanoscale*, 2015, **7**:10719-10727.
- [169] E.H. H  roz, J.G. Duque, W.D. Rice, C.G. Densmore, J. Kono, S.K. Doorn. "Resonant Raman spectroscopy of armchair carbon nanotubes: absence of broad G⁻ feature". *Physical Review B*, 2011, **84**: 121403.
- [170] H. An, A. Kumamoto, H. Takezaki, S. Ohyama, Y. Qian, T. Inoue, Y. Ikuhara, S. Chiashi, R. Xiang, S. Maruyama. "Chirality specific and spatially uniform synthesis of single-walled carbon nanotubes from a sputtered Co-W bimetallic catalyst". *Nanoscale*, 2016, **8**: 14523-14529.
- [171] X. Tu, A.R.H. Walker, C.Y. Khripin, M. Zheng. "Evolution of DNA sequences toward recognition of metallic armchair carbon nanotubes". *Journal of the American Chemical Society*, 2011, **133**: 12998-13001.
- [172] E.H. H  roz, J.G. Duque, X. Tu, M. Zheng, A.R.H. Walker, R.H. Hauge, S.K. Doorn, J. Kono. "Fundamental optical process in armchair carbon nanotubes". *Nanoscale*, 2013, **5**: 1411-1439.
- [173] M. Kumar, Y. Ando. "Chemical vapor deposition of carbon nanotubes: a review on growth mechanism and mass production". *Journal of Nanoscience and Nanotechnology*, 2010, **10**: 3739-3758.
- [174] B.C. Bayer, C. Baehtz, P.R. Kidambi, R.S. Weatherup, C. Mangler, J. Kotakoski, C.J.L. Goddard, S. Caneva, A.C. Vilatela, J.C. Meyer, S. Hofmann. "Nitrogen controlled iron catalyst phase during carbon nanotube growth". *Applied Physics Letters*, 2014, **105**: 143111.
- [175] B. Zhou, S. Han, R. Raja and G. A. Somorjai, *Nanotechnology in catalysis 3*, Springer Science & Business Media, 2007.
- [176] J.E. Herrera, D.E. Resasco. "Role of Co-W interaction in the selective growth of

single-walled carbon nanotubes from CO disproportionation”. *The Journal of Physical Chemistry B*, 2003, **107**: 3738-3746.

[177] P. Villars, Inorganic Solid Phases, SpringerMaterials (online database), Springer, Heidelberg (ed.), Springer Materials: $\text{Co}_6\text{W}_6\text{C}$ ($\text{W}_6\text{Co}_6\text{C}$) Crystal Structure.

[178] E. Einarsson, Y. Murakami, M. Kadowaki, S. Maruyama. “Growth dynamics of vertically aligned single-walled carbon nanotubes from *in situ* measurements”. *Carbon*, 2008, **46**: 923-930.

[179] G. Chen, R.C. Davis, H. Kimura, S. Sakurai, M. Yumura, D.N. Futaba, K. Hata. “The relationship between the growth rate and the lifetime in carbon nanotube synthesis”. *Nanoscale*, 2015, **7**: 8873-8878.

[180] M. Bedewy, B. Viswanath, E.R. Meshot, D.N. Zakharov, E.A. Stach. “Measurement of the dewetting, nucleation, and deactivation kinetics of carbon nanotube population growth by environmental transmission electron microscopy”. *Chemistry of Materials*, 2016, **28**: 3804-3813.

[181] A. Li-Pook-Than, J. Lefebvre, P. Finnie. “Phases of carbon nanotube growth and population evolution from *in situ* Raman spectroscopy during chemical vapor deposition”. *The Journal of Physical Chemistry C*, 2010, **114**: 11018-11025.

[182] A.S. Shirinyan, A.M. Gusak, M. Wautelet. “Phase diagram versus diagram of solubility: What is the difference for nanosystem?” *Acta Materialia*, 2005, **53**: 5025-5032.

[183] A. Markström, B. Sundman, K. Frisk. “A revised thermodynamic description of the Co-W-C system”. *Journal of Phase Equilibria and Diffusion*, 2005, **26** (2): 152-160.

List of abbreviations

2D: Two dimensional

3D: Three dimensional

CNT(s): Carbon nanotube(s)

SWNT(s): Single-walled carbon nanotube(s)

MWNT(s): Multi-walled carbon nanotube(s)

VLS: Vapor-liquid-solid mechanism

vHS: van Hove singularities

DOS: Density of states

VA-SWNT(s): Vertically-aligned SWNT(s)

CVD: Chemical vapor deposition

ACCVD: Alcohol catalytic chemical vapor deposition

sccm: Standard cubic centimeters per minute

RBM: Radial Breathing Mode

BWF: Breit–Wigner–Fano feature

SDS: Sodium dodecyl sulfate

D₂O: Deuterium oxide

SAED: Selected area electron diffraction

PL: Photoluminescence excitation spectroscopy

SEM: Scanning electron microscopy

TEM: Transmission electron microscopy

STEM: Scanning transmission electron microscopy

EDS-STEM: Energy dispersive X-ray spectroscopy-scanning transmission electron microscopy

HAADF-STEM: High angle annular dark field-scanning transmission electron microscopy

EDS: Energy dispersive X-ray spectroscopy

FFT: Fast Fourier transform

FCC: Face-centered cubic

BCC: Body-centered cubic

List of publications

- [1] **H. An**, A. Kumamoto, H. Takezaki, S. Ohyama, Y. Qian, T. Inoue, Y. Ikuhara, S. Chiashi, R. Xiang, S. Maruyama, “Chirality specific and spatially uniform synthesis of single-walled carbon nanotubes from a sputtered Co-W bimetallic catalyst”. *Nanoscale*, 2016, **8**, 14523-14529.
- [2] K. Cui, A. Kumamoto, R. Xiang, **H. An**, B. Wang, T. Inoue, S. Chiashi, Y. Ikuhara, S. Maruyama, “Synthesis of subnanometer-diameter vertically aligned single-walled carbon nanotubes with copper-anchored cobalt catalysts.” *Nanoscale*, 2016, **8**, 1608-1617.
- [3] X. Chen, R. Xiang, P. Zhao, **H. An**, T. Inoue, S. Chiashi, S. Maruyama. “Chemical vapor deposition growth of large single-crystal bernal-stacked bilayer graphene from ethanol”. *Carbon*, 2016, **107**, 852-856.

Acknowledgement

The time of working on this dissertation reminds me all the impressions during the past three years and a half. Foremost, I am really grateful to the China Scholarship Council for the financial support of my PhD course. Focusing on a classic topic not only offers me the chance to go through all the excellent pioneering works but also inspires new ideas by standing on the shoulders of giants. Working in the group of Maruyama Laboratory is very impressive and interesting. The colorful world in nanosize and hardworking people in Japan teach me how to do research. I am sincerely grateful to my supervisor Professor Shigeo Maruyama for his kind and patient supports. His sense of research, enthusiasm for knowledge and insight to scientific development together with his hardworking encourage me a lot.

I also would like to thank Professor Shohei Chiashi for his help and advising on my work. His solid knowledge on the spectroscopic measurement provides me a guarantee on the interpretation of experimental results. I am thankful to Professor Rong Xiang for his support and discussion on my TEM study. We did spend almost half a year on selecting the appropriate microgrid for in-plane TEM with Dr. Kehang Cui. Fortunately, we find the right ones. I also want to thank Professor Inoue for his support on my experiments and research discussions. I would like to thank Mr. Watanabe, Dr. Kehang Cui, Dr. Xiao Chen, Dr. JinHyeok Cha, Dr. Heeyuen Koh, Dr Sungjin Kim, Takaaki Chiba, Keigo Otsuka, Takafumi Oyake, Cheng Wu for their help in my struggling time of the first year in Japan. I would like to thank Ms. Terao, Ms. Shimada, Ya Feng, Qing Wang, Bo Hou, Yang Qian, and all other members in the lab for their help.

I am also thankful to our collaborators, Professor Yuichi Ikuhara, Dr. Akihito Kumamoto for their support on TEM. Their solid expertise, extensive experience and interpretation on TEM inspire me a lot on my own research. Many thanks should also go to Mr. T. Itoh, Mr. H. Tsunakawa for their assistance and discussions on TEM.

The last but not the least, I need to thank my families for their love and understanding.